Highly-Efficient Thermoelectronic Conversion of Heat and Solar Radiation to Electric Power

Dissertation zur Erlangung des Doktorgrades
der Mathematisch-Naturwissenschaftlichen Fakultät
der Universität Augsburg

Vorgelegt von Stefan Meir

Augsburg, November 2012

Tag der mündlichen Prüfung	17. Dezember 2012
Erstgutachter	Prof. Dr. J. Mannhart (Max-Planck Institut für Festkörperforschung, Stuttgart)
Zweitgutachter	Prof. Dr. A. Reller (Universität Augsburg)

Contents

1 Introduction

As William Shockley and Hans-Joachim Queisser have shown [1], the efficiency of single-junction photovoltaic (PV) cells is limited to around 34 %. Various concepts have been suggested to overcome this limit [2–4], the most promising of which is to use multiple junctions and to illuminate the cell with concentrated sunlight. To date, the best laboratory-scale PV cells making use of this principle reach an efficiency of 43.5 % [5]. However, PV cells available on the mass market have far smaller efficiencies ranging from 10 % to 20 % [6].

Most of the incident energy not converted to electric power heats up the solar panel. In principle, it should be possible to recycle this heat by feeding it into a secondary heat engine. However, the efficiency of PV cells usually decreases significantly with increasing cell temperature. On the other hand, the efficiency of any secondary heat engine is ultimately limited to the Carnot efficiency

$$\eta_\mathrm{C} = 1 - \frac{T_\mathrm{h}}{T_\mathrm{l}},$$

where $T_\mathrm{h} \approx 350\,\mathrm{K}$ and $T_\mathrm{l} \approx 300\,\mathrm{K}$ are typical values for the temperatures of the high and low temperature reservoirs, selected such that the PV cell can still work efficiently. Hence, even a perfect secondary heat engine will convert the waste heat to electricity with an efficiency of less than 14 %, which hardly justifies the effort to include it into the system.

Despite these efficiency limitations, PV cells constitute the vast majority of the worldwide solar-to-electricity conversion capacity with 70 GW capacity being installed by the end of 2011 [6][1].

Alternatively, solar radiation can be converted to electricity by converting it to heat and running a turbine with steam generated therefrom. This technique is called Concentrated Solar Power (CSP), as sunlight has to be focused to achieve desirably high temperatures. A typical steam turbine thereby converts heat to mechanical energy with an efficiency of

[1] To give a comparison, the total electricity generation capacity installed on earth was around 4000 GW in 2009 [7].

around 40 % at a steam temperature of around 400 °C [8]. The overall efficiency is further reduced as some energy is lost in the concentrator and in the generator converting mechanical energy into electricity. However, total solar-to-electricity efficiencies of around 20 % are realized today [8, 9]. Additionally, it is possible to store thermal energy in heat tanks and to generate electricity therefrom even in times of no sunshine.

Despite those attractive characteristics, in 2011 the global capacity of CSP was only around 2 GW [6], most of which is installed in Spain and the USA.

As an alternative to mechanical steam turbines, where heat is intermediately converted to mechanical energy, it can be directly converted to electricity. As in such systems no moving parts are involved, they have the benefit of a possibly simple design, low maintenance costs, and high reliability.

Thermoelectricity (TE) is the most prominent technique of direct heat-to-electricity conversion. It makes use of the Seebeck effect: the voltage drop arising from a temperature gradient across a thermoelectric material. The efficiency of this conversion is mainly characterized by a dimensionless figure of merit, the ZT factor [10]:

$$ZT = \alpha^2 \frac{\sigma_\mathrm{e}}{\sigma_\mathrm{th}} T,$$

with the ratio of electrical to thermal conductivity $\sigma_\mathrm{e}/\sigma_\mathrm{th}$, temperature T and the Seebeck coefficient α, which is defined as the voltage created per temperature difference. With ZT approaching infinity the efficiency approaches the Carnot limit [11]. Unfortunately, materials with high $\sigma_\mathrm{e}/\sigma_\mathrm{th}$ ratios – typically metals – tend to have low Seebeck coefficients [11], while materials with high Seebeck coefficients – typically insulators – have low electrical conductivity. The best trade-off and hence the best efficiency is obtained for doped semiconductors [12]. Those materials, however, have worse Seebeck coefficients than insulators and worse $\sigma_\mathrm{e}/\sigma_\mathrm{th}$ ratios than metals, the latter being mainly due to the lattice thermal conductivity. This results in ZT being typically limited to values below 2 [11, 13].

Hence, even the best thermoelectric semiconductors commercially available today are limited to efficiencies below 10 % [14], and it has been doubted whether efficiencies above 30 % can ever be achieved [13]. Therefore, the usage of TE has been limited to applications where its solid-state nature is beneficial enough to compensate the low efficiency [15], such as powering spacecraft, small-scale cooling, and small-scale electricity generation. Thermoelectrics – as compared to the more efficient, mechanical heat engines – do not appear to be able to make a significant contribution in future large-scale electricity generation.

A less-known, but rather similar approach of direct heat-to-electricity conversion is the principle of the thermionic converter (TIC). Here, electrons are evaporated from the hot emitter electrode, transferred through a vacuum gap, and absorbed on the cold collector electrode, which thereby gets charged negatively. The resulting voltage between emitter and collector can be used to drive a current through an external load cycle, which corresponds to the generation of electric power.

The Seebeck coefficient of a TIC is comparable to an insulating thermoelectric while the ratio of electrical and thermal conductivity is even better than for metals, which is due to the absence of lattice heat conduction. This leads to a possible ZT factor as high as 40 [16]. Additionally, as emitter and collector are separated by vacuum, very high temperature differences can be utilized, leading to a high Carnot limit of the system. As will be shown in Ch. 3.2, TICs can therefore be highly efficient.

Additionally, TICs are suitable to be used as topping cycles for conventional heat engines, *e.g.*, in CSP power plants. In this configuration the waste heat transferred to the collector is used as heat input for a secondary heat engine. This way most of the waste heat of the TIC can be recycled. The efficiency of the resulting combined cycle will be discussed in Ch. 3.2, too. It will be shown that it is significantly larger than for any of the two system alone.

Due to the high efficiency of combined cycle systems, they might be an option for fossil-fuel power plants as well. Here, fossil fuels such as gas, oil, coal, or nuclear fission material are burned to produce heat. Steam or pressurized gas are generated from this heat and used in turbines to generate electricity. All of the above-mentioned fossil fuels can generate significantly higher temperatures than the best steam turbines can handle. Consequently, not the full temperature range can be employed, leading to smaller than possible Carnot efficiency limits. In gas- and oil-fired power plants, gas turbines can be used as topping cycles to increase the total conversion efficiency. However, this is not the case in coal-fired power plants [17], which account for 40 % of the global electricity generation capacity [18]. As TICs can deal with those high temperatures, they might here as well be used as topping cycles, thereby enhancing the total conversion efficiency and consequently leading to a significant reduction of CO_2 emissions and fossil fuel consumption.

Unfortunately, the conversion of heat to electricity in a TIC is usually limited by the mutual repulsion of electrons in the vacuum gap. Electrons on their way to the collector push back subsequent electrons, which therefore do not reach the collector. This space-charge cloud highly limits the current transferred to the collector and thus the efficiency.

Two methods to suppress the formation of the space charge have been developed in the past. Unfortunately, as will be shown in Ch. 2, both methods have major drawbacks, preventing the widespread use of the technique.

In this thesis a third approach to overcome the space charge was studied in a conjoint effort with C. Stephanos [19]: *thermoelectronic energy conversion* (TEC). TECs are a special type of TICs and based on the suppression of the space charge by a combination of electric and magnetic fields. While the focus of C. Stephanos' thesis is on assessing thermoelectronic converters by modeling, the focus of this work is the experimental realization and an assessment of attainable output powers and efficiencies.

2 The concept of thermionic energy conversion

In this chapter I will give a brief introduction into the principle of thermionic energy conversion, describe methods to suppress the space charge, and provide a brief review of the history of the field. The theoretical background necessary to analyze the experimental results will be provided in the next chapter.

2.1 Introduction to thermionic energy conversion

A thermionic converter is a heat engine that uses electrons as its working fluid and directly converts heat into electric energy. As sketched in Fig. 2.1, this is accomplished by evaporating electrons from the emitter and absorbing them at the collector. As electrons are removed from the emitter and transferred to the collector, the latter gets charged negatively with respect to the former. Consequently, a voltage is built up, which can be used to source a current I_l through an external load cycle R_l and back to the emitter. This voltage is therefore referred to as the load voltage V_l. In the steady state the current I_l through the load must equal the rate of electrons that are transferred across the vacuum gap.

In sum, the electric power $P_\mathrm{l} = V_\mathrm{l} I_\mathrm{l}$ is generated while the thermal power P_in is delivered to the emitter from an external heat source. At the same time, the thermal power P_rej is rejected from the collector to a cold heat reservoir. This basic working principle will be discussed in more detail in Ch. 3.

The thermal energy needed to heat the emitter can be provided from virtually any strong source of heat – in particular from sunlight, which enables the use of TICs for solar energy harvesting. Further heat sources are the burning of fossil fuels, the nuclear decay in radioisotope batteries and fission reactors, or the heat generated in future nuclear fusion reactors. TICs coupled with electric motors might even replace internal combustion engines in the automotive sector.

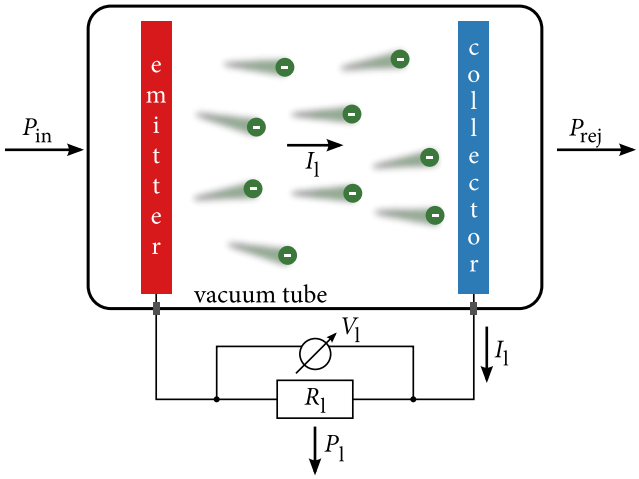

Figure 2.1: Sketch of the working principle of a thermionic converter. Electrons are evaporated from the hot emitter, cross the vacuum gap, and condense on the cold collector. There a negative charge accumulates, which can be used to drive a current I_l through an external load cycle R_l. Therefore, the system converts a fraction of the incoming thermal power P_{in} into an electric power P_l, the rest (P_{rej}) is rejected. Throughout this work the direction of the current is defined by the direction of the electron flow.

The space-charge problem

Unlike other heat engines, TICs use electrons as working fluid, which by their very nature are charged negatively and repel each other. This leads to the unfavorable effect that electrons moving from the emitter to the collector are pushed back by the space-charge cloud formed by preceding electrons. Unfortunately, this effect highly limits the current transferred to the collector to impractically small values. Hence, to build an efficient TIC the space charge has to be overcome in some way.

Historically, the most prominent approach to solve this task is adding cesium gas to the interelectrode space. The ionization energy of cesium is as low as 3.9 eV and thus the lowest of all stable elements [20, p. 10/176]. Therefore, Cs^+ ions are easily generated, *e.g.*, by electron-atom collisions, and distributed in the interelectrode space in a way that reduces the negative space-charge cloud [21]. Unfortunately, besides cesium being highly reactive and thereby limiting material choices [22, p. 603], this approach has the drawback that the ionization of the gas is an energy consuming process. Therefore, typically around 50 % of the electric output power is lost [16, 23]. Possibly more efficient ways to generate the ions have been proposed [16], but not yet demonstrated.

A second approach is to make the gap between emitter and collector too small for the space charge to build up. Electrons are then transferred across the gap fast enough to

not considerably interact with each other. This so-called close-space condition is typically met when the distance is smaller than approximately 3 µm [23, 24]. Most modern research on TIC is focused on this principle, but it has not been applied on a large scale yet [16]. It turns out to be a challenging engineering task to maintain the large temperature difference necessary for highly effective energy conversion over such a small vacuum gap. Additionally, at very small gap widths heat loss by thermal radiation is significantly increased due to near-field heat transfer [24]. The need to avoid these additional heat losses usually excludes the complete elimination of the space charge.

Overcoming the space charge with electric and magnetic fields

In this thesis, a third mechanism to overcome the space-charge effect has been studied. Our approach is to add a third, grid-like electrode consisting of meshes and grid wires in between emitter and collector. As sketched in Fig 2.2, a positive voltage applied to this electrode, the so-called gate, will accelerate electrons away from the emitter and thereby remove them from the space charge. Consequently, the space charge shrinks or even vanishes.

As no ions are involved in the process, this special type of the thermionic energy converter (TIC) is called *thermoelectronic energy converter* (TEC). It should be noted that throughout this work the term TIC is used whenever referring to the thermionic principle in general. Unless stated otherwise, general remarks with respect to TICs are equally valid for TECs.

To prevent electrons from hitting the positively charged gate, a longitudinal magnetic field is applied, which will cause electrons to move on helical paths along the magnetic field lines. Neglecting the influence of the electric field, the radius of gyration r_g of electrons in a homogeneous magnetic field is [19, 25]

$$r_g = \frac{v_\perp m_e}{eB}. \tag{2.1}$$

Here, $v_\perp$ is the velocity component perpendicular to the magnetic field, m_e the electron's mass, e the positive elementary charge, and B the magnetic flux density. Taking Boltzmann's constant k_B, $T = 1500\,°C$, $B = 0.1\,T$, and assuming $v_\perp = \sqrt{k_B T/m_e}$, this yields $r_g \approx 10\,\mu m$.

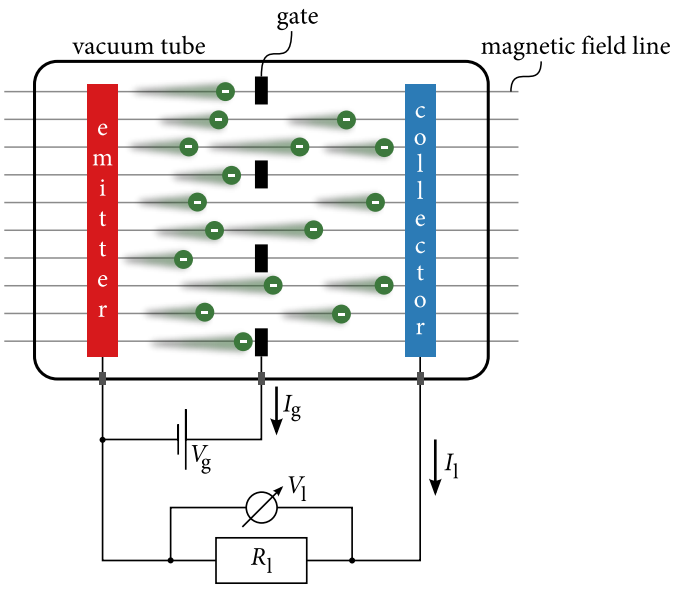

Figure 2.2: Sketch of the working principle of a thermoelectronic energy converter. By applying a positive voltage V_g to the gate, electrons are accelerated away from the emitter. At the same time the magnetic field forces the electrons to follow its field lines on helical paths (not shown) with radii of gyration much smaller than the meshes. Therefore, all those electrons following a magnetic field line that itself does not touch a gate wire also won't impinge onto the gate. These electrons will condense on the collector instead.

If, additionally, the effect of the electric field is considered, Eq. 2.1 has to be slightly modified, yielding [19, 25]

$$r_g = \frac{\sqrt{v_x^2 + (v_y + E_\perp/B)^2}\, m_e}{eB},$$

where $E_\perp$ is the component of the electric field perpendicular to the magnetic field and v_y is the velocity component in direction of $E_\perp$. In this discussion the direction of the magnetic field is identified with the z-direction.

As can be seen, the component $E_\parallel$ of the electric field pointing in direction of the magnetic field has no influence on the radius of gyration. For $E_\perp/B \ll v_x + v_y$ the radii of gyration are hardly affected by the electric field. Hence, with a sufficiently large magnetic field applied, the radii of gyration of the electron paths are significantly smaller than the meshes of any macroscopically large gate. Consequently, all those electrons following a magnetic field line that itself passes through a mesh, will also fly through that mesh and finally reach the collector.

An extensive discussion of the movement of electrons in combined electric and magnetic fields is given by C. Stephanos [19].

In summary, as the effect of the space charge is suppressed by the electric field, it no longer limits the current transmitted to the collector. At the same time, the majority of the electrons is not lost on the gate, but reaches the collector and contributes to the generation of the output power.

Earlier attempts to overcome the space charge with electric and magnetic fields

In the past, two comparable setups were studied: the magnetic and the electric triodes shown in Fig. 2.3 [21]. Both triodes and our approach share the idea to overcome the space charge by a positively charged gate. However, they do not make use of the combination of magnetic and electric fields studied within this work.

The electric triode (Fig. 2.3a) lacks a mechanism to prevent electrons from hitting the grid wires, which leads to unfavorably high gate currents. Consequently, a high electric power must be spent to sustain the gate electric field, which much reduces the conversion efficiency.

The magnetic triode (Fig. 2.3b) is ineffective in suppressing the effect of the space charge, which is due to the high effective gap width. In anticipation of the results of

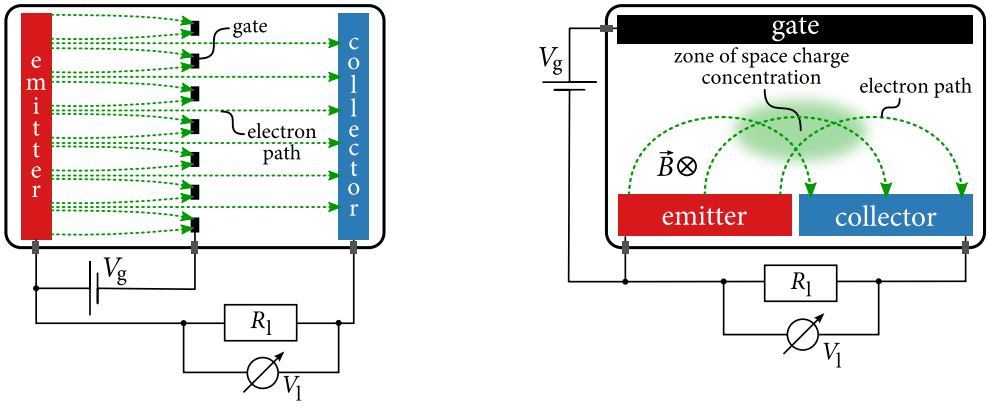

(a) Electric triode **(b)** Magnetic triode

Figure 2.3: Sketches of earlier attempts to overcome the space charge with applied E- and B-fields. **(a)** The electric triode lacks a mechanism to keep electrons from hitting the gate. Therefore, the gate current is unfavorably high [21]. **(b)** The magnetic triode [21] needs a minimum electron path length, which is defined by the dimensions of emitter and collector. As will become clear within the course of this work, short electron path lengths ($\lesssim 100\,\mu m$) are crucial for suppressing the effect of the space charge. A second drawback is that all electrons pass through the central region, which is indicated by the blurred ellipse. Therefore, the magnetic triode creates a new space-charge zone upon suppressing the original one.

this and C. Stephanos' [19] theses, it may be said that small gap widths are preferable also for TEC. The effective gap width in the magnetic triode is, however, given by the length of the electron paths, which in this case cannot be smaller than the dimension of the emitter. As heat has to be transferred to the emitter and removed from the collector, the dimension of both can probably not be smaller than around 1 mm, which is too large for an efficient suppression of the space charge. Additionally, a region of space-charge accumulation due to intersecting electron paths may be created, which further lowers the current transferred to the collector.

Consequently, both triodes did not provide a satisfying solution to the space-charge problem.

2.2 A brief history of thermionic energy conversion

Thermionic emission was first reported by Edison and Preece [26] in 1885. Being crucial for electron tubes, thermionic emission became extremely important for electronics in the 20th century. Schlichter was the first one to publish the idea to convert heat to electricity using thermionic emission in 1915 [27], but intense research on the topic did not take place before the late 1950s, when several promising prototypes were reported [28–33].

Subsequent research concentrated on the cesium type TIC. During the Solar Energy Technology program, conducted by the Jet Propulsion Laboratory (USA), thermionic converters for solar energy harvesting were developed and tested [34]. Although typical lifetimes around 10 000 h and efficiencies ranging from 7 % to 10 % were achieved, the program was stopped in the 1970s.

Nuclear-powered TICs were investigated more intensely. The Atomic Energy Commission (USA), succeeded by the Department of Energy (DOE), carried out research on nuclear-powered TICs, which were intended both for space and terrestrial applications. The program ran from 1959 until 1973, when all research on space nuclear reactors was terminated [34].

After a period of very weak funding, a collaboration between the National Aeronautics and Space Administration (NASA), the DOE and the Defense Advanced Research Projects Agency re-entered the field in the 1980s with their SP-100 research initiative [35]. Being an alternative to thermoelectric converters, TICs were at that time considered as power sources for space missions [36]. Space missions far away from the sun, such as the Pioneer and Voyager space programs, and satellites frequently use radioisotope batteries as power sources. The decay heat generated therein is converted to electric energy, which is usually done with thermoelectrics. Owing to their high temperature suitability, TICs promise higher conversion efficiency. However – probably due to the higher reliability of thermoelectrics – research on TICs was quit in favor of thermoelectrics in the SP-100 program [34].

Unlike the NASA, the Soviet Union actually tested two TICs in space. After intense ground testing since around 1970, two so-called TOPAZ[1] reactors were flight-tested in 1987 and 1988 on the Plasma-A spacecraft [37]. Both converters completely fulfilled their test programs. Despite the related and somewhat advanced ENISEY system went through a round of successful ground tests in 1988, the Soviet program was discontinued in the same year [37].

[1] TOPAZ is a Russian acronym for *Thermionic power from the active zone* [34].

In a collaboration between Russia and the USA, the development of the ENISEY system, which was then called TOPAZ 2, was continued from 1991 until 1996 [35]. However, planned flight tests of converters already delivered to the USA were not carried out. This was due to a heavy dispute in the scientific community on the question, whether nuclear reactors should be launched into orbits around the earth at all [38].

In the beginning of the 21st century there seemed to be some upcoming interest in solar-powered cesium type converters for space applications in the course of the HPALM[2] program [39–41]. However, to my knowledge there have not been any publications on the concept since 2006.

The close-space concept was investigated in the late 1950s and early 1960s, but interest soon faded out in favor of the cesium type. However, in this period thorough theoretical understanding was obtained [42–49], and Hatsopoulos and Kaye realised a first proof-of-concept generator in 1958 [30].

The close-space concept has gone through a revival since around 2000, when new works were published on this topic [50–54]. This is probably due to improved machining techniques that might make the fabrication of those devices possible [55]. Current research on thermionics therefore seems to focus on this topic, in some cases pushing the gap width into the nanometer regime and exploiting tunneling phenomena this way [56–62]. In many cases, TICs are proposed as cooling devices [56–59, 63–66] instead of electricity generators.

However, the difficulties to maintain those tiny spacings at large temperature differences still remain, and no practical devices have been demonstrated yet.

[2] HPALM stands for *High Power Advanced Low Mass*, which refers to the comparatively low mass per output power offered by TICs.

3 Theoretical background of thermoelectronic energy conversion

In this chapter the theoretical background necessary to analyze the experimental results obtained in this thesis will be introduced stepwise. After discussing the field- and temperature-dependent emission of electrons from solids, the case of a two-electrode thermionic converter will be discussed in detail. Afterwards, the consequences of including a third electrode, the gate, will be described.

3.1 Emission of electrons from solids

The emission of electrons from solids is essential for any TIC. To remove an electron from a solid at 0 K, a minimum work, the so-called work function, must be spent to overcome the attractive forces of the ion cores and the image charge, and to move the electron across a dipole layer formed at the surface of the solid [67]. Analogically, the work function ϕ for finite temperatures and for an electrically neutral sample is defined as

$$\phi \equiv E_{\mathrm{vac}} - \mu,$$

with the vacuum level E_{vac} far outside the surface and the electrochemical potential μ inside the solid. By this definition the attractive force due to the image charge is included in the work function, which follows the tradition in this field of research. As the electrodes in a TIC are typically separated far enough from each other, this definition is more suitable than the other frequently used definition that does not include the image charge.

The energy required to remove an electron from the solid can be provided by various processes, the most fundamental ones of which are sketched in Figs. 3.1a to 3.1c. Besides the photoelectric effect, thermal emission, and field emission, combinations thereof can be realized, such as the Schottky emission sketched in Fig. 3.1e. Here, the work function is effectively lowered by an applied electric field, which permits electrons to overcome the barrier already at moderate temperatures.

Photon-enhanced thermionic emission (PETE, Fig. 3.1d), the combination of the photoelectric effect with thermal emission, is especially effective if the emitting material is a semiconductor [68, 69]. Incoming photons with sufficiently large energies excite electrons across the bandgap E_{gap}. If the lifetime of these electrons in the conduction band is sufficiently long, they thermalize there by electron-electron and electron-phonon interactions. The population of the conduction band must therefore be regarded as a somewhat independent thermodynamic ensemble, with its own effective electrochemical potential $\mu_{\mathrm{cb}} > \mu$. From the conduction band the electrons can then be emitted at intermediate temperatures, as the remaining work function barrier is reduced. As this mechanism permits to emit practically large current densities at intermediate temperatures, it seems to be an attractive option for solar TICs [69]. The increase of the efficiency arising from combining the PETE and TEC processes will be discussed in Ch. 6.3.

In practice, once an electron has left the solid its trajectory is strongly influenced by the electric field generated by preceding electrons. This space charge can only be neglected at very low emission currents or at very high external electric fields. Usually, electron-electron repulsion within the space charge causes the reflection of a fraction of all electrons back to the solid and thereby limits the emission current.

For the purpose of the following discussion of the space-charge-limited emission current, the accelerating electric field is assumed to be generated by applying a positive voltage V to a field generating anode[1] as it is sketched in Fig. 3.2a. For simplicity, the photoelectric effect is neglected in the following discussion.

The electric field any emitted electron is subjected to can be described as the superposition of the external electric field and the electric field generated by the space-charge cloud. For a fixed emitter temperature T_{e}, which determines the total number of electrons that have sufficient kinetic energy to escape from the emitter, there are four regimes of electron emission from solids (Fig. 3.2b). Those regimes are governed by the interplay of the external and the space-charge field and will be discussed for an increasing external electric field below.

Child-Langmuir regime

If the external field is weak, the space charge is dominant. Increasing T_{e} will hardly increase J, as any extra electron is reflected by the space charge. For the case of two infinite parallel plates separated by d and electrons leaving the emitter with zero kinetic energy,

[1] As will be shown later, the case of a positively biased collector is contradictory to thermionic energy conversion. Therefore, if the reader wants to identify the field generating electrode shown in Fig. 3.2a with a component of the TEC, they may please compare it to the gate.

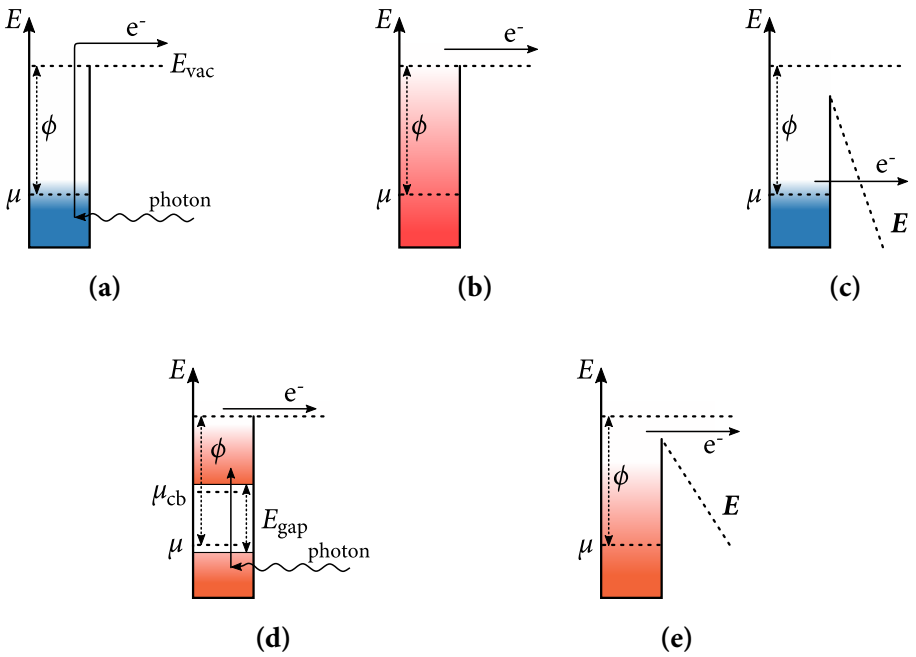

Figure 3.1: Sketches of emission processes of electrons from solids. The occupation of states is sketched as a vertical color gradient. **(a)** The photoelectric effect is the excitation of an electron by a photon to an energy high enough to overcome the work function [70]. **(b)** If the solid is sufficiently hot, some electrons can escape due to the thermal distribution [71–73]. **(c)** The work function barrier becomes thin, if a large electric field $\boldsymbol{E}$ is applied. This permits electrons to tunnel through the barrier; a process called Fowler-Nordheim emission [74]. **(d)** With semiconducting emitters the photoelectric effect can be combined with thermal emission, permitting the emission of electrons at intermediate temperatures and photon energies smaller than the work function [68, 69]. Incoming photons excite electrons across the band gap E_{gap}. If the lifetime of these electrons in the conduction band is sufficiently long, electrons thermalize within the conduction band. This thermalization occurs with respect to an effective electrochemical potential μ_{cb}, the height of which depends on the number of electrons in the conduction band. An intermediate temperature then permits electrons to overcome the remaining barrier. This photon-enhanced thermionic emission (PETE) is especially promising for TIC [69]. **(e)** Besides narrowing the work function barrier, an electric field also decreases the barrier height, which permits electrons to escape from the solid already at intermediate temperatures [75]. This so-called Schottky-emission can in principle be used in TECs to tailor the effective work function by an electric field.

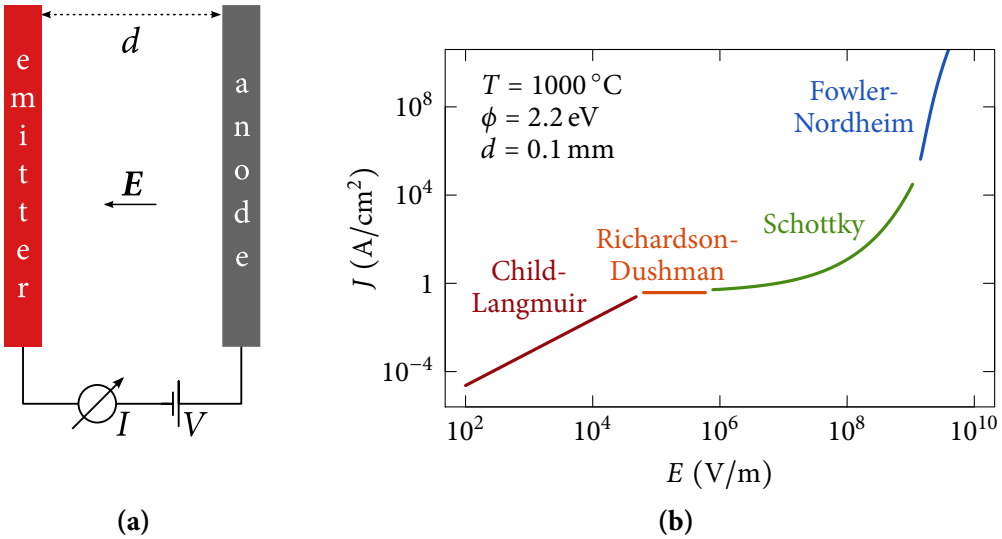

Figure 3.2: The E-field dependence of the emission of electrons from solids. **(a)** Sketch of a hypothetical setup to measure the emitted current density $J = I/A$ as a function of the applied electric field $\boldsymbol{E}$. **(b)** Calculated current density as a function of the applied electric field E for the four regimes of electron emission described within this chapter. The assumption of $d = 0.1\,\mathrm{mm}$ is required only for the Child regime.

the current density J can be calculated analytically, yielding the Child-Langmuir law for the current density reaching the anode [19, 22, 76, 77]:

$$J = \frac{4\varepsilon_0}{9}\sqrt{\frac{2e}{m_e}}\frac{V^{3/2}}{d^2}, \tag{3.1}$$

where ε_0 is the electric constant.

The thermal distribution of the initial electron velocities can be incorporated numerically, yielding some minor modifications to the Child-Langmuir law [19, 78].

Richardson-Dushman regime

Upon increasing the external field, it eventually becomes large enough to fully suppress the effect of the space charge. A plateau of the current density J as a function of the applied field is reached, because all electrons with sufficient energy to escape from the emitter

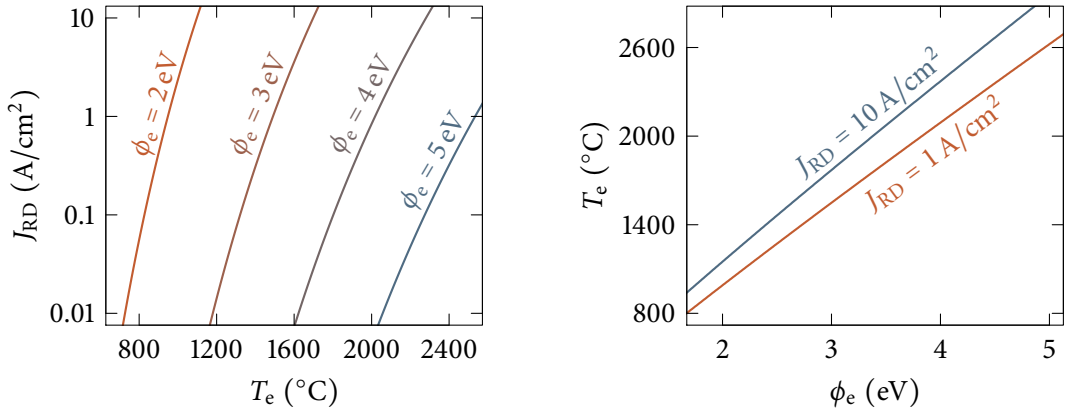

(a) **(b)**

Figure 3.3: Emission of electrons in the Richardson-Dushman regime. **(a)** Richardson-Dushman-limited current density J_{RD} as a function of emitter temperature T_e for a series of emitter work functions ϕ_e. **(b)** The temperature required for a desired current density can be obtained by numerically solving Eq. 3.2 for T_e. Typical values for TICs range from $J_{RD} = 1\,\mathrm{A/cm^2}$ to $10\,\mathrm{A/cm^2}$.

reach the anode. J can be calculated taking into account the thermal energy distribution of electrons within the emitter, yielding the Richardson-Dushman equation [71–73]:

$$J_{RD} = A_R T_e^2 \cdot \exp \frac{-\phi_e}{k_B T_e}, \tag{3.2}$$
$$A_R = \frac{4\pi m_e k_B^2 e}{h^3} = 1.202 \times 10^6 \frac{\mathrm{A}}{\mathrm{K^2 m^2}},$$

with the Planck constant h. In practice, the value for the Richardson constant A_R is often reduced as compared to the above given theoretical value. This is for example caused by a fraction of all electrons that approach the emitting surface with high enough kinetic energy being reflected back into the emitter.

The Richardson-Dushman regime is highly important for TICs, as it yields the maximum current density in absence of very high electric fields. Figure 3.3a shows the current density calculated from the Richardson-Dushman equation for a series of emitter work functions. Figure 3.3b shows the temperature required for emitted current densities of $1\,\mathrm{A/cm^2}$ and $10\,\mathrm{A/cm^2}$ – typical values for TICs – as a function of the emitter work function. As can be seen, temperatures exceeding 2000 °C are required for $J_{RD} \geq 1\,\mathrm{A/cm^2}$, if the work function is higher than approximately 4 eV.

Schottky regime

As sketched in Fig. 3.1e, increasing the external field beyond the Richardson-Dushman regime leads to a decrease of the height of the work function barrier by [22, 75]

$$\Delta\phi \approx \sqrt{\frac{e^3 E}{4\pi\varepsilon_0}},$$

which yields a slightly modified Richardson-Dushman-like equation:

$$J = A_\mathrm{R} T_\mathrm{e}^2 \exp \frac{-(\phi_\mathrm{e} - \Delta\phi)}{k_\mathrm{B} T_\mathrm{e}}.$$

Within the Schottky-regime tunneling of electrons through the work function barrier can still be neglected.

Fowler-Nordheim regime

Upon increasing the external field even further, the width of the work function barrier is eventually decreased far enough to permit tunneling through said barrier. This mechanism, sketched in Fig. 3.1c, then becomes the dominant emission process [74].

As within this work only moderate electric fields were applied, both the Schottky and the Fowler-Nordheim regimes are not accessible. However, Schottky emission may well be used to tailor the effective work functions in future TECs.

3.2 Thermionic energy conversion in ideal thermionic converters

Some fundamental concepts of thermoelectronic energy conversion can be discussed best for the simple two plate geometry of a TIC, where emitter and collector are assumed to be coplanar, quasi-infinite plates, without any gate in between and without any space charge hindering the transfer of electrons from the emitter to the collector. Throughout this work this hypothetical system is referred to as an ideal TIC. It can, in principle, be realized in a close-space type TIC having a gap width small enough to fully the suppress the effect of the space charge.

The work functions of both electrodes play a fundamental role for the conversion of energy. Hence, their influence will be discussed first.

Work function considerations

In Fig. 3.4 the build-up of surface charges upon electrically connecting two materials **A** and **B**, which for simplicity are assumed to be metals, with different work functions ϕ_A and ϕ_B is sketched. Those surface charges induce an electric field $\boldsymbol{E}$; an effect that has already been reported by Lord Kelvin [79] and is nowadays – among others – being employed in the context of Kelvin probe microscopy [80, 81].

This effect has an important consequence on thermionic energy conversion. Assuming sample **A** in Fig. 3.4b was used as the collector and **B** as the emitter of a TIC, emitted electrons would be pushed back to the emitter by the electric field $\boldsymbol{E}$. Only those electrons with kinetic energies high enough to overcome the barrier formed by the collector work function could cross the vacuum gap, which would be highly unfavorable. This yields a first important conclusion: in a TIC the collector work function must not be higher than the emitter work function.

In subsequent sections this is accounted for by identifying metal **A** as the emitter and metal **B** as the collector.

Ideal current-voltage characteristic

The dependence of the output current I_l on the load voltage V_l is a fundamental property of any TIC. Unless stated otherwise, the term IV characteristic is therefore identified with this dependence. Below, I will derive the IV characteristic of an ideal TIC.

If the emitter is heated to sufficiently high temperatures, electrons will be evaporated from the emitter, travel to the collector and condense there. If both electrodes are short-

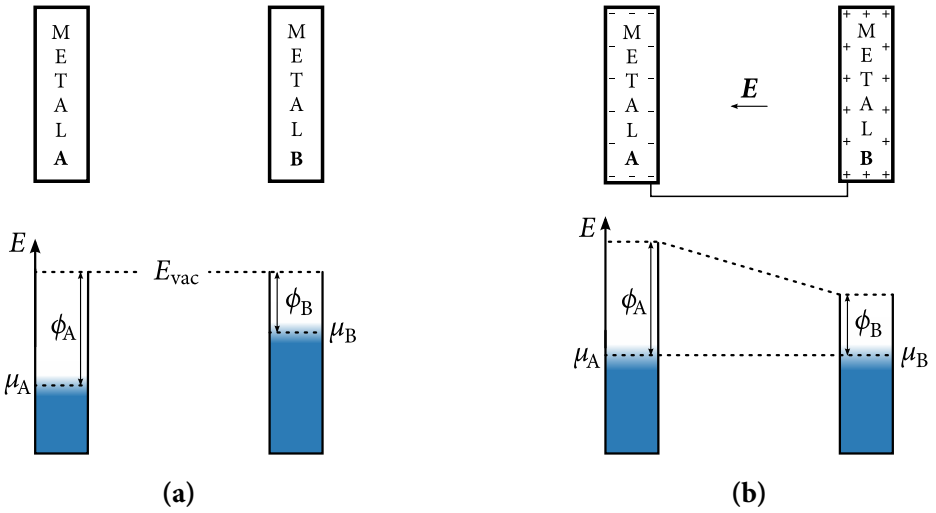

Figure 3.4: Sketch of the build-up of surface charges upon electrically connecting two metal samples **A** and **B** having different work functions $\phi_{\mathbf{A}} > \phi_{\mathbf{B}}$. The occupation of states is sketched as blue color gradient. **(a)** Initially, both metal samples are electrically neutral and there is no electrical connection between them. Hence, there is no electric field and the vacuum level is location independent. **(b)** After electrically connecting both samples, electrons can move from **B** to **A**, which is energetically favorable. In equilibrium, the electrochemical potentials have aligned, a net negative charge has accumulated in **A**, and a net positive charge has remained in **B**. The result is an electric field $\boldsymbol{E}$ pointing towards metal **A**.

circuited as is sketched in Fig. 3.5a, electrons can move back to the emitter without any change in their potential energy. The electrochemical potentials μ_e and μ_c are equal and no voltage is produced: $V_l = (\mu_c - \mu_e)/e = 0$.

If a small load resistor R_l is incorporated as sketched in Fig. 3.5b, electrons can no longer move back to the emitter without doing any work as they need to pass R_l. Instead, a voltage $V_l = (\mu_c - \mu_e)/e = R_l I_l > 0$ is built up, where I_l is the current transferred across the gap. Hence, the system generates an electric power $P_l = I_l V_l$. If R_l is slightly increased, the load voltage V_l also increases. Thereby I_l does not decrease, as there still is some electric field $\boldsymbol{E}$, which drags every evaporated electron onto the collector. The generated power $P_l = I_l V_l$ is therefore expected to increase linearly with the load voltage.

Upon further increasing R_l, eventually the optimum condition sketched in Fig. 3.5c is reached. Here the load voltage equals the difference in work functions

$$V_l = \frac{\phi_e - \phi_c}{e},$$

and consequently the gap is free of any electric field. Since every emitted electron has a non-zero velocity component pointing towards the collector, in an ideal TIC still all electrons will reach the collector.

This changes as soon as R_l is increased beyond the optimum condition. Electrons then have to overcome an electrostatic barrier $\phi_{barr} = \phi_c + eV_l - \phi_e$ as is sketched in Fig. 3.5d. Only electrons with kinetic energies higher than that barrier will still reach the collector. In this configuration ϕ_{barr} can be regarded as an additional work function, the effective work function then being $\phi_{eff} = \phi_e + \phi_{barr} = eV_l + \phi_c$. According to the Richardson-Dushman equation (Eq. 3.2), the current still reaching the collector is then given by

$$I_l = AA_R T_e^2 \exp\frac{-\phi_{eff}}{k_B T_e} = AA_R T_e^2 \exp\frac{-(eV_l + \phi_c)}{k_B T_e}, \tag{3.3}$$

where A is the emitter area.

Since this corresponds to an exponential drop of the current with increasing load voltage, the generated power reaches its maximum value at $V_l = V_{mp} \equiv (\phi_e - \phi_c)/e$, where mp stands for maximum power. Consistently, the optimum load resistance is referred to as R_{mp}. Figure 3.6 shows the $I_l(V_l)$ and $P_l(V_l)$ characteristics to be expected from this discussion.

In any real TIC, even in the regime $V_l < V_{mp}$ the current will not be exactly constant, but slightly vary with varying V_l. Throughout this work, the current that is obtained at $V_l = V_{mp}$ is denoted to as $I_{mp} \equiv I_l(V_l = V_{mp})$.

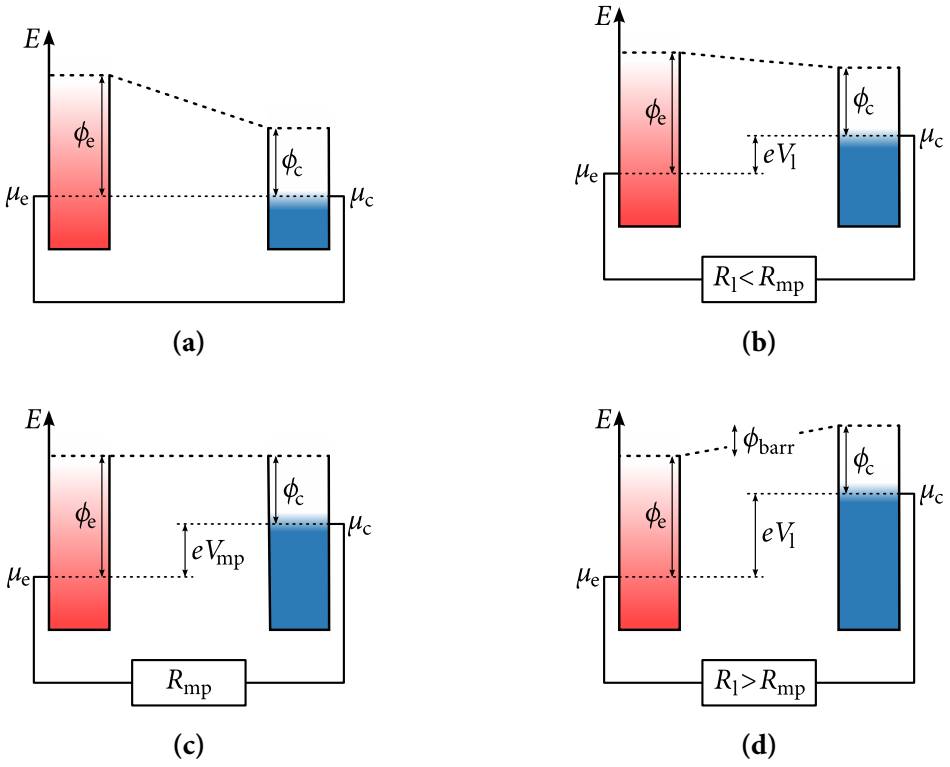

Figure 3.5: Sketches of the electron potential energy for a series of load resistances R_l. **(a)** $R_l = 0$. Once they have been evaporated and reached the collector, electrons can travel back to the emitter energetically neutrally. No load voltage is built up. **(b)** $0 < R_l < R_{mp}$. A non-zero load voltage V_l builds up. The rate of electrons reaching the collector does not decrease as compared to **(a)**. **(c)** R_l and thus V_l is further increased until the optimum condition $R_l = R_{mp}$ is reached, corresponding to $V_l = V_{mp} = (\phi_e - \phi_c)/e$. In an ideal TIC the collector current still does not decrease. **(d)** Pushing R_l beyond the critical condition exponentially decreases the load current as only electrons with thermal energies higher than the barrier ϕ_{barr} can still reach the collector.

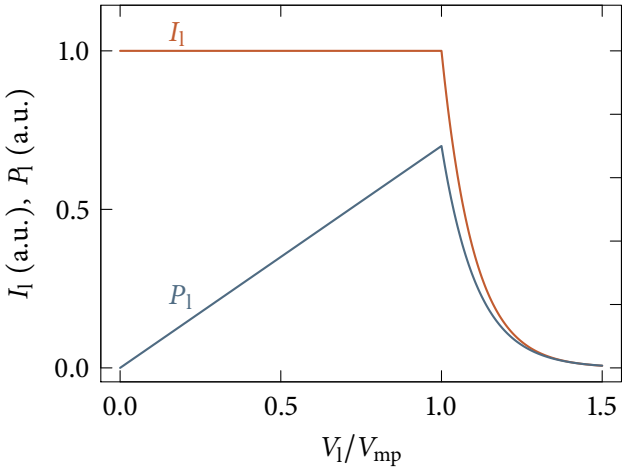

Figure 3.6: Ideal characteristics for the load current I_l and the load power P_l as a function of the load voltage V_l. For V_l exceeding the optimum value $V_{mp} = (\phi_e - \phi_c)/e$, the current I_l and thus the generated power $P_l = I_l V_l$ drop exponentially.

In principle, Eq. 3.3 gives a possibility to determine the collector work function by fitting the expected exponential behavior to a measured $I_l V_l$ characteristic. However, as will be discussed in Ch. 5.1, this approach fails if the velocity distribution of the electrons changes while they are transferred to the collector.

Efficiency of ideal TICs

Below, the efficiency of ideal TICs will be discussed on the basis of several publications thereon [22, 23, 82, 83]. In this chapter only the idealized case will be discussed, which in addition to the preceding chapter implies that the space charge is eliminated in an arbitrary process not consuming any heat or electric power. To give an example, this is again fulfilled in a close-space converter, if the gap width is maintained without providing an additional channel of heat conductance from the emitter to the collector.

As sketched in Fig. 3.7, heat is lost from the emitter by evaporation of electrons, thermal radiation, and conduction across the lead wires connecting the load with emitter and collector. Further heat losses, *e.g.*, due to mechanical supports of the emitter, are neglected as they can in principle be very small. The heat loss from the emitter due to thermal radiation and evaporation of electrons is transported to the collector.

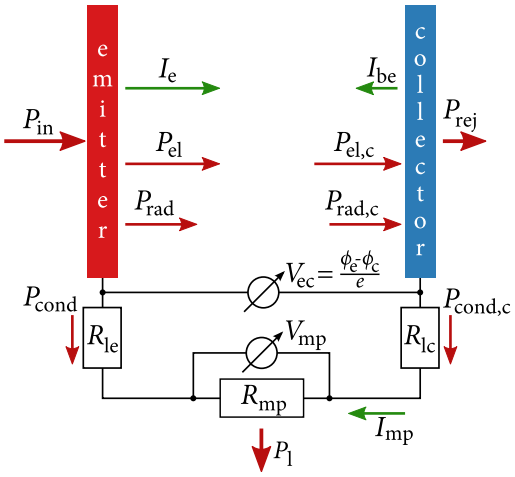

Figure 3.7: Sketch of energy flow (red arrows) and current (green arrows) channels relevant for TICs. Heat is removed from the emitter by electron cooling (P_{el}), thermal radiation (P_{rad}) and heat conduction (P_{cond}). The current across the vacuum gap and through the load is reduced by the back emission I_{be}, yielding $I_{mp} = I_e - I_{be}$. Furthermore, the usable voltage is reduced by the voltage drop V_{lead} across the lead resistances R_{le} and R_{lc}.

It is necessary to distinguish two cases with respect to this heat transported to the collector. If only the TIC is regarded, this heat is lost and the respective efficiency will be referred to as η_{tic}. If, alternatively, this heat is fed into a secondary heat engine, *e.g.*, a steam turbine, the total efficiency will be higher and referred to as η_{cc}, where cc stands for combined cycle.

As was discussed in the preceding section, an ideal TIC reaches the maximum of its output power at $V_l = V_{mp} = (\phi_e - \phi_c)/e$, where the local vacuum potential of emitter and collector are equal. Consequently, the load resistance is assumed to be chosen such that this criterion is fulfilled.

Stand-alone thermionic converters

As in an ideal TIC there is no space charge limiting the transfer of electrons across the vacuum gap, the complete emitted current I_e reaches the collector. Due to the low collector work function, a usually small current I_{be}– the so-called back-emission – is emitted from the collector as well, flows to the emitter, and thereby reduces the net current transported across the vacuum gap and through the load:

$$I_{mp} = I_e - I_{be}.$$

Both emitted currents are thereby given by the Richardson-Dushman equation (Eq. 3.2):

$$I_e = AA_R T_e^2 \cdot \exp \frac{-\phi_e}{k_B T_e},$$
$$I_{be} = AA_R T_c^2 \cdot \exp \frac{-\phi_c}{k_B T_c},$$

with A being the active area of both emitter and collector and T_e, ϕ_e, T_c, and ϕ_c the temperatures and work functions of emitter and collector, respectively. It is neglected that the effect of the back-emission slightly alters the load voltage, at which the output power is maximized. This is reasonable as this effect is negligible, if I_{be} is significantly smaller than I_e, which will be the case for any practical configuration.

The efficiency η_{tic} is defined as the fraction of the electric output power, which equals the power P_l delivered to the load, and the heat input:

$$\eta_{tic} = \frac{P_l}{P_{in}}, \qquad (3.4)$$
$$P_l = (V_{mp} - V_{lead}) I_{mp},$$

where V_{lead} is the voltage drop due to the finite resistances R_{le} and R_{lc} of the leads connecting emitter and collector with the load. As for the moment a stand-alone TIC is regarded and the heat transported to the collector is lost anyway, R_{lc} can be assumed to be arbitrarily low, in particular $R_{lc} \ll R_{le}$. Fully neglecting R_{lc} yields

$$P_l = [(\phi_e - \phi_c)/e - R_{le} I_{mp}] I_{mp}. \qquad (3.5)$$

In equilibrium, the heat input P_{in} compensates the sum of all channels of heat loss from the emitter:

$$P_{\mathrm{in}} = P_{\mathrm{rad}} + P_{\mathrm{el}} + P_{\mathrm{cond}}, \tag{3.6}$$

where P_{rad}, P_{el}, and P_{cond} are the heat losses due to thermal radiation, transport of electrons across the gap, and conduction across the lead. Notably, the electric output power P_{l} does not explicitly appear in this equation because it is included in the electronic term P_{el}.

The radiative heat loss P_{rad} is governed by the Stefan-Boltzmann law:

$$P_{\mathrm{rad}} = \sigma \varepsilon A \left(T_{\mathrm{e}}^4 - T_{\mathrm{c}}^4 \right) \tag{3.7}$$

with the Stefan-Boltzmann constant σ. The relevant effective emissivity ε of the electrode system typically equals 0.1 [23].

Emitted electrons remove an average thermal energy of $\phi_{\mathrm{e}} + 2k_{\mathrm{B}}T_{\mathrm{e}}$ from the emitter [19, 83], where $2k_{\mathrm{B}}T_{\mathrm{e}}$ is the average thermal energy exceeding the work function. Similarly, every back-emitted electron reaching the emitter deposits an average thermal energy[2] of $\phi_{\mathrm{e}} + 2k_{\mathrm{B}}T_{\mathrm{c}}$. Hence, the net heat loss due to electron transfer across the gap becomes:

$$P_{\mathrm{el}} = I_{\mathrm{e}}/e \cdot \left(\phi_{\mathrm{e}} + 2k_{\mathrm{B}}T_{\mathrm{e}}\right) - I_{\mathrm{be}}/e \cdot \left(\phi_{\mathrm{e}} + 2k_{\mathrm{B}}T_{\mathrm{c}}\right) \tag{3.8}$$

The heat conduction due to the electrical connection to the external load, which is assumed to be at an ambient temperature of $T_0 = 300\,\mathrm{K}$, is reduced by Joule heating within the lead, half of which is effectively transferred back to the emitter [19, 83]:

$$P_{\mathrm{cond}} = \left(T_{\mathrm{e}} - T_0\right)/R_{\mathrm{th,e}} - \frac{1}{2} I_{\mathrm{mp}}^2 R_{\mathrm{le}},$$

where $R_{\mathrm{th,e}}$ is the thermal resistance of the emitter lead. To minimize ohmic losses (see Eq. 3.5) good electrical conductances of the lead are favorable, while low thermal conductances minimize heat conduction losses. As metals provide the best ratio of electrical

[2] That the heat transported to the emitter by the back-emission depends on ϕ_{e} instead of ϕ_{c} might seem somewhat counterintuitive. However, just like every electron emitted from the emitter must remove at least ϕ_{e} in thermal energy, every condensed electron must deposit at least ϕ_{e}.

and thermal conductivity of all suitable materials, they are used in all practical TICs. With the Wiedemann-Franz law this permits to express $R_{\mathrm{th,e}}$ in terms of R_{le}:

$$R_{\mathrm{th,e}} = \frac{R_{\mathrm{le}}}{LT_{\mathrm{l}}},$$

with the theoretical Lorenz number $L = 2.44 \times 10^{-8}\,\mathrm{W\Omega K^{-2}}$ and the average lead temperature $T_{\mathrm{l}} = (T_{\mathrm{e}} - T_0)/2$ [82]. It is neglected that some metals show slightly different Lorenz numbers as the deviations are typically only small [84]. This yields:

$$P_{\mathrm{cond}} = \frac{L}{2R_{\mathrm{le}}}(T_{\mathrm{e}} - T_0)^2 - \frac{1}{2}I_{\mathrm{mp}}^2 R_{\mathrm{le}}. \tag{3.9}$$

Inserting Eqs. 3.5 to 3.9 into Eq. 3.4 yields a general expression for the efficiency of an ideal TIC:

$$\eta_{\mathrm{tic}} = \frac{[(\phi_{\mathrm{e}} - \phi_{\mathrm{c}})/e - R_{\mathrm{le}} I_{\mathrm{mp}}] I_{\mathrm{mp}}}{\sigma\varepsilon A(T_{\mathrm{e}}^4 - T_{\mathrm{c}}^4) + \frac{I_{\mathrm{e}}}{e}(\phi_{\mathrm{e}} + 2k_{\mathrm{B}}T_{\mathrm{e}}) - \frac{I_{\mathrm{be}}}{e}(\phi_{\mathrm{e}} + 2k_{\mathrm{B}}T_{\mathrm{c}}) + \frac{L(T_{\mathrm{e}}-T_0)^2}{2R_{\mathrm{le}}} - \frac{I_{\mathrm{mp}}^2 R_{\mathrm{le}}}{2}}, \tag{3.10}$$

which has been published in similar form by several authors [22, 23, 82, 83]. By replacing the currents in this equation by current densities and by expressing the resistances of the lead wires as conductances per emitting area, it can be shown that η_{tic} in fact does not depend on A.

Because of the huge parameter space, it is a non-trivial task to determine optimum values for the parameters R_{le}, T_{e}, T_{c}, ϕ_{e}, and ϕ_{c} from this equation. Historically, authors have approached this problem by neglecting one or more terms in Eq. 3.10 – usually the back-emission [82, 83] – or by using approximations considering the lead wires [22]. The omission of the back-emission is somewhat reasonable, as in the range of optimum efficiency it actually is small in most cases [82]. However, because errors arising therefrom might get large in the subsequent discussion of a combined-cycle system and because it is a less serious problem with modern computer technology, in this work the full model has been treated numerically. Throughout this work, the lead wire resistance has been optimized numerically wherever efficiencies are plotted or numeric values of efficiencies are given in the text.

It turns out that for any given set of ϕ_{e}, T_{e}, and T_{c} it is optimal to chose the smallest ϕ_{c} for which the back-emission is still much smaller than I_{e}. Further decreasing ϕ_{c} is counterproductive as I_{mp} then drops faster than V_{l} rises. For $T_{\mathrm{c}} = 100\,°\mathrm{C}$ it is optimal to chose $\phi_{\mathrm{c}} = 0.55\,\mathrm{eV}$, which is an extremely low value. However, although work functions

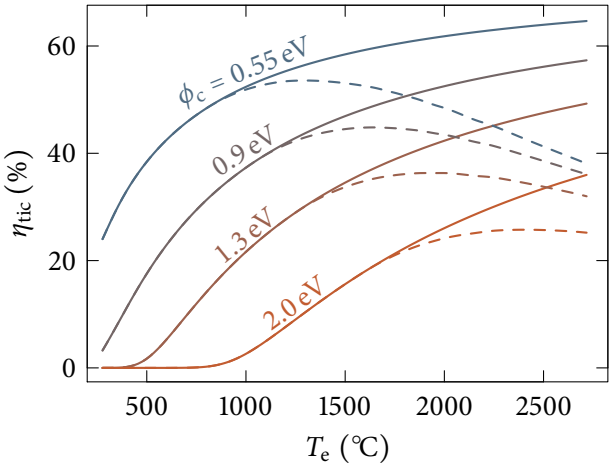

Figure 3.8: Conversion efficiency η_{tic} of an ideal stand-alone TIC plotted as a function of emitter temperature T_e for a series of collector work functions ϕ_c and for T_c = 100 °C, calculated from Eq. 3.10. To obtain the data shown here, the emitter work function was optimized for every T_e.
Limiting the current density to 10 A/cm^2 yields the dashed lines. The optimum of the efficiency is then obtained for $\phi_e \approx 2.3$ eV.
A work function of 0.9 eV has recently been reported for doped diamond systems [85], and 1.3 eV to 2.0 eV are typical values for alkaline-earth oxides on metals [86].

as low as that have not yet been achieved, there is no known physical reason prohibiting their realization. As Fig. 3.8 shows, for this optimum value of ϕ_c the calculation predicts efficiencies exceeding 60 %, which are obtained at an emitter work function around 3 eV.

Additionally, Fig. 3.8 shows that very high efficiencies can also be obtained for work functions that have already been demonstrated experimentally.

In practice, the condition of lossless space-charge suppression can only be fulfilled for finite current densities. Figure 3.8 additionally shows efficiencies that were calculated with the current being limited to 10 A/cm^2. As can be seen, in this case very high emitter temperatures have no benefits, as the resulting high current densities cannot be transferred to the collector.

Figure 3.9 shows the contribution of the individual loss channels to the total heat loss from the emitter for the example of ϕ_c = 0.9 eV. As can be seen, the heat carried away by emitted electrons is the most important contribution. This channel splits up into two subchannels, which represent the energy required to overcome the emitter work function (ϕ_e) and the average excess thermal energy ($2k_B T_e$) in Eq. 3.8. Thereby the ϕ_e-subchannel clearly dominates.

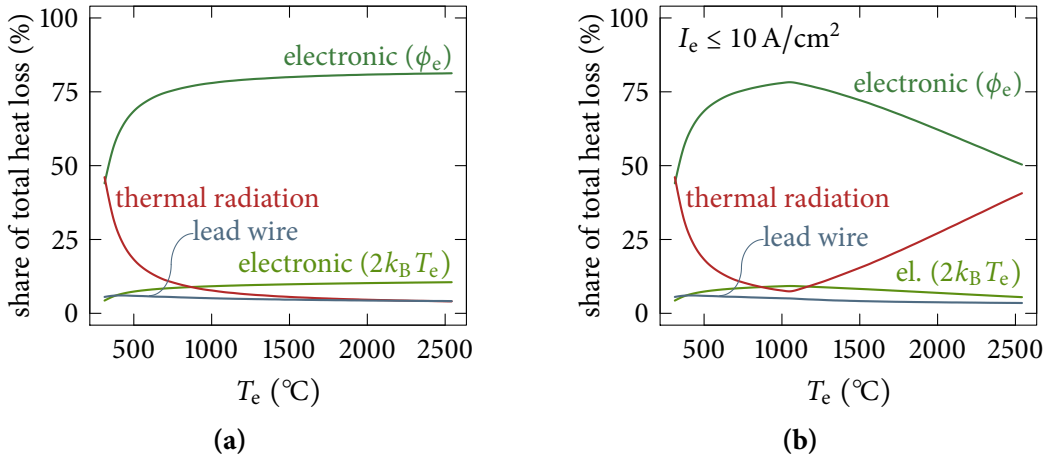

Figure 3.9: Relative importance of the channels of heat loss from the emitter as a function of the emitter temperature for the example $\phi_c = 0.9\,eV$ of the data shown in Fig. 3.8. The individual contributions were calculated from Eqs. 3.7 to 3.9 while neglecting the back-transport of energy from the collector via thermal radiation (the T_c^4-term in Eq. 3.7) and electron transport (the I_{be}-terms in Eq. 3.8). The electronic contribution is split up into the the two terms arising from the need to overcome the emitter work function (ϕ_e) and from the average thermal energy exceeding the work function barrier ($2k_B T_e$). **(a)** For $\phi_c = 0.9\,eV$ and an arbitrarily high emitted current density, corresponding to the solid line in Fig. 3.8. **(b)** For $\phi_c = 0.9\,eV$ and the emitted current density limited to $10\,A/cm^2$, corresponding to the dashed line in Fig. 3.8.

Interestingly, with increasing temperature the thermal radiation increases slower than the emitted current density does. Consequently, the relative importance of the thermal radiation decreases. However, if the temperature is increased beyond the temperature at which the emitted current density equals the maximum that can be transferred across the vacuum gap, the thermal radiation becomes relevant again. In Fig. 3.9b this is the case for $T_e > 1050\,°C$. Consequently, the thermal radiation leads to the decrease of the efficiency that can be observed in Fig. 3.8 (dashed lines).

Combined cycle systems

In the preceding discussion the possibility to drive a secondary heat-to-electricity converter with the waste heat produced by the TIC has not been considered, albeit it can significantly increase the total conversion efficiency. Several authors have mentioned the possible increase of the total conversion efficiency of such combined cycle systems [16, 55, 87], but to my knowledge no comprehensive discussion has been provided.

To discuss combined cycle systems in a practical way, the TIC is assumed to feed the heat rejected by the collector into either a large-scale steam-turbine working at an heat-to-electricity efficiency of $\eta_s = 35\,\%$ and receiving its heat at an upper temperature of 390 °C, or into a small-scale Stirling engine working at the same efficiency but receiving its heat at 700 °C. These are parameters typical for steam turbines and Stirling engines being used in operational CSP plants [8, 88]. Ideally, the collector temperature equals the inlet temperature of the secondary heat engine.

The additional electric power P_s generated by the secondary heat engine can be accounted for by introducing an additional term into the numerator of Eq. 3.4:

$$\eta_{cc} = \frac{P_l + P_s}{P_{in}} = \frac{P_l + \eta_s P_{rej}}{P_{in}},$$

where the heat power P_{rej} rejected by the collector in equilibrium is the sum of an electronic term, a radiation term and a conduction term, in analogy to the preceding discussion of P_{in}:

$$P_{rej} = P_{el,c} + P_{rad,c} - P_{cond,c}.$$

Here, the electronic and the radiative contribution both heat the collector, while the conductive contribution cools it:

$$\begin{aligned} P_{el,c} &= I_e/e(\phi_c + 2k_B T_e) - I_{be}/e(\phi_c + 2k_B T_c), \\ P_{rad,c} &= \sigma\varepsilon(T_e^4 - T_c^4), \text{ and} \\ P_{cond,c} &= \frac{L}{2R_{lc}}(T_c - T_0)^2 - (I_e - I_{be})^2 R_{lc}/2. \end{aligned}$$

As can be seen, the radiation term $P_{rad,c}$ heating the collector is exactly the same as P_{rad}, which cools the emitter. This is due to only those two components exchanging thermal radiation in an ideal TIC.

Since the lead connecting the collector with the load resistance cannot be neglected in the case of a combined cycle, P_l has to be slightly modified:

$$P_l = [(\phi_e - \phi_c)/e - (R_{le} + R_{lc})I_{mp}]I_{mp}.$$

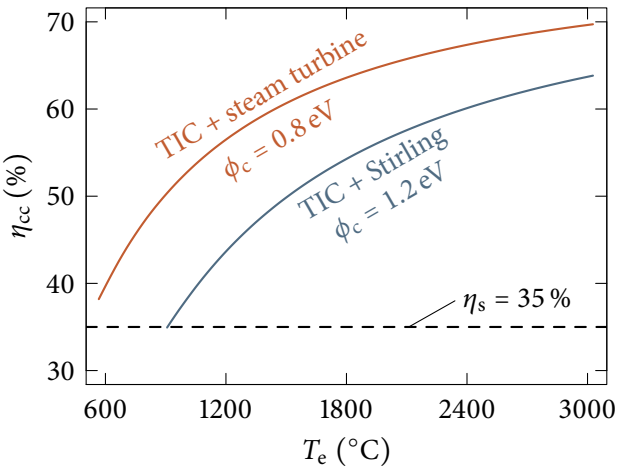

Figure 3.10: Total conversion efficiency η_{cc} of a combined cycle system consisting of an ideal TIC and a secondary heat engine ($\eta_s = 35\,\%$), as a function of emitter temperature T_e. The data were calculated from Eq. 3.11. The secondary heat engine is assumed to be either a steam turbine with an inlet temperature of $T_c = 390\,°C$ or a Stirling engine with $T_c = 700\,°C$. In both cases the collector is assumed to have the respective optimum work function of $\phi_c = 0.8\,eV$ (steam turbine) or $\phi_c = 1.2\,eV$ (Stirling engine). For each T_e the emitter work function was optimized.

The total efficiency of the combined-cycle process then becomes:

$$\eta_{cc} = \frac{P_l + \eta_s (P_{el,c} + P_{rad,c} - P_{cond,c})}{P_{in}}, \tag{3.11}$$

with P_{in} as in Eqs. 3.6 to 3.9.

Figure 3.10 shows the total efficiency obtained from Eq. 3.11 for the two cases of the TIC feeding its rejected heat either into a steam turbine or a Stirling engine. In both cases the collector is assumed to have the optimum work function for the respective inlet temperatures, which is $\phi_c = 0.8\,eV$ for the steam turbine and $\phi_c = 1.2\,eV$ for the Stirling engine.

As can be seen, adding a TIC to the already established thermal-to-electricity converters can substantially increase the total conversion efficiency. Furthermore, attractive conversion efficiencies can be achieved with substantially higher – and therefore far easier to realize – collector work functions than is the case for stand-alone TICs.

As the focus of this work is the suppression of the space charge by electric and magnetic fields, the availability of materials with low work functions will be treated only briefly in the outlook (Ch. 7).

Solar heating

In the preceding sections, the heat-to-electricity efficiencies of stand-alone and combined-cycle TICs were calculated. However, if the emitter is heated with solar radiation, the

light-to-electricity efficiency η_l may be a better measure of system performance. It is slightly reduced as compared to the heat-to-electricity efficiencies η_tic and η_cc, because light needs to be absorbed by the emitter. Consequently, the emitter must provide some highly light-absorbing area A_b, where b stands for black. As this black spot has a high emissivity, thermal radiation from A_b constitutes an additional channel of heat loss $P_\mathrm{b} = A_\mathrm{b}\sigma T_\mathrm{e}^4$.

η_l can be expressed in terms of the heat-to-electricity efficiency η, where η can stand both for η_tic and η_cc, as follows:

$$\frac{\eta_\mathrm{l}}{\eta} = \frac{P_\mathrm{out}/(P_\mathrm{in} + P_\mathrm{b})}{P_\mathrm{out}/P_\mathrm{in}} = \frac{1}{1 + P_\mathrm{b}/P_\mathrm{in}}, \tag{3.12}$$

where P_out is either the output power of the stand-alone TIC or of the combined cycle.

In the steady state, the light input from the sun must equal the heat input power of the TIC or combined cycle plus the additional heat loss due to the black spot. With the light concentration c and the intensity of the incident, not yet concentrated sunlight I_sun this yields:

$$\begin{aligned} A_\mathrm{b} c I_\mathrm{sun} &= P_\mathrm{in} + P_\mathrm{b} = P_\mathrm{in} + A_\mathrm{b}\sigma T_\mathrm{e}^4 \\ \Rightarrow \frac{A_\mathrm{b}}{P_\mathrm{in}} &= \frac{1}{c I_\mathrm{sun} - \sigma T_\mathrm{e}^4} \\ \Rightarrow \frac{P_\mathrm{b}}{P_\mathrm{in}} = \frac{A_\mathrm{b}\sigma T_\mathrm{e}^4}{P_\mathrm{in}} &= \frac{\sigma T_\mathrm{e}^4}{c I_\mathrm{sun} - \sigma T_\mathrm{e}^4} = \frac{1}{c I_\mathrm{sun}/(\sigma T_\mathrm{e}^4) - 1} \end{aligned}$$

inserting this into Eq. 3.12 yields a surprisingly simple relationship:

$$\frac{\eta_\mathrm{l}}{\eta} = 1 - \frac{\sigma T_\mathrm{e}^4}{c I_\mathrm{sun}}. \tag{3.13}$$

With solar heating the efficiencies of both stand-alone and combined-cycle generators are thus reduced by the ratio of the intensities of the thermal radiation from the black spot and the incoming, concentrated sunlight.

Figure 3.11 shows the ratio η_l/η as a function of the emitter temperature for a series of light concentration factors c. As can be seen, in order to achieve high efficiencies at high emitter temperatures, high concentration factors are required. Today, concentration factors of up to 3000 are readily achieved [9], and 10000 seems to be technically possible [89]. The fundamental limit in media with a refractive index of 1 is given by $c_\mathrm{max} \approx 46000$ [90].

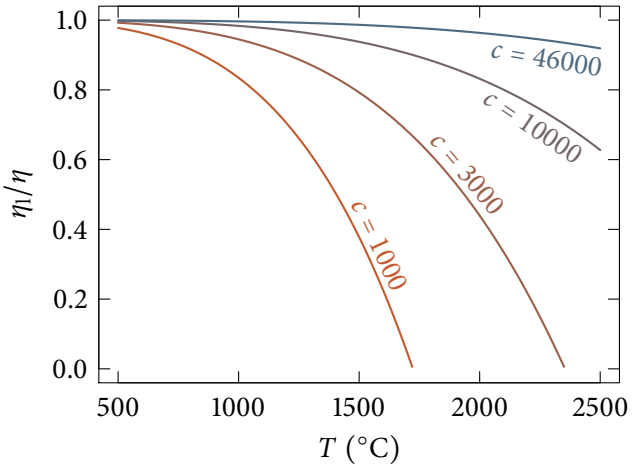

Figure 3.11: Ratio of sunlight-to-electricity efficiency η_l and heat-to-electricity efficiency η as a function of emitter temperature for a series of light concentration factors c. Data were calculated from Eq. 3.13. c_{max} = 46000 corresponds to the optical limit in media with a refractive index of 1 [90]. A solar intensity of 900 W/cm^2 was assumed, corresponding to the AM1.5 direct+circumsolar reference spectrum [91].

3.3 Thermoelectronic energy conversion

In the preceding discussion of an ideal TIC, electron-electron repulsion in the interelectrode space has been neglected. In reality, however, emitted electrons are pushed back by the space-charge cloud formed by electrons in front of them and are reflected if their kinetic energy is too low to overcome this repulsion.

The space charge modifies the electron potential energy in the interelectrode space. As compared to the idealized case of Fig. 3.5c, an energy barrier E_{sc} has to be introduced as shown in Fig. 3.12. In case of practical emitted current densities this barrier is high enough to block the vast majority of all electrons.

The suppression of the space charge by a gate within a TEC consisting of coplanar, infinite plates will be discussed below. The gate is supposed to be a hypothetical metal foil that is perfectly transparent for electrons. Although such an ideal gate does not exist in reality, this discussion will yield important insights. As can be seen from Fig. 3.13, the system is translation invariant along the x- and y-directions. This permits to treat the ideal TEC as one-dimensional along the z-direction.

The electric field generated by the gate accelerates electrons away from the emitter. They pass through the gate and when approaching the collector they are decelerated to their initial velocity. This process is virtually lossless and decreases the effects of the space charge in two distinct ways:

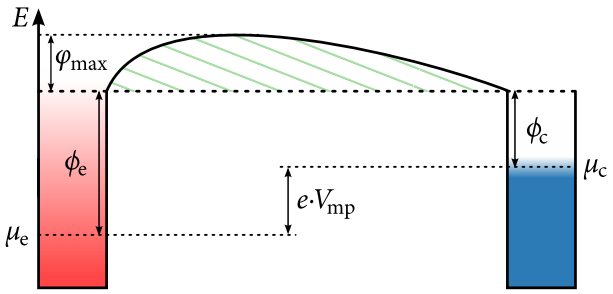

Figure 3.12: Sketch of the potential energy of an electron within a TIC. If there was no space charge, electrons could travel field-free from the emitter to the collector (dashed line). Due to the electron-electron repulsion, the space charge causes a potential barrier φ_{max} in the electron potential energy (solid line). Only electrons with high enough kinetic energy overcome the barrier. Reflection of low energy electrons at the barrier both lowers the collector current and leads to an even higher space-charge density near the emitter. The space-charge profile shown here was calculated by C. Stephanos [19].

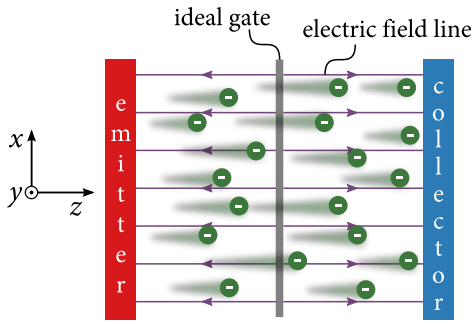

Figure 3.13: Sketch of a TEC with an ideal gate. The ideal gate is a hypothetical metal foil that is transparent for electrons. Just like the electrodes in a plate capacitor, the ideal gate and the plane-parallel, infinite emitter and collector electrodes generate a homogeneous electric field. Consequently, the system is translation invariant along the x- and y-directions, and it can be treated as one-dimensional. The magnetic field is not shown here.

First, the accelerated electrons pass through the vacuum gap at a high average velocity. Due to the 1-dimensionality of the problem, in dynamic equilibrium the equation of continuity requires the electron current density J to be independent of the position z within the gap. Neglecting the thermal velocity distribution of the emitted electrons and assuming them all to move at the same velocity $v(z)$ yields

$$J = n_e(z)ev(z) = -\rho_{sc}(z)v(z),$$

with n_e and ρ_{sc} being the electron-number density and the space-charge density, respectively. The space-charge density is therefore inversely proportional to the velocity:

$$\rho_{sc}(z) = -\frac{J}{v(z)}.$$

The space-charge contribution to the electric potential $\varphi(z)$ in the interelectrode space is given by Poisson's equation:

$$\nabla^2\varphi(z) = \frac{\mathrm{d}^2}{\mathrm{d}z^2}\varphi(z) = -\frac{\rho_{sc}(z)}{\varepsilon_0} = \frac{J}{\varepsilon_0 v(z)}. \tag{3.14}$$

Here the one-dimensionality of the problem, which leads to $\frac{\mathrm{d}^2}{\mathrm{d}x^2}\varphi(z) = \frac{\mathrm{d}^2}{\mathrm{d}y^2}\varphi(z) = 0$, was utilized. As can be seen, the curvature of the electric potential is inversely proportional to the velocity.

Owing to the boundary conditions given by the surfaces of emitter and collector, the value of φ is fixed at those positions. Therefore, a higher average velocity due to the gate – resulting in a smaller curvature of $\varphi(z)$ – directly leads to a smaller peak height. This effect is demonstrated in Fig. 3.14a.

Second, due to the superposition of the space-charge potential with the gate's electric potential, the total electric potential is reduced. Even if there was no reduction of the space charge by the increased velocity, the superposition of gate and space-charge potential would already reduce the space-charge barrier. This effect is demonstrated in Fig. 3.14b.

In sum, for a fixed current density the acceleration of electrons in the electric potential of the gate lowers the space-charge barrier or even completely suppresses it as sketched in Fig. 3.14c. Consequently, if the electron emission has not yet reached its Richardson-Dushman saturation value (see Ch. 3.1), the current density will increase.

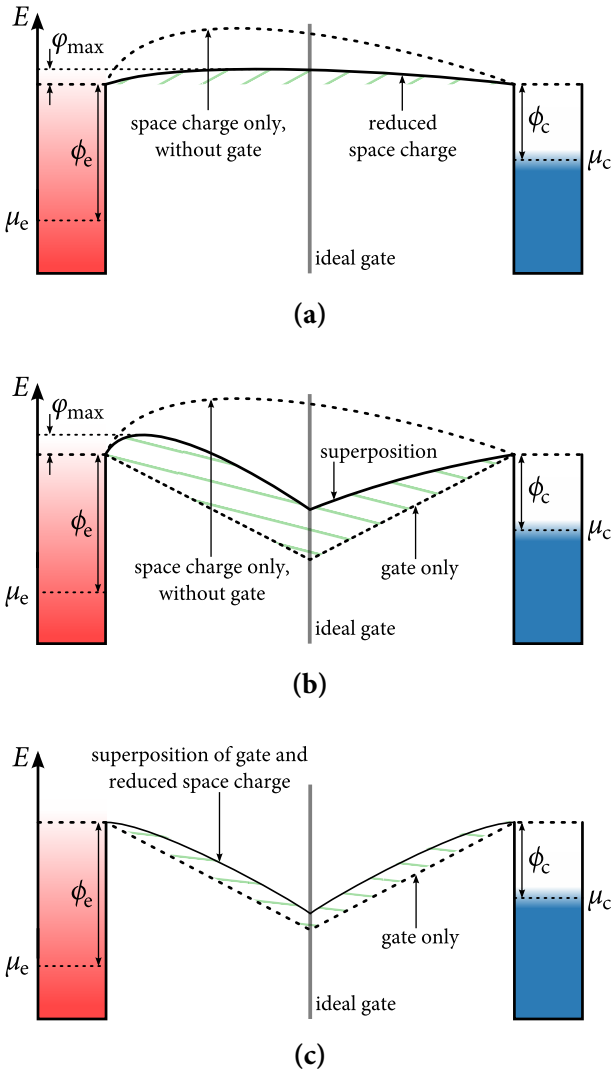

Figure 3.14: Sketches of the potential energy of an electron within a TEC. The two different contributions of the gate electric field are demonstrated separately. **(a)** By increasing the average velocity of electrons in the interelectrode space, the gate decreases the curvature of the electric potential in accordance to Eq. 3.14 and thus the height of the barrier. **(b)** Even if the increased velocity did not reduce the barrier, the superposition of space-charge and gate potential would already lower the barrier in the total potential energy. **(c)** The total effect of the gate is given by the superposition of the reduced space-charge with the gate potential. In this case, the current-limiting peak has completely disappeared.

One-dimensional calculation of the gate-enhanced thermoelectronic current density

As has been discussed in the previous section, the gate reduces or completely annuls the space-charge barrier for a given current density. The resulting increased current density then creates a new space-charge barrier, which again alters the current density. As can be seen, the shape of the space charge and the current density strongly depend on each other. The current density resulting for a given geometry and gate voltage can therefore only be calculated in a self-consistent way, which will be briefly sketched in this chapter. A more detailed discussion of this calculation is given by C. Stephanos [19].

In a first step, the thermal energy distribution of the electrons constituting the current will be neglected. This is reasonable, as the thermal distribution has a typical width of only about 0.1 eV, while electrons typically gain several eV in the electric field of the gate.

For a given current density J the total electric potential $\varphi(z)$ in the interelectrode space can then be calculated from Eq. 3.14, yielding

$$\varphi(z) = \varphi_{\text{gate}}(z) \underbrace{+\frac{J}{\varepsilon_0} \iint_0^z \mathrm{d}\tilde{z}^2 \frac{1}{v(\tilde{z})}}_{\text{space charge}} . \tag{3.15}$$

The velocity $v(\tilde{z})$ can thereby be calculated from the kinetic energy:

$$\frac{1}{2} m_\mathrm{e} \tilde{v}^2 = E_{\text{kin}} = E_{\text{start}} - E_{\text{pot}} = E_{\text{start}} + e\varphi(\tilde{z}),$$

yielding

$$v(\tilde{z}) = \sqrt{\frac{2}{m_\mathrm{e}} (E_{\text{start}} + e\varphi(\tilde{z}))}. \tag{3.16}$$

where E_{start} is the initial kinetic energy of the electrons. By inserting Eq. 3.16 into Eq. 3.15, a differential equation for the total electric potential is obtained:

$$\varphi(z) = \varphi_{\text{gate}}(z) + \frac{J}{\varepsilon_0} \sqrt{\frac{m_\mathrm{e}}{2}} \iint_0^z \mathrm{d}\tilde{z}^2 \frac{1}{\sqrt{E_{\text{start}} + e\varphi(\tilde{z}))}}. \tag{3.17}$$

For an ideal gate positioned symmetrically in between emitter and collector, and appropriate boundary conditions with the approximation $E_{\text{start}} = 0$, this equation can be

solved analytically (see the work of C. Stephanos [19]), yielding both the shape of the total potential

$$\varphi(z) = \frac{3}{4} V_\mathrm{g} \left(\frac{d_\mathrm{ec}}{2} \right)^{-4/3} \cdot \begin{cases} z^{4/3} & \text{for} \quad 0 \leq z \leq \frac{d_\mathrm{ec}}{2} \\ (d_\mathrm{ec} - z)^{4/3} & \text{for} \quad \frac{d_\mathrm{ec}}{2} < z \leq d_\mathrm{ec} \end{cases} \tag{3.18}$$

and the current density

$$J = 4\varepsilon_0 \sqrt{\frac{e}{6m_\mathrm{e}}} \frac{V_\mathrm{g}^{3/2}}{d_\mathrm{ec}^2}, \tag{3.19}$$

with the emitter-collector spacing d_ec.

The total electric potential is plotted alongside the gate potential in Fig. 3.15a and the current density is shown as a function of the gate voltage and gap width in Figs. 3.15b and 3.15c, respectively.

As the thermally distributed initial velocity of evaporated electrons has been neglected, the results presented so far are expected to underestimate the current density. The thermal distribution can be accounted for by replacing the integrand in Eq. 3.17 by an integral over the half-Maxwellian distribution function [19, 22]

$$f(E_\mathrm{start}) = 2 \left(\frac{m_\mathrm{e}}{2\pi k_\mathrm{B} T_\mathrm{e}} \right)^{3/2} \cdot \exp \frac{-E_\mathrm{start}}{k_\mathrm{B} T_\mathrm{e}},$$

yielding:

$$\varphi(z) = \varphi_\mathrm{gate}(z) + \frac{\sqrt{m_\mathrm{e}}}{\varepsilon_0 \sqrt{2}} \iint_0^z \mathrm{d}\tilde{z}^2 \int_0^\infty \mathrm{d}E_\mathrm{start} \frac{j(E_\mathrm{start}) f(E_\mathrm{start})}{\sqrt{E_\mathrm{start} + e\varphi(\tilde{z})}}, \tag{3.20}$$

where $j(E_\mathrm{start})$ is the infinitesimal contribution of the energy component E_start to the total current density.

Methods to numerically solve this equation as well as obtained solutions are presented in detail by C. Stephanos in [19]. For comparison, the current density resulting from the calculations presented there is also shown as a function of the gate voltage V_g and the gap width d_ec in Figs. 3.15b and 3.15c, respectively. As expected, neglecting the thermal distribution slightly underestimates the current density, but it does not alter the general behavior as a function of V_g or d_ec.

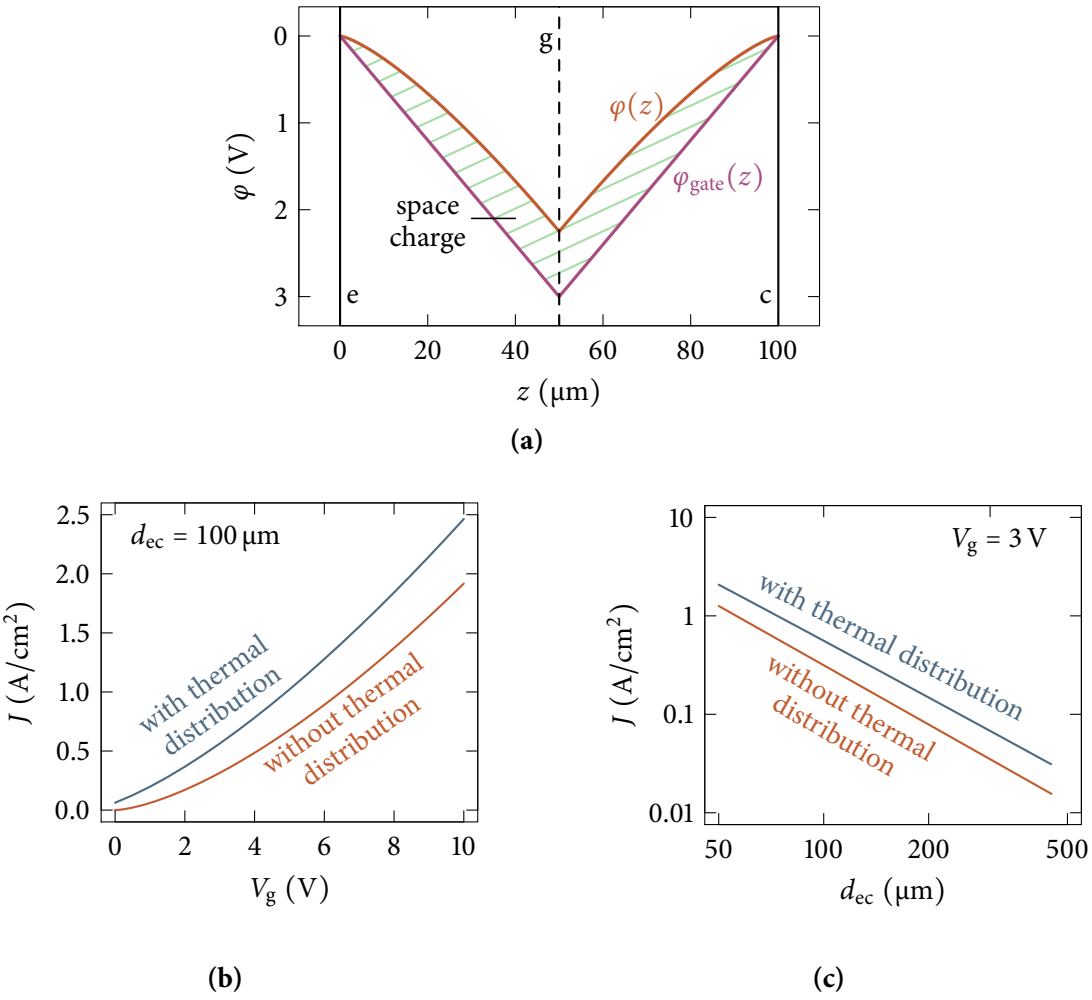

Figure 3.15: Results of one-dimensional calculations of the space charge for an ideal gate. **(a)** An ideal gate creates a linear electric potential $\varphi_{\text{gate}}(z)$, which leads to the presented shape of the total potential $\varphi(z)$ (Eq. 3.18). Here the thermal distribution of electron energies was neglected. Because the electron potential energy is proportional to the negative value of the electric potential, the $\varphi(z)$-axis is reversed. The positions of emitter (e), gate (g), and collector (c) are indicated as solid and dashed lines, respectively. The current density J (Eq. 3.19) resulting from this calculation is shown as a function of the gate voltage V_g (**b**) and gap width d_{ec} (**c**) both for the case of neglected (Eq. 3.19) and non-neglected (Eq. 3.20) thermal distribution. The results shown here were obtained by C. Stephanos [19].

Optimization of the gate position

In an optimized TEC, the gate voltage will be just high enough to exactly suppress the formation of a space-charge-induced peak in the electron potential energy. Higher gate voltages do not increase the current density[3], and lower gate voltages cause the formation of a space-charge peak and therefore result in a substantially decreased current density.

If the gate – with the optimum gate voltage applied – is positioned in the center between emitter and collector, the potential energy will have a symmetrical shape. If the gate is moved away from the center towards the emitter, two effects lead to the formation of a peak in the electron potential energy on the collector side, and hence to a reduction of the current density:

First, after moving the gate the electrons travel slower in the region $d_{\mathrm{ec}}/2 < z < d_{\mathrm{ec}}$, leading to a higher curvature of the electric potential $\varphi(z)$ in accordance with Eq. 3.14. Yet, as before the gate was moved the curvature was just small enough to not cause a peak, any higher curvature leads to the formation of a peak.

Second, the gate contribution to the total electric potential has a smaller slope near the collector after the gate has been moved. Even if the curvature of $\varphi(z)$ had not changed upon moving the gate, this would already lead to the formation of a peak in the total potential energy.

For the same two reasons, moving the gate in the opposite direction towards the collector causes the formation of a space-charge peak on the emitter side. Because any peak in the electron potential energy reduces the current transferred to the collector, it is best to position the gate in the center.

It should be noted that this is only approximately true if the TEC is not optimized, and the gate voltage is therefore not high enough to suppress the space-charge peak even if the gate is positioned in the center. In this case, it is favorable to slightly move the gate towards the emitter as this suppresses the remaining peak there. However, upon moving the gate a second peak near the collector will soon develop. This method was therefore not used in the work done within this thesis.

[3] A possible Schottky emission is neglected here.

3.4 The current tube method

In the previous chapter, C. Stephanos' models to predict the current across the vacuum gap of a TEC for an ideal gate were described. Obviously, experiments can only be performed with real gates, which generate inhomogeneous electric fields.

To account for those inhomogeneities and to predict the current to be expected in my measurements, an enhanced model was conceptualized in collaboration with C. Stephanos and implemented in the course of this thesis. This model extends the 1D calculations to a quasi-3-dimensional model by dividing the interelectrode space into straight tubes, which are arranged along the emitter-collector axis and cross the complete vacuum gap, as sketched in Fig. 3.16.

Upon following the magnetic field lines, each electron is assumed to travel from the emitter to the collector within exactly one tube. Thereby, due to the magnetic field forcing the electrons on helical paths, the x- and y-components of the E-field are assumed to have no influence of the movement of electrons along the tubes. Additionally, E_z is assumed to be constant over the tube cross section, which permits the current within each tube to be calculated from the one-dimensional equations derived above. The space-charge density is thereby assumed to be approximately constant along the x- and y-directions.

To determine the total current for a given TEC configuration, the electric field distribution is calculated using the commercial electric field solver IES COULOMB [92]. As the 1D model is valid only for the case of an ideal gate, the electric field within each tube needs to be averaged as sketched in Fig. 3.17. The current within each tube can then be estimated from the averaged E-field using the 1D solutions to Eq. 3.17. The current within one gate mesh is then obtained by summing up all corresponding tubes. Finally, multiplying the current within one gate mesh by the total number of meshes yields the total current.

Obviously, this model is based upon some simplifications, which will somewhat limit its validity. However, it offers an elegant way to model the current in presence of exper-

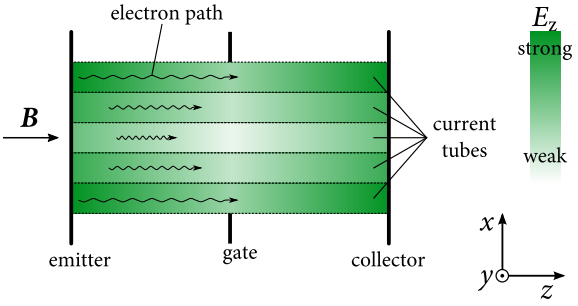

Figure 3.16: Sketch of the subdivision of the interelectrode space into current tubes. The electric field is assumed to be constant over the tube cross section. Typically, E_z is strong near the emitter and the collector, and within tubes passing close to the gate wires. Consequently, electrons move faster near the gate wires.

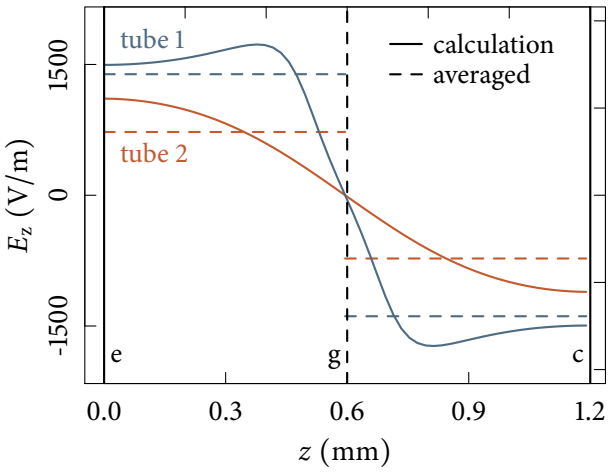

Figure 3.17: Calculated electric field E_z (solid lines) along two exemplary tubes and the averaged fields (dashed lines), which are used in the 1D models to predict the current density within each tube. The positions of emitter (e), gate (g), and collector (c) are indicated as vertical solid and dashed lines, respectively. In the example shown, a gate voltage of 1 V was applied and the mesh diameter (see Ch. 4.3) was 1.6 mm. The data were calculated with IES COULOMB [92].

imentally inevitable inhomogeneities in the electric field. The results obtained with the current tube method can hardly be interpreted without comparing them to my measurements. Consequently, they will not be discussed here, but in Ch. 6.

4 Experimental setup and material choices

In this chapter I will present the experimental setup that was developed during the course of this work and used to obtain the experimental results presented in Ch. 5 and Ch. 6. After giving an overview of the setup in general, I will discuss the most important components – emitter, gate, and collector – in detail. At some places, preliminary experiments demonstrating the functionality of the components will be presented.

4.1 Overview

To guarantee sufficiently large mean free paths of the electrons, the experiment is mounted inside a vacuum chamber, which is evacuated by a turbomolecular pump. The mean free path of electrons at the resulting base pressure of 1×10^{-7} mbar is in the order of several thousand meters [93], which guarantees ballistic transport from the emitter to the collector.

Fig. 4.1 shows a photograph of the vacuum chamber. The components shown there will be discussed in this chapter. The experiment is mounted on the inside of a DN200 CF vacuum flange, which itself is attached to a transfer system. As all electrical connections to the experiment are realized via electrical feedthroughs incorporated into the main flange, the emitter-gate-collector assembly can be moved out of the vacuum chamber to allow for modifications. Figure 4.2 shows a photograph of the vacuum chamber with the experiment in position for maintenance.

As is sketched in Fig. 4.3, the emitter, gate, and collector are mounted on a perforated ceramic plate, which permits to independently mount them in various positions on the plate. They are electrically connected via the steel screws below the ceramic plate, typically using two wires attached to two screws per component (not shown in Fig. 4.3) to permit four-terminal sensing of currents and voltages.

The required magnetic field is generated by two stacks of permanent magnets made of NdFeB, which are the strongest type of commercially available permanent magnets [94,

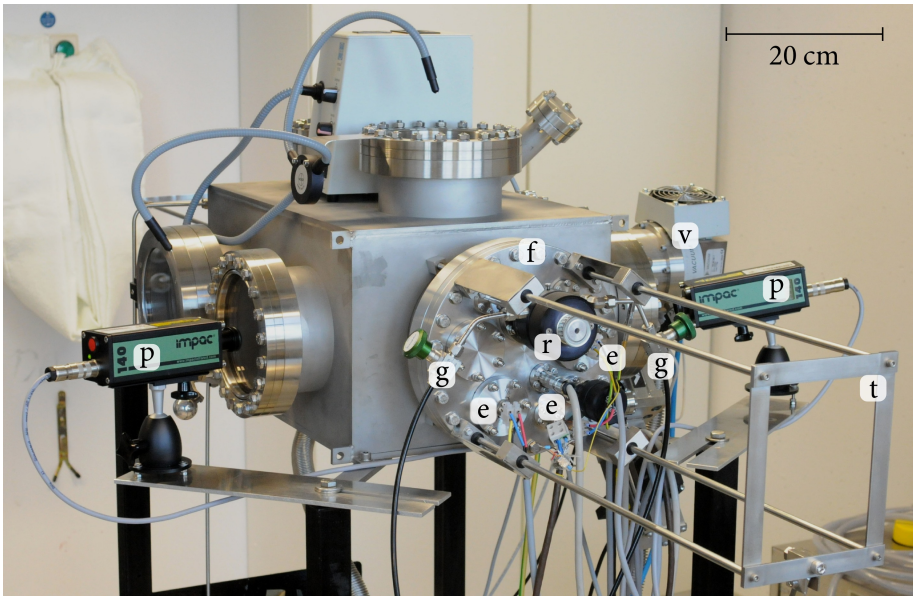

Figure 4.1: Photograph of the vacuum chamber housing the experimental setup. The main experiment is mounted on the inside of a DN200 CF vacuum flange (f), which is attached to a transfer system (t). Further visible components: pyrometers (p), turbomolecular pump (v), rotary feedthrough for the magnetic system (r), gas inlets (g), and several electrical feedthroughs (e). Photograph by K. Wiedenmann.

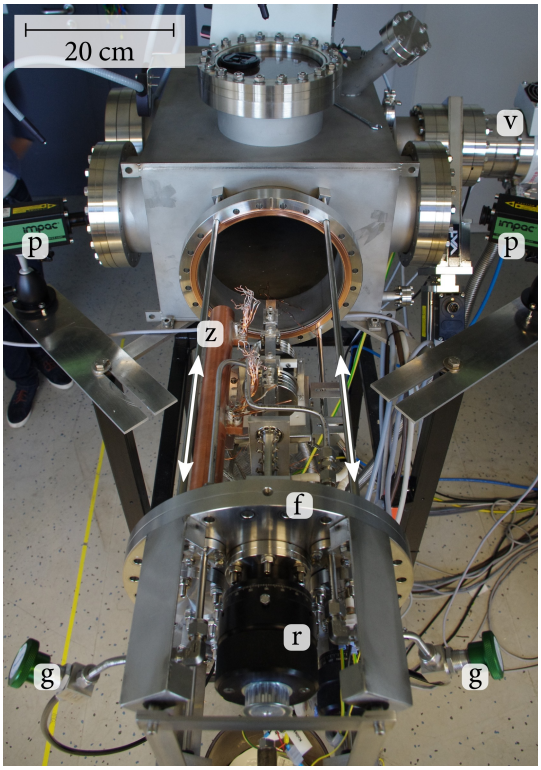

Figure 4.2: Photograph of the vacuum chamber with the experiment in position for maintenance. As is indicated, the vacuum flange (f) carrying the main experiment can be moved along the shafts, which permits to bring it into a position that allows for modifications. Further visible components: pyrometers (p), turbomolecular pump (v), rotary feedthrough for the magnetic system (r), gas inlets (g), and the copper cylinder (z) that serves to cool the magnets.

95]. As compared to electromagnets, these magnets have the advantage that magnetic fields with flux densities exceeding 100 mT can easily be achieved. Generating these flux densities with electromagnets is a demanding engineering task; in particular in vacuum, where it is complicated to remove the heat generated by the high required currents. Consequently, electromagnets were not considered as an option. The magnets are held by an iron yoke, which provides a low reluctance path for the magnetic flux, and thereby both decreases the stray magnetic field and increases the magnetic flux density in the region between both magnets. The yoke is mounted on a rotary feedthrough, which permits to rotate the magnets away from the emitter-gate-collector assembly *in situ*. Consequently, measurements with and without magnetic field can be performed consecutively without breaking the vacuum in between.

Figures 4.4a and 4.4b show photographs of the main experiment with the magnets being in position for measurements with and without magnetic field. The generated magnetic field was measured with a commercial hall effect sensor, which yields an approximately homogeneous magnetic flux density of order 200 mT varying by about ±10 mT across the gate cross section.

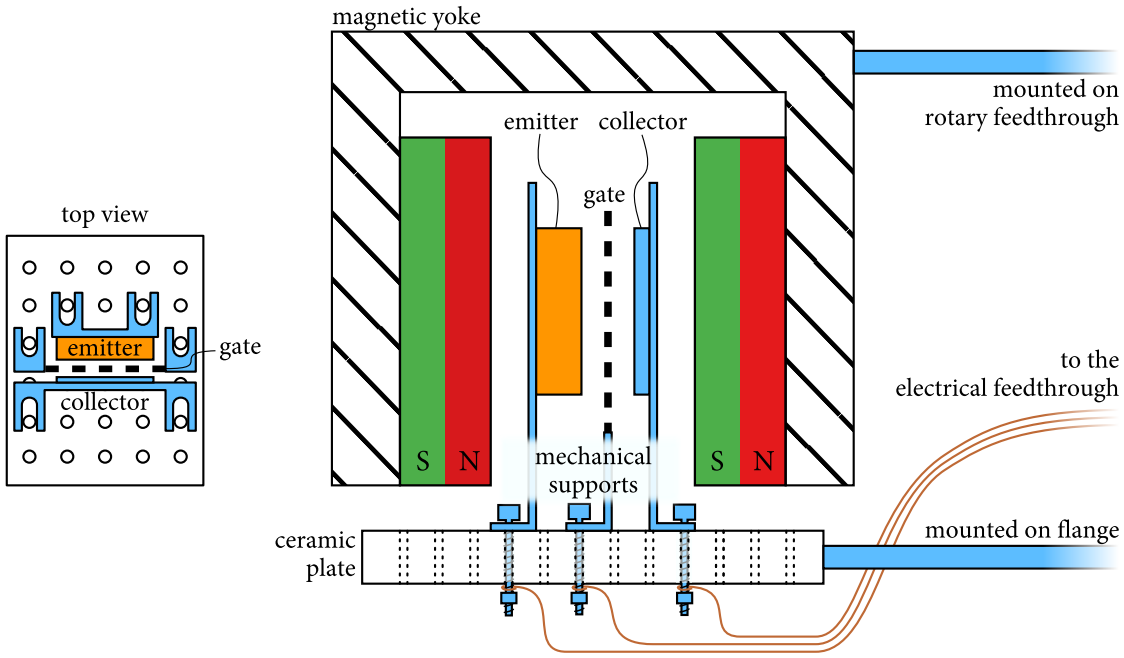

Figure 4.3: Sketch of the main experiment inside the vacuum chamber. The permanent magnets are attached to an iron yoke, which itself is mounted on a rotary feedthrough incorporated into the main flange. This way the magnetic field can be switched on and off *in situ*. Emitter, gate, and collector are mounted on a perforated ceramic plate, which allows for variable positioning and guarantees good electrical insulation. The ceramic plate is attached to the inside of the main flange.

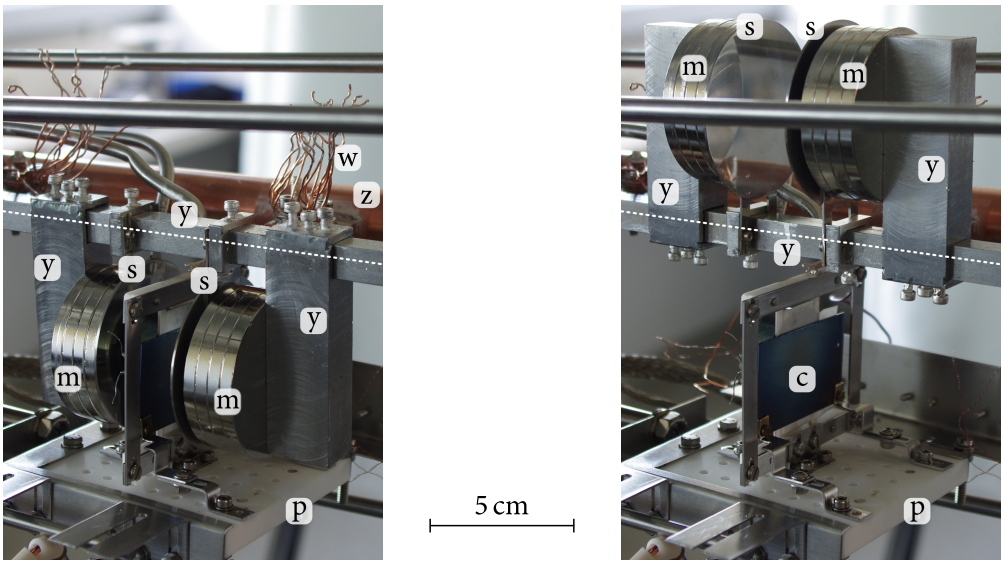

(a) **(b)**

Figure 4.4: Photographs of the main experiment with the magnets in position for measurements with **(a)** and without **(b)** magnetic field. The magnets are protected from the thermal radiation from the emitter by heat shields (s). The axis of rotation of the rotary feedthrough is indicated as a dashed line. Further visible components: the ceramic plate (p) holding emitter, gate, and collector (c), and a copper cylinder (z) and some copper wires (w), which are used to cool the magnets in some experiments.

The wiring of the experiment is sketched in Fig. 4.5. Four-wire-sensing carried out by standard source-measurement-units (SMUs) was used to precisely control the electric potentials at the emitter, gate, and collector. The collector-load-circuit is not realized by a variable resistor, but by an SMU as well. This enables to measure not only in the regime of positive load voltages, but also in in the so-called accelerating regime, where electrons are accelerated towards the collector. By definition of the load voltage (see *e.g.* Fig. 3.5), this corresponds to negative load voltages, which cannot be realized with a resistor. Additionally, using a computer-controlled SMU has the advantage to permit automatic measurements. That the SMU behaves exactly like the equivalent collector-load-cycle sketched at the bottom of Fig. 4.5 was confirmed experimentally.

The resistively heated emitters to be discussed in the following section are heated by a standard power source, and the emitter temperature is measured with a standard pyrometer working in a spectral range of 1.45 µm to 1.80 µm. The spectral emissivity of the emitter was assumed to be 0.5. A custom software PID controller is used to automatically control the temperature. The gas inlets shown in Figs. 4.1 and 4.2 serve to blow nitrogen onto the emitter during maintenance. This is necessary because the emitter contains barium oxide, which is highly hygroscopic and consequently has to be protected from air moisture.

All instruments are connected to a computer to enable automatic measurements.

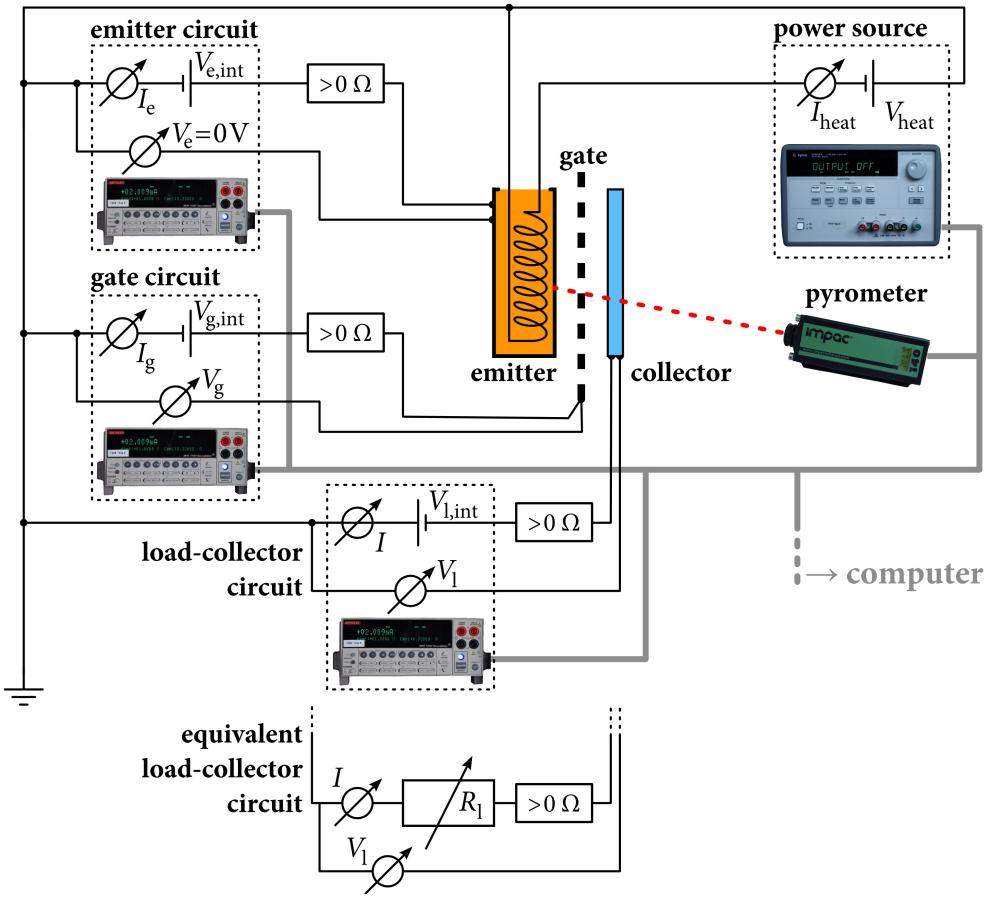

Figure 4.5: Sketch of the wiring of the experiment. The emitter is heated by a power source and its temperature is measured with a pyrometer. The heater wires are electrically insulated from the metallic hull of the emitter, and consequently from the emitting surface. This permits to measure the emitted current independently from the heating current. Due to the requirement to set the emitting surface to ground potential and the finite electrical conductance of the wire connecting it, it is necessary to actively set the potential difference between ground and emitting surface to zero. This is done with a source-measurement unit (SMU), which is programmed to measure I_e and to adjust $V_{e,int}$ such that $V_e = 0\,V$.
Similarly, to precisely adjust the electric potential at the gate, an SMU is programmed to measure I_g and to adjust $V_{g,int}$ such that V_g matches the desired value.
To enable automatic measurements, the load is not realized by a variable resistor, but by an SMU. Again, it is programmed to measure I_l and to adjust $V_{l,int}$ such that V_l matches the desired value. As was confirmed experimentally, this is equivalent to incorporating a variable resistor R_l and measuring I_l and V_l with an ampere- and voltmeter, respectively.

4.2 Emitters

First experiments were performed with directly heated, wound tungsten filaments as shown in Fig. 4.6a. This setup had a couple of drawbacks, the most important one being a significant voltage drop across the filament due to its resistive heating. As tungsten has a work function of about 4.5 eV [86], a voltage of typically 10 V had to be applied to heat the filament to sufficiently high temperatures. The resulting potential drop creates an electrostatic field along the filament, which significantly disturbs the movement of emitted electrons. The same holds true for any directly, resistively heated emitter material, albeit it can be slightly less serious with low-work-function materials.

Additional drawbacks of wound filaments are the typically small emitting surface, leading to small emission currents even at high temperatures, and the non-flat geometry, making it difficult to perform distance-dependent measurements.

To avoid these issues, an indirectly heated emitter was used, where the flat, emitting surface has a low-work-function and is thermally – but not electrically – connected to the resistive heating element. An emitter work function ϕ_e ranging from 2 eV to 3 eV makes it possible to attain current densities in the order of 1 A/cm^2 at moderately high temperatures of about 1000 °C to 1500 °C (see Eq. 3.2 and Fig. 3.3b).

A couple of material systems were considered, such as LaB_6 (work function 2.8 eV [86]), tungsten doped with intermetallic oxides [96, 97] and barium-oxide-dispenser cathodes. The latter were actually used as they have very promising specifications and are commercially available in suitable geometries. Figure 4.6b shows an off-the-shelve configuration [98] used for preliminary experiments, while Figs. 4.6c and 4.6d show a custom cathode, which was manufactured on request [98] to be very compact in z-direction. This custom design was used in all experiments shown within this thesis.

BaO-dispenser cathodes consist of a porous tungsten matrix that is interspersed with barium oxide, the emitting material. An aluminum oxide filling thermally connects the heating wire with the tungsten matrix and at the same time electrically insulates both [99]. Figure 4.7a shows a sketch of this configuration for the custom BaO-dispenser cathode used in this thesis.

When the cathode is heated, BaO diffuses from within the reservoir formed by the pores in the tungsten matrix to the outside and constitutes a low-work-function surface on top of the outermost tungsten layer [99, 100]. Figures 4.7b and 4.7c sketch the most probable configuration of this emitting surface for an examplary BaO coverage of 25 % [101].

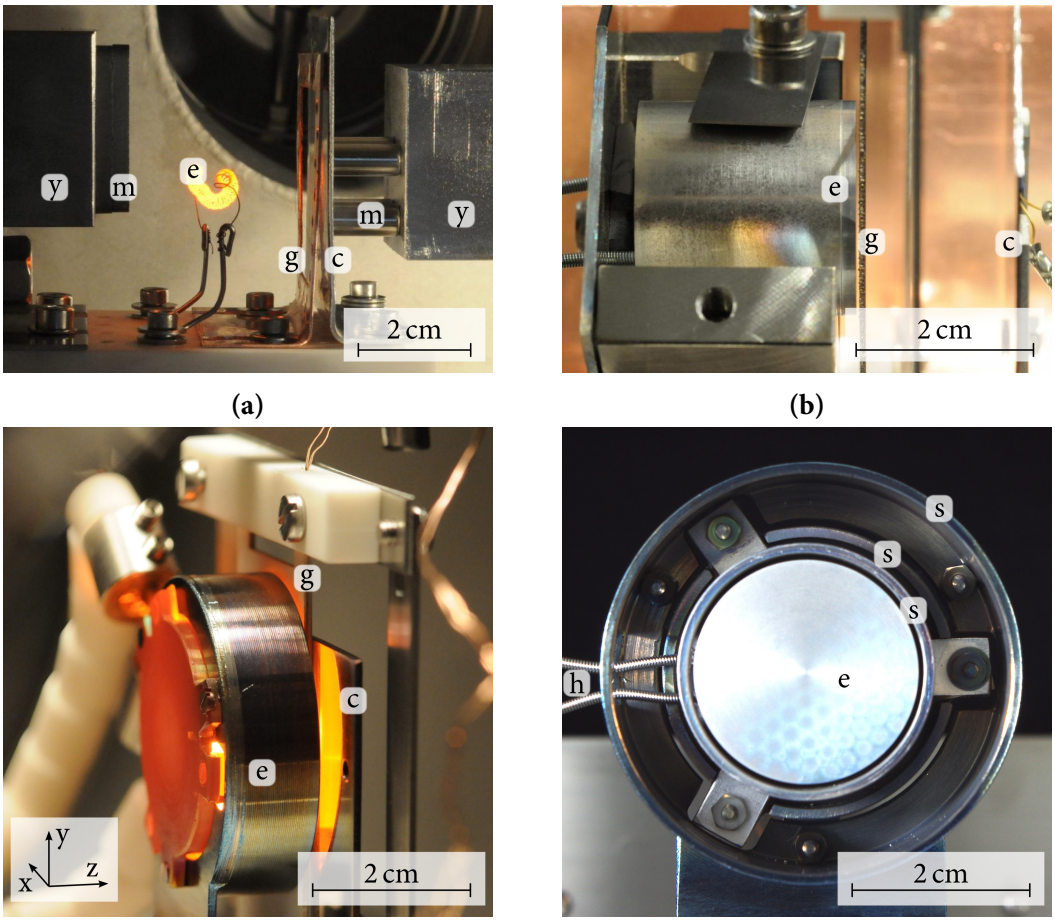

Figure 4.6: Photographs of emitters used within this work. **(a)** First experiments were performed with resistively heated tungsten filaments (e). The gate (g) was formed of tungsten wires strained on a copper or ceramic frame. Some permanent magnets (m) mounted on a magnetic yoke (y) generated the magnetic field. The major drawback of this setup was a potential drop across the filament, caused by the direct, resistive heating. **(b)** The BaO-dispenser cathode (e) used for preliminary experiments has an indirectly heated and flat, emitting surface, avoiding any potential drop across the surface and making it possible to mount the gate (g) in a well-defined distance. Emitting area: $A = 2.85\,\mathrm{cm}^2$. **(c)** The custom BaO-dispenser cathode makes it possible to mount the magnets (not shown here) very close to the experimental stack consisting of emitter (e, within heat shields), gate (g, in between distance plates), and collector (c). Emitting area: $A = 2.85\,\mathrm{cm}^2$. **(d)** Front view of the custom BaO-dispenser cathode (e) within three layers of heat shields (s). On the left side the heater wires (h) can be seen. After many days of operation the emitting surface shows hexagonal imprints probably originating from the gate. No influence of those imprints on the emission behavior could be observed.
Photographs by K. Wiedenmann (**a**, **b**), A. Herrnberger (**c**).

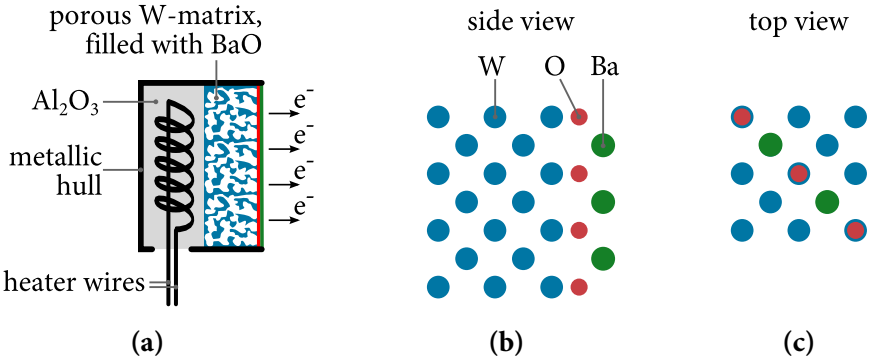

Figure 4.7: Working principle of BaO-dispenser cathodes. **(a)** Sketch of the resistively heated BaO-dispenser cathodes used during the work of this thesis. The aluminum-oxide filling transmits heat from the heater wires to the tungsten matrix, where an emissive surface is formed. **(b)** and **(c)** The emissive surface consists of usually partial monolayers of barium and oxygen on top of the tungsten surface. The configuration sketched here is the most probable one for a typical barium-oxide coverage of 25 % [101].

The emission properties of the BaO-dispenser cathodes were studied using a simplified version of the generator setup, where the gate was omitted. Instead – as sketched in Fig. 3.2a – an accelerating voltage V_{acc} was directly applied to a collector made of steel, which was mounted in a distance d_{ec} from the emitter.

When BaO-dispenser cathodes are heated, it typically takes several hours until a sufficient amount of barium has diffused to the surface and established the low-work-function layer. In the literature this effect is called activation [99, 102, 103]. It can be observed by repeatedly taking $I_{\mathrm{l}}(V_{\mathrm{acc}})$ characteristics, as shown in Fig. 4.8a. These characteristics were recorded directly after the emitter temperature was increased from 800 °C to 850 °C and clearly demonstrate an increase of the emission capability as a function of time. They show the expected diode behavior with clear Child-Langmuir and Richardson-Dushman regimes (see Fig. 3.2b). The Richardson-Dushman saturation current I_{RD} is indicated in this figure for one characteristic.

From every $I_{\mathrm{l}}(V_{\mathrm{acc}})$ characteristic the respective emitter work function ϕ_{e} can be determined from the corresponding saturation current I_{RD} by solving the Richardson-Dushman equation (Eq. 3.2) for ϕ_{e}:

$$\phi_{\mathrm{e}} = -k_{\mathrm{B}} T_{\mathrm{e}} \ln \frac{I_{\mathrm{RD}}/A}{A_{\mathrm{R}} T_{\mathrm{e}}^2}, \tag{4.1}$$

where A is the emitting area.

Figure 4.8b shows the emitter work function ϕ_e, calculated from the saturation current using Eq. 4.1, as a function of T_e. The barium diffusion to and the evaporation from the emitter surface as well as the kinetics of the chemical reactions leading to the formation of the low-work-function surface are temperature dependent processes. Consequently, the temperature and time dependence of the work function does not surprise.

BaO-dispenser cathodes are very sensible against practically any kind of contamination as the low-work-function surface is easily disturbed by impurities, leading to higher work functions and thus lower emission currents. This effect is called poisoning and appears with common gases like CO_2 and O_2, as well as water vapor [103]. Hence, the BaO-dispenser cathodes have to be operated at pressures below 1×10^{-6} mbar [104]. To avoid contaminations and because barium oxide is very hygroscopic, the BaO-dispenser cathodes used during the work of this thesis were kept in a nitrogen flow during maintenance periods.

Additionally, poisoning occurs with most metals, if their vapor pressure is too high [105]. Hence, the need to avoid poisoning sets some material constraints on other parts of the experimental setup, especially on the gate.

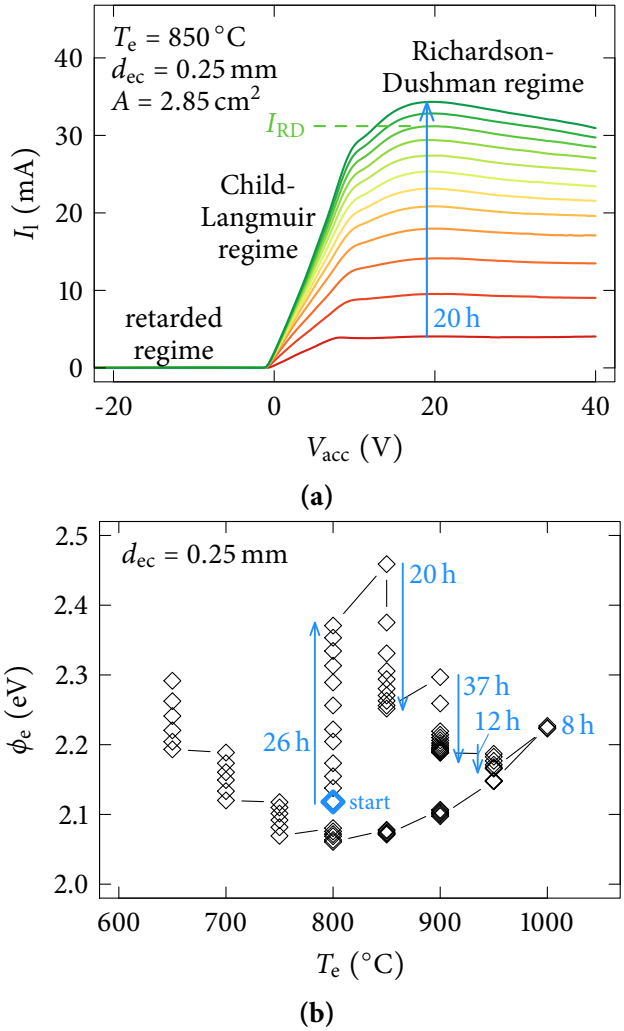

Figure 4.8: Time and temperature dependent measurements of the emitter's emission capability. **(a)** $I(V_{acc})$ characteristics taken during the activation of the emitter. A small ohmic background conductance of about 1 mA per 20 V was subtracted. Due to the slow diffusion of barium to the surface and the slow kinetics of the surface chemistry, it takes several hours for the emission capability to saturate. From the Richardson-Dushman saturation current I_{RD}, which is indicated for one exemplary characteristic, the work function of the emitter can be determined based on Eq. 4.1.
(b) The emission capability of the emitter was investigated as a function of time and temperature. After an initial activation phase at T_e = 950 °C (not shown) the temperature was set to the starting point at 800 °C. As this temperature is too low to sustain the low-work-function surface, the work function slowly increases. At higher temperatures the emitter is re-activated and the work function decreases again. For T_e > 1000 °C the work function can not be determined as in this case the saturation current exceeds the measurement limit of 1 A. After the work function had saturated at T_e = 1000 °C the temperature was decreased in steps of 50 °C and the emission behavior was measured for 2 h per step. A steel collector was used for this measurement.

4.3 Gates

The gate obviously needs to be an electrical conductor, and mechanically stable up to high temperatures as it is mounted near the hot emitter. Additionally, to avoid the poisoning of the emitter, its vapor pressure needs to be sufficiently low at those temperatures. Both requirements are best fulfilled by refractory metals. Of these, tungsten has the lowest electrical resistivity ($5.3 \times 10^{-8}\,\Omega\,\mathrm{m}$ [106, p. 12/41]) and, additionally, a very low vapor pressure at high temperatures [106, p. 4/125].

Some preliminary experiments were performed with a gate made of tungsten wires, which were strained on a ceramic frame. Such gates were found to have major drawbacks concerning their planarity and the geometry of the generated electric field.

To avoid those drawbacks, gates were structured by laser cutting tungsten foils by external vendors [107, 108]. It was found possible to create grid bars as thin as 80 µm with this technique, if the foil is not thicker than about 250 µm (see Fig. 4.9c). In contrast to strained wires, this technique also allows the design of complex structures like the honeycomb lattices shown in Fig. 4.9. Due to its optimum plane filling [109], this structure was used in all experiments shown within this thesis.

As will be discussed in detail in Ch. 6, the performance of these gates – *i.e.* their ability to suppress the space charge – was found to highly depend on the mesh diameter w, which I define as is shown in Fig. 4.9a. A further important parameter is the transparency t, defined as sketched in Fig. 4.9b as the fraction of the mesh area and the total cross section of the gate.

To mount emitter, gate, and collector with stable spacings therebetween, the gate is sandwiched in between aluminum oxide spacers, which were likewise fabricated by an external vendor via laser cutting [107]. For this purpose, aluminum oxide was selected because of its very high electrical resistivity (of order $10 \times 10^{12}\,\Omega\,\mathrm{m}$ [110]) and because it is already contained in the BaO-dispenser cathodes, reducing the probability of poisoning the latter. Figure 4.9d shows a photograph of the gate and one spacer during mounting into the metal frame holding them in position. After this step, emitter and collector are slightly pressed against the spacers on their respective sides to obtain a robust assembly.

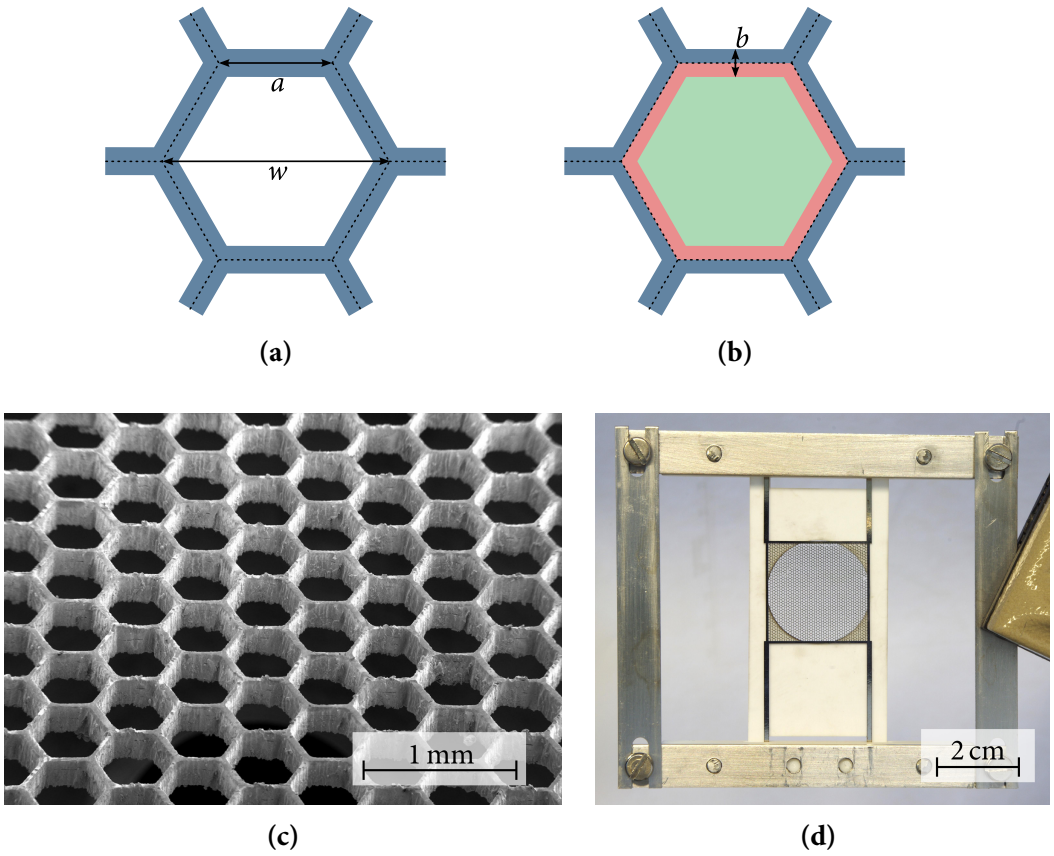

Figure 4.9: The gates used in this thesis. **(a)** The mesh diameter $w = 2a$ is defined as the distance of opposite corners of the hexagons. **(b)** For fixed w the bar width b controls the transparency t of the gate, which is defined as the fraction of the mesh area and the total cross section of the gate. Taking advantage of the periodicity this can be written as $t = A_{\text{green}}/(A_{\text{green}} + A_{\text{red}})$. **(c)** Scanning electron micrograph of a gate with $w = 0.6\,\text{mm}$, $b = 0.08\,\text{mm}$, and a thickness of $0.2\,\text{mm}$. Micrograph taken by B. Fenk (Max-Planck Institute for Solid State Research, Stuttgart). **(d)** The gates are sandwiched in between Al_2O_3 distance plates and mounted within a metal frame. A second distance plate is not shown here.

4.4 Collectors

As was demonstrated in chapter 3.2, the collector work function ϕ_c has to be smaller than the emitter work function ϕ_e to achieve a high energy conversion efficiency. This can be realized by using either a low ϕ_c and an intermediate ϕ_e, or an intermediate ϕ_c and a high ϕ_e. Both approaches were found to be difficult to follow as low-work-function surfaces are difficult to achieve, and high-work-function emitters have to be heated to very high temperatures to emit sufficiently large current densities.

However, to study the suppression of the space charge by electric and magnetic fields, it is not necessary to use collectors with work functions as low as that. Instead, for this purpose any work function can be simulated electrically by applying an offset voltage. As can be seen in Fig. 4.10, the electric field working on the electrons on their way to the collector in this case is identical to the one that would be present if a low-work-function collector was used.

Consequently, it was decided not to optimize the system with respect to conversion efficiency, and to work with conventional collector materials instead. Most measurements were performed using collectors fabricated of stainless steel. This is due to the relatively low outgassing of stainless steel even at elevated temperatures, which reduces the danger of poisoning the emitter, and the good machinability as compared to refractory metals.

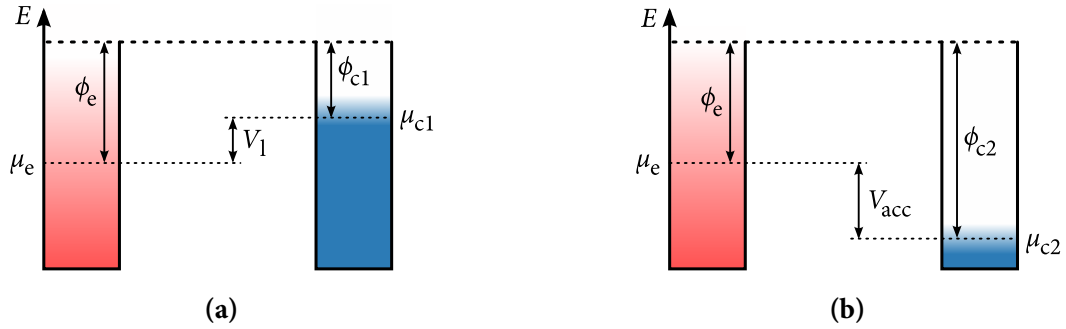

Figure 4.10: The electrical simulation of a low collector work function. The electric field in the interelectrode space (here: $E = 0$) is identical in the two cases of a low collector work function ϕ_{c1} with an applied load voltage $V_l > 0$ (**a**) and a high collector work function ϕ_{c2} with an applied accelerating voltage $V_{acc} < 0$ (**b**), where $V_{acc} = V_l + \phi_{c1}/e - \phi_{c2}/e$. A practical TIC as in (**a**) can therefore be studied experimentally by using high-work-function collectors as in (**b**). Unless explicitly stated otherwise, this electrical simulation of low collector work functions is not applied on data shown in this thesis.

To perform measurements with $\phi_c \approx \phi_e$, which has the advantage of a vanishing contact potential (see Ch. 3.2), in some cases a second BaO-dispenser cathode was used as a

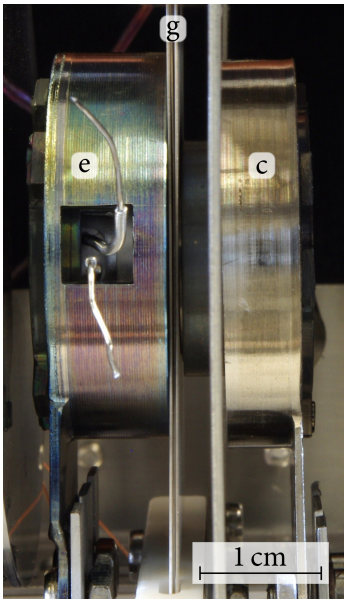

Figure 4.11: Photograph of the setup using an additional BaO-dispenser cathode as collector (c, in between heat shields). To enable the mounting of emitter (e, in between heat shields), gate (g), and collector, the outermost heat shield on the right-hand side is shorter than the one on the left-hand side. This setup was used to study the behavior of the system with vanishing contact potential.

collector. As in these type of measurements the collector can be heated to temperatures high enough to permit a small but well detectable back-emission, ϕ_c can be estimated therefrom using the Richardson-Dushman equation (Eq. 4.1). Figure 4.11 shows a photograph of this setup.

5 Proof-of-concept of thermoelectronic energy conversion

A significant part of this work was dedicated to understanding and demonstrating the fundamental physics governing the transfer of electrons across the vacuum gap of a thermoelectronic converter. Therefore, within this part the focus was on experimentally testing the influence of the electric and magnetic fields on the electron movement from the emitter to the collector. It was not intended to optimize the conversion efficiency or the output power density.

The most important tool to investigate the electron movement was the measurement of IV characteristics for various device configurations. Thereby both the influence of the load and gate voltages on the collector and gate currents were investigated. All data shown in this chapter were measured with a gate having a mesh diameter of w = 1.6 mm, a bar width of b = 80 µm and a thickness of 0.2 mm. The influence of the gate geometry will be discussed in Ch. 6. Unless stated otherwise a magnetic field of order 200 mT was applied.

5.1 Basic current-voltage characteristics

In a practical TEC, the load resistance is varied to adjust the load voltage V_l to its optimum value $V_\mathrm{mp} = (\phi_\mathrm{e} - \phi_\mathrm{c})/e$ and thereby maximize the output power. As has been described in the preceding chapter, in my experiments the variation of the load resistance was realized by directly applying the load voltage V_l between emitter and collector and measuring the resulting collector current with a standard SMU.

Figure 5.1 shows a typical $I_\mathrm{l}(V_\mathrm{l})$ characteristic, which was obtained with two BaO-dispenser cathodes working as emitter and collector. Before recording this $I_\mathrm{l}(V_\mathrm{l})$ characteristic, the work functions of emitter and collector were adjusted such that $\phi_\mathrm{c} < \phi_\mathrm{e}$ by taking advantage of the temperature and time dependence of the work functions of the BaO-dispenser cathodes (see Ch. 4.2).

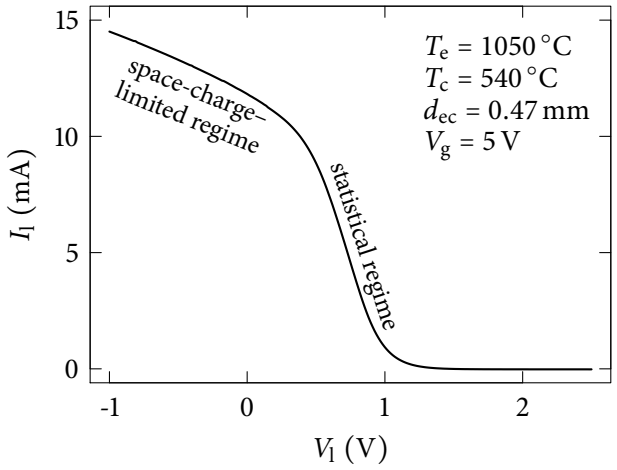

Figure 5.1: Typical characteristic of the output current I_l as a function of the load voltage V_l. For high load voltages, the collector current becomes small as hardly any electron evaporated from the emitter has sufficient kinetic energy to reach the collector. With decreasing load voltage more electrons can reach the collector and I_l increases until it enters the space-charge-limited regime at $V_l \approx 0.2\,\mathrm{V}$. Collector: BaO-dispenser, gate: see p. 61.

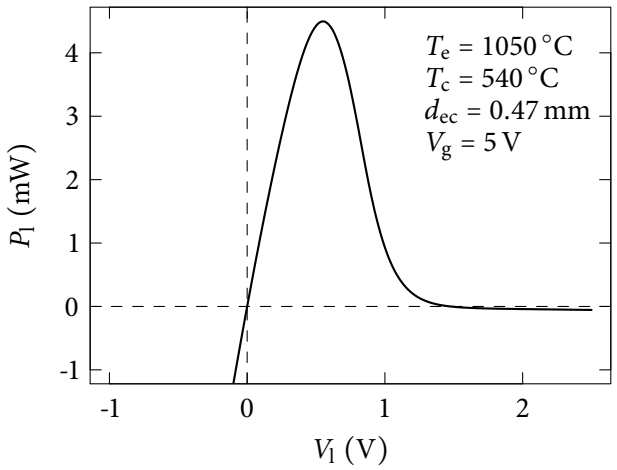

Figure 5.2: Electric power generation while measuring the $I_l(V_l)$ characteristic shown in Fig. 5.1. The system generates an electric output power for $0 < V_l \lesssim 1.2\,\mathrm{V}$, whereas it consumes electric power when negative load voltages are applied or when the back emission leads to negative collector currents. Collector: BaO-dispenser, gate: see p. 61.

At high load voltages, only a small fraction of the emitted electrons has sufficient kinetic energy to overcome the resulting, retarding electric field (see Fig. 3.5d). As expected, the output current I_l approaches zero in this case. With decreasing load voltage, slower electrons can reach the collector and the respective current increases until at $V_l \approx 0.2\,\mathrm{V}$ finally every emitted electron has sufficient kinetic energy to reach the collector. As the current in this regime is mainly determined by the velocity distribution of the emitted electrons, this regime is called the statistical regime.

As negative load voltages correspond to an acceleration of electrons onto the collector, within this accelerating regime every electron that is not reflected by the space charge is expected to reach the collector. For an idealized TEC, in which no space charge is present, one would then expect the slope to be zero, as sketched in Fig. 3.6. A finite slope being observed in the experiment therefore indicates that the gate electric field does not completely suppress the space charge. With increasing accelerating collector potential the residual space charge is then suppressed and the output current therefore still increases slightly. Consequently, this small-slope regime of the $I_l(V_l)$ characteristic is referred to as the space-charge-limited regime.

As Fig. 5.2 illustrates, the system generates an electric output power $P_l = I_l V_l$ with the maximum of 4.5 mW being reached at a load voltage of 0.55 V. As expected, in the accelerating regime and for $V_l \gtrsim 1.2\,\mathrm{V}$, where due to the back-emission I_l becomes negative, the system consumes electric power.

Notably, the $I_l(V_l)$ and $P_l(V_l)$ characteristics for fixed gate voltages shown in Fig. 5.1 and 5.2 correspond very well to what has been reported in the literature for other types of TICs (see *e.g.* the standard work by Hatsopoulos [21, 22]).

Determination of the collector work function and V_{mp} from $I_l(V_l)$ characteristics

As was pointed out in Ch. 3.2, the collector work function plays a fundamental role in any TIC. Efficient energy conversion is not possible without low collector work functions. However, to avoid the experimental complexity of obtaining and maintaining low-work-function surfaces, we decided to use available materials with work functions that – although being impractical for efficient energy conversion – are adequate to study the transfer of electrons across the vacuum gap. Nevertheless, knowing the actual collector work function is of high interest to interpret the experimental data.

As was already noted in Ch. 4, both polished steel plates and BaO-dispenser cathodes were used as collectors. Reported work functions of steel vary from around 4.3 eV [111] to

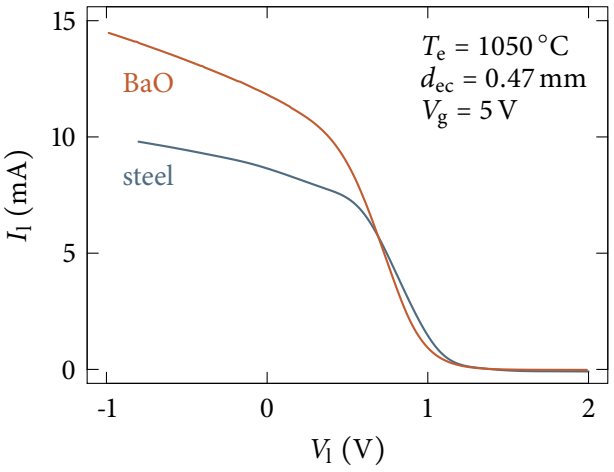

Figure 5.3: Comparison of two typical $I_l(V_l)$ curves measured with a steel ($T_c \approx$ 500 °C) and a BaO-type (T_c = 540 °C) collector. The transition from the statistical to the space-charge-limited regime occurs at approximately the same load voltage. This strongly suggests that the steel collector has a work function that is very similar to the one of the BaO collector. The offset of about 5 mA at negative load voltages may be due to different gate work functions, which lead to different accelerating E-fields. Gate: see p. 61.

around 5.6 eV [112], mainly depending on the method of measurement and the oxidation state of the surface. In contrast, the BaO-dispenser cathodes used as collectors in the experiments were prepared in order to have a work function ranging between 2.0 eV and 2.5 eV. Thinking of the ideal $I_l(V_l)$ characteristic shown in Fig. 3.6, one would therefore expect to observe an offset of the load voltage of about 2 V in the $I_l(V_l)$ characteristics taken with both types of collectors.

However, much smaller – if any – offsets of V_l are observed, which can be seen from the comparison of two typical $I_l(V_l)$ curves shown in Fig. 5.3. As the work function of the BaO-type collector was controlled by measuring its emission capability, the small value of this offset is presumably due to the steel collectors having smaller work functions than expected. This can probably be explained by barium atoms being evaporated from the hot emitter [99] and condensing on the cold steel collector. To my knowledge, a reduction of the work function of steel by barium layers has not been reported in the literature, but it is well known both for cesium on steel [86, p. 125] and for barium on various metals [86, pp. 118-135]. This observation is therefore not surprising. Remarkably, this reduction of the collector work function offers the possibility to realize the state $\phi_c \lesssim \phi_e$ without using any uncommon materials on the collector side.

Assuming that the transfer of electrons to the collector does not alter their velocity distribution, the collector work function can be determined from a fit of the Richardson-Dushman equation (Eq. 3.3) to the measured $I_l(V_l)$ curves in the statistical regime. As noted in Ch. 3.2, this is due to the collector work function being the effective barrier electrons have to overcome to reach the collector. As Fig. 5.4 shows, from the $I_l(V_l)$ curve already shown in Figs. 5.1 and 5.3 this fit procedure yields ϕ_c = 2.1 eV.

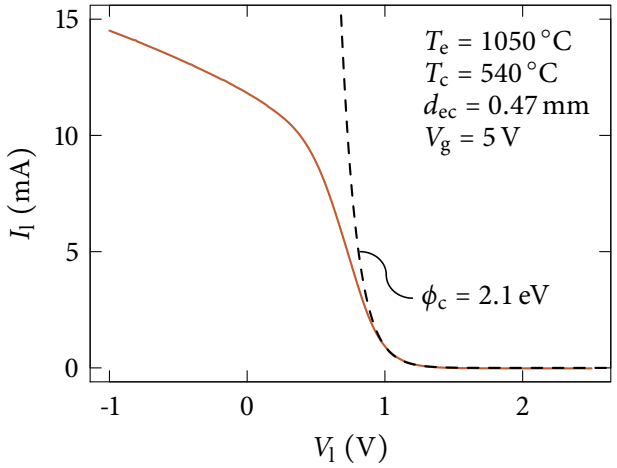

Figure 5.4: Measured $I_l(V_l)$ characteristic (solid line) and a corresponding Richardson-Dushman fit (dashed line, see Eq. 3.3). Unfortunately, the result of the fit strongly depends on the range it is applied to, which in this case is V_l = 0.9 V to V_l = 2.5 V. It yields a collector work function of ϕ_c = 2.1 eV. Collector: BaO-dispenser, gate: see p. 61.

Unfortunately, the values of the fit parameters were found to largely depend on the range the fits were applied to. For example, applying the fit shown in Fig. 5.4 to the range between V_l = 0.8 V and V_l = 2.5 V instead of V_l = 0.9 V and V_l = 2.5 V alters the resulting ϕ_c by nearly 0.1 eV. Additionally, the premise that the velocity distribution of the electrons is not altered during the transfer of electrons to the collector is questionable. There are various processes involved that might influence the electron velocity distribution, such as the exchange of momentum within the space-charge cloud or energy-dependent absorption and emission of electrons at the surfaces of collector and emitter, respectively. Hence, this approach to determine ϕ_c is known to be unreliable [113] and consequently not applied within this thesis.

Instead, it was found feasible to determine the difference of the work functions of emitter and collector rather than the collector work function itself. This can be done based on the transition between the statistical and the space-charge-limited regime. Since any practical TEC will be operated near $V_{mp} = (\phi_e - \phi_c)/e$, this parameter is indeed the relevant one. Within the statistical regime, which is determined by the $I_l(V_l)$ curve having a large slope, the vacuum level at the surface of the collector is larger than the one at the surface of the emitter. Hence, the number of electrons reaching the collector grows exponentially with decreasing load voltage. At $V_l = V_{mp} = (\phi_e - \phi_c)/e$ every emitted electron has enough kinetic energy to reach the collector, and the $I_l(V_l)$ curve therefore flattens out. Consequently, V_{mp} is expected to lie within the transition region between the statistical and the space-charge-limited regime. Although this transition is not sharp, V_{mp} is at least approximately determined by the intersection of two linear regressions to the $I_l(V_l)$ curve as shown in Fig 5.5. In this case, this method yields V_{mp} = 0.4 V. Throughout this work, the current I_l at $V_l = V_{mp}$ is denoted as I_{mp}.

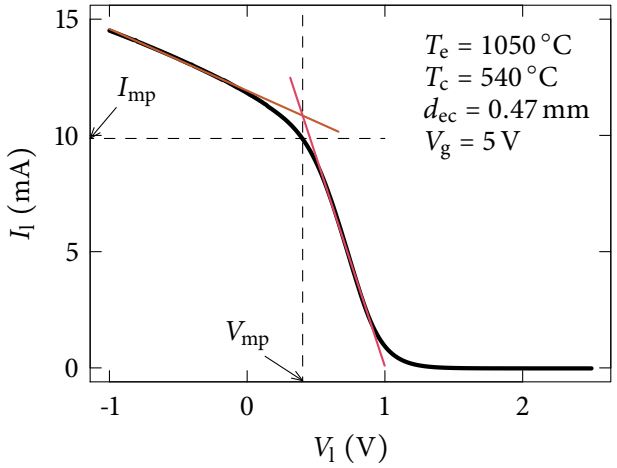

Figure 5.5: Measured $I_l(V_l)$ characteristic and linear regressions to the statistical and space-charge-limited regimes. The transition between both regimes occurs at $V_l = V_{mp} = (\phi_e - \phi_c)/e$. As this transition is not sharp, for this work V_{mp} and I_{mp} are defined by the intersection of two linear regressions in the respective ranges. Collector: BaO-dispenser, gate: see p. 61.

It should be noted that V_{mp}, as defined in Fig. 5.5, does not necessarily coincide with the maximum of the power generated in the experiment as it was shown in Fig. 5.2. In fact, V_{mp} will even be negative in case of $\phi_c > \phi_e$, and consequently in the experiment no power will be generated at $V_l = V_{mp}$.

5.2 Suppression of the space charge by the gate electric field

Figure 5.6 shows a typical series of $I_l(V_l)$ characteristics obtained with gate voltages ranging from 0 V to 24 V. The collector current I_l clearly increases with increasing gate voltage, showing that as expected the space charge is suppressed by the gate electric field.

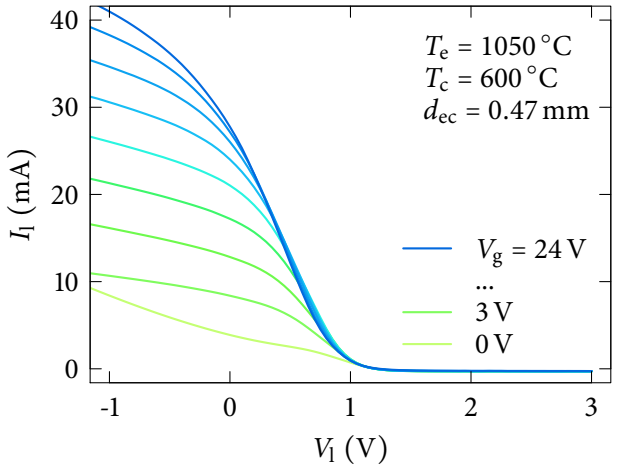

Figure 5.6: Collector current I_l as a function of the load voltage V_l for a series of gate voltages V_g ranging from 0 V to 24 V. The collector current clearly increases with increasing gate voltage, which strongly indicates that the space charge is suppressed by the gate electric field. Collector: BaO-dispenser, gate: see p. 61.

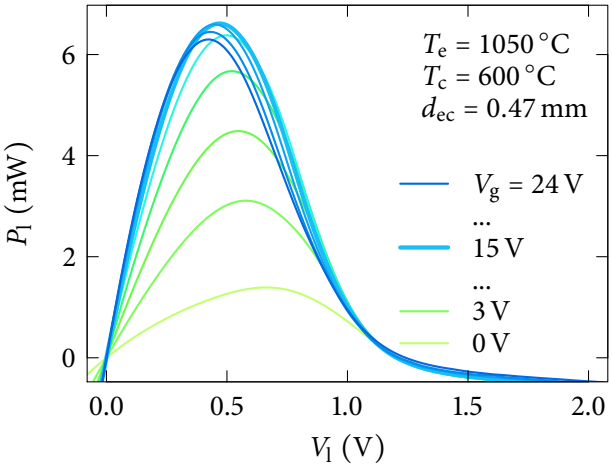

Figure 5.7: Generated power P_l as a function of the load voltage V_l for a series of gate voltages ranging from 0 V to 24 V. With increasing gate voltage, the load power first increases until it starts to decrease at gate voltages larger than the optimum gate voltage. The data for the optimum gate voltage (15 V) are drawn as a thick line. Collector: BaO-dispenser, gate: see p. 61.

The respective $P_l(V_l)$ characteristics are shown in Fig. 5.7. They, as well, clearly exhibit an increase of the generated power with increasing gate voltage. However, for gate voltages higher than the optimum gate voltage of 15 V the generated power starts to decrease. This arises from the slight decrease of I_{mp} for high gate voltages, which can be seen in Fig. 5.8a.

However, for $0\,V \leq V_g \lesssim 20\,V$, Fig. 5.8a clearly shows the suppression of the space charge by the gate electric field. Thereby, as the gate current does not saturate at high V_g, it may be concluded that the space charge is not fully suppressed. Consequently, the system operates in the Child-Langmuir regime (see Ch. 3.1), which can as well be seen in I_g following the Child-Langmuir law (Eq. 3.1). Thereby, the effective emitter-gate spacing, which occurs in the Child-Langmuir law, is larger than expected ($d_{eg,eff}$ = 0.6 mm > d_{eg} = 0.2 mm). Presumably, this is due to the 3-dimensionality of the system: the Child-Langmuir law actually accounts for 1D systems only.

For the case of negative – *i.e.* decelerating – gate voltages, this configuration is very similar to a conventional electron tube, where the gate voltage is typically used to suppress the collector current. In all measurements performed, both I_l and I_g rapidly approach zero for negative gate voltages. Consequently, data for $V_g < 0$ are not shown in this work.

To sum up, the measurements have shown that the electric field created by the gate actually suppresses the current-limiting effect of the space charge. However, the space charge cannot be completely suppressed. As will be discussed in Ch. 6, this is because in the configuration studied the emitter-collector spacing was unfavorably large.

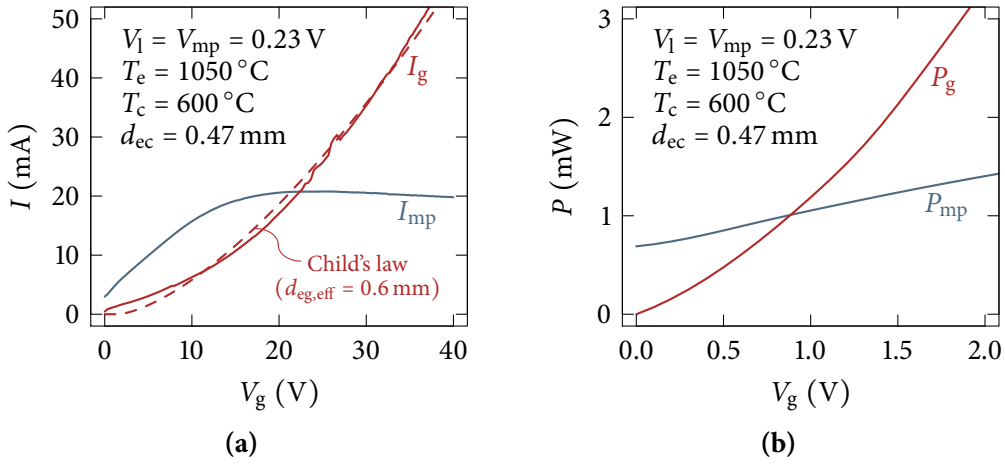

Figure 5.8: (a) Load and gate currents at $V_l = V_{mp}$ as a function of the gate voltage. For negative – *i.e.* decelerating – gate voltages, no current is observed (not shown here), while it arises with increasing gate voltage as the space charge is suppressed gradually. Unless very high gate voltages are applied, electrons preferably reach the collector. The space charge cannot be fully suppressed with the gate voltages applied in this measurement. Consequently, the gate current does not saturate. Instead, I_g follows a Child-Langmuir-like behavior (dashed line, see Ch. 3.1). **(b)** Generated power $P_{mp} = I_{mp} V_{mp}$ and gate power $P_g = I_g V_g$ as a function of gate voltage V_g. For small gate voltages the system generates more electric power than it consumes to sustain the gate electric field.
Collector: BaO-dispenser, gate: see p. 61.

5.3 Suppression of the gate current by the magnetic field

To explore the influence of the magnetic field on the transfer of electrons from the emitter to the collector, measurements with and without an applied magnetic field were performed. By rotating the magnetic yoke and the permanent magnets attached to it out of the experimental region, it is possible to switch the magnetic field on and off *in situ*, as already shown in Ch. 4.

Figures 5.9a and 5.9b show characteristics of the load and gate currents as a function of the load voltage with the magnetic field switched on and off, respectively. As expected, if there is no magnetic field applied, the gate current clearly exceeds the load current in the regime $V_\mathrm{l} \gtrsim V_\mathrm{mp}$. Only if an accelerating voltage (*i.e.* $V_\mathrm{l} < 0$) is applied to the collector, do the load and gate currents approach similar values. In contrast, with an applied magnetic field the load current dominates – in particular in the regime $V_\mathrm{l} \approx V_\mathrm{mp}$, which is relevant for practical devices.

This behavior is also clearly observable in Fig. 5.9c, where the share of the load current in the total emitted current is shown as a function of the load voltage. With an applied magnetic field, the load current nearly approaches the value expected from the geometry, which is the transparency $t = 0.89$ of the gate (see Fig. 4.9b).

Figures 5.10a and 5.10b show the collector and gate currents as a function of the gate voltage for $V_\mathrm{l} = V_\mathrm{mp}$. As can be seen, the effect of the magnetic field is stable over a broad range of gate voltages. The load current divided by the total current (Fig. 5.10c) is close to the geometrical transparency up to $V_\mathrm{g} = 15\,\mathrm{V}$.

Because the gate current decreases significantly when the magnetic field is switched on, it can be concluded that the magnetic field forces electrons on paths along the magnetic field lines. Consequently, the majority of the electrons are effectively prevented from hitting the gate.

That the collector current divided by the total current is slightly lower than the gate transparency is presumably due to the inhomogeneous electric field. As can be seen in Fig. 5.11, the electric field on the surface of the emitter is nearly twice as large in regions aligned with the grid bars than in regions aligned with the meshes. This effect in combination with the not fully suppressed space charge leads to an increased current density in regions of the emitter facing the grid bars, as the space charge is suppressed to a higher degree there. Consequently, the share of the gate current in the total emitted current is higher than in the case of a homogeneous electric field or a fully suppressed space charge. Similarly, the share of the collector current in the total current is reduced.

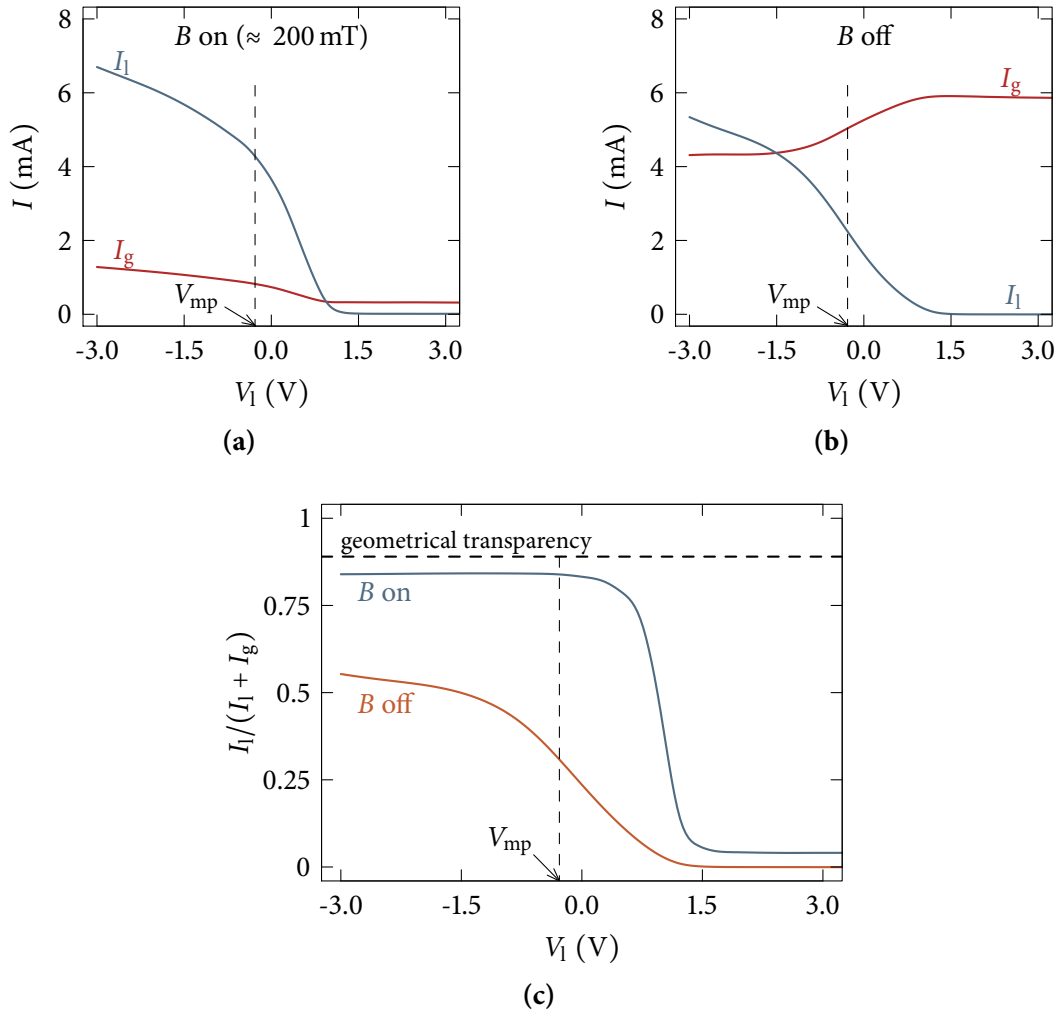

Figure 5.9: Load and gate currents as a function of load voltage for V_g = 6 V, T_e = 1100 °C, $T_c \approx 500$ °C, and d_{ec} = 1 mm with the magnetic field switched on (**a**) and off (**b**). With magnetic field applied the load current clearly dominates the gate current, in particular in the region $V_l \approx V_{mp}$, which is relevant for power generation. Without magnetic field, the gate current dominates for all relevant voltages. **(c)** Load current I_l divided by the total current $I_l + I_g$ plotted as a function of the load voltage. With applied magnetic field, $I_l/(I_l + I_g)$ nearly approaches the geometrical transparency t = 0.89 (see Fig. 4.9a) of the gate.
Collector: steel, gate: see p. 61.

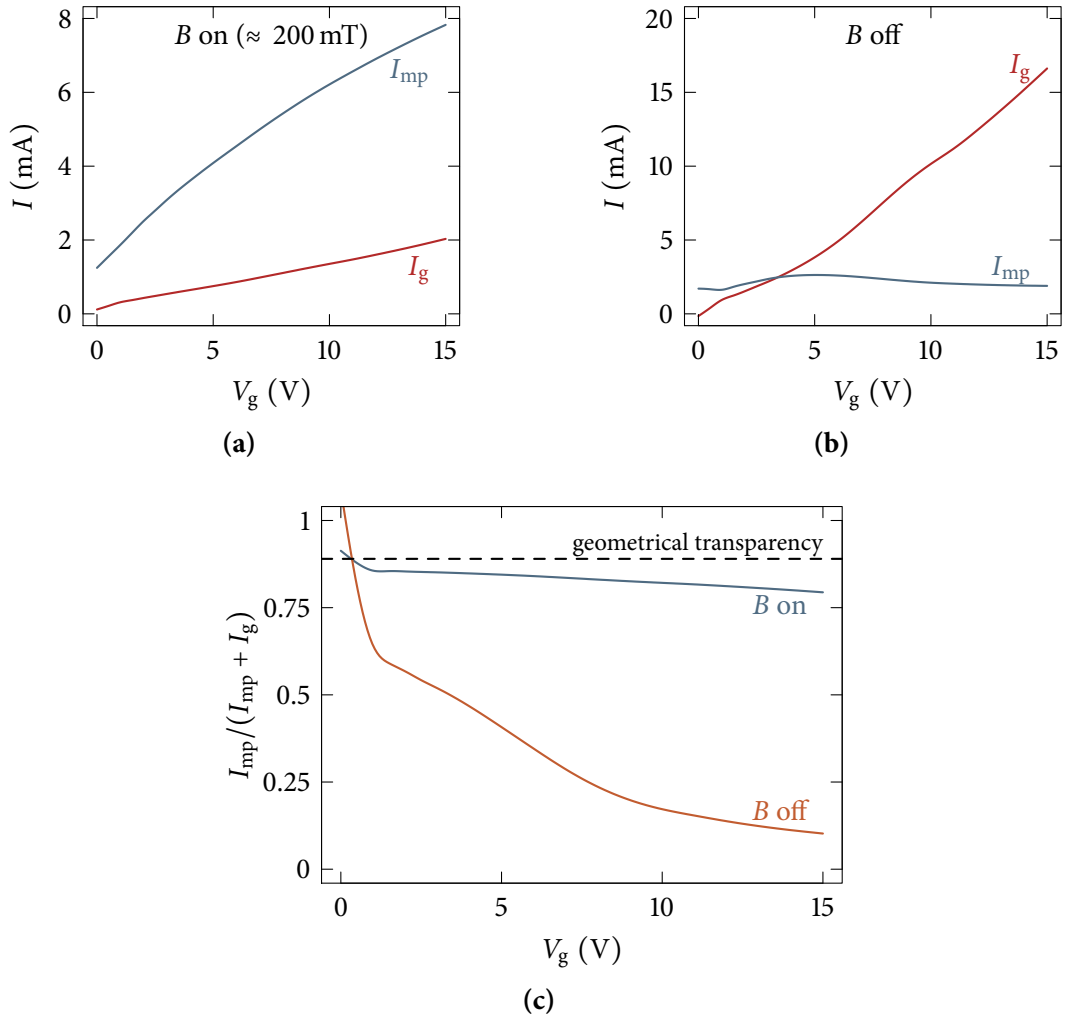

Figure 5.10: Load current and gate current as a function of gate voltage for $V_l = V_{mp} = -0.4\,\mathrm{V}$, $T_e = 1100\,°\mathrm{C}$, $T_c \approx 500\,°\mathrm{C}$, and $d_{ec} = 1\,\mathrm{mm}$ with the magnetic field switched on (**a**) and off (**b**). **(c)** Load current I_{mp} divided by the total current $(I_{mp} + I_g)$ plotted as a function of the gate voltage. With applied magnetic field $I_{mp}/(I_{mp} + I_g)$ is close to the geometrical transparency $t = 0.89$ of the gate up to $V_g = 15\,\mathrm{V}$. Collector: steel, gate: see p. 61.

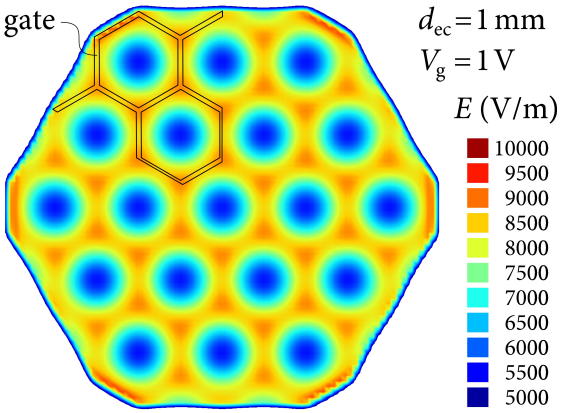

Figure 5.11: Calculated magnitude of the electric field on a plane in a distance of 5 µm from the emitter for the measurements shown in Figs. 5.9 and 5.10. The electric field in regions facing the bars of the grid is nearly a factor of 2 larger than in regions facing the meshes. This leads to a high current density near the bars as compared to the meshes. This calculation was performed with IES COULOMB [92].

5.4 Summary

In this chapter a proof-of-concept of the TEC working principle was given. It was demonstrated that the system presented in Ch. 4 generates more electric power than is necessary to maintain the electric field. Therefore, the system actually works as a converter of thermal to electric power. Measured IV characteristics correspond well to idealized models, but low achievable current densities and output powers still clearly show the influence of a not fully suppressed effect of the space charge.

The electric field generated by a positive voltage applied to the gate reduces the effects of the space charge and therefore increases the collector current. At the same time the magnetic field effectively prevents electrons from crashing onto the gate.

6 Assessment of attainable output powers and efficiencies

In the measurements shown in Ch. 5, only small powers were generated. They were in particular too small to build an efficient generator. Hence, in this chapter I want to give an analysis of the output powers and efficiencies that can be attained with TEC. This analysis will be based on a comparison of C. Stephanos' 1D models [19], the current tube model presented in Ch. 3.3, and my experimental results.

First I will discuss the role of the collector work function in the measurements.

6.1 Discussion of a hypothetical replacement of the collector by a low-work-function material

As has been discussed in Ch. 3.2, low collector work functions are crucial for an efficient and high-power operation of TICs. Therefore, with high-work-function collectors being used in the experiments, one cannot expect to attain high output powers. It is an interesting *Gedankenexperiment* to replace the actually used collector by a hypothetical one with a significantly lower work function.

As has already been touched in Ch. 4, a low-work-function collector can be simulated electrically by applying an offset voltage to the collector (see Fig. 4.10), which corresponds to a shift of the $I_l(V_l)$ curve along the voltage axis. Hence, upon replacing the collector actually used (work function ϕ_c) by a hypothetical one (work function $\phi'_c < \phi_c$), the $I_l(V_l)$ curve is shifted towards higher load voltages, as shown in Fig. 6.1a. Thereby, the generated power increases linearly with the work-function reduction (Fig. 6.1b). Similarly, the generated power as a function of the gate voltage increases linearly with the work-function reduction (Fig. 6.1c).

As can be seen, substituting the collector by one with a lower work function would increase the output power by a factor of two to four. However, this still does not push the system into the desired regime of some W/cm^2. Hence, there must be a further important

parameter that limits the output power in the experiments shown so far. As already noted and as will be discussed in detail in the following sections, this parameter is the gap width.

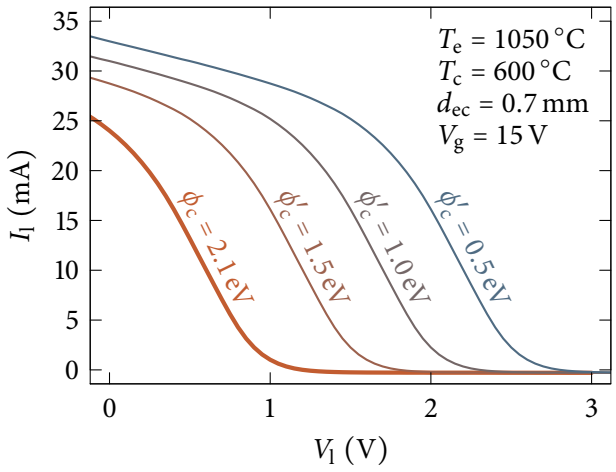

(a)

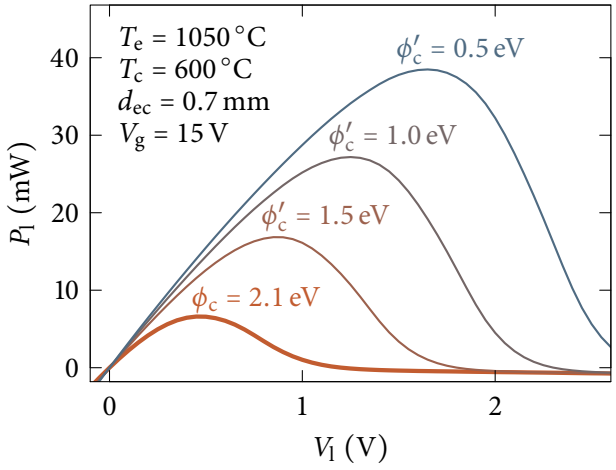

(b)

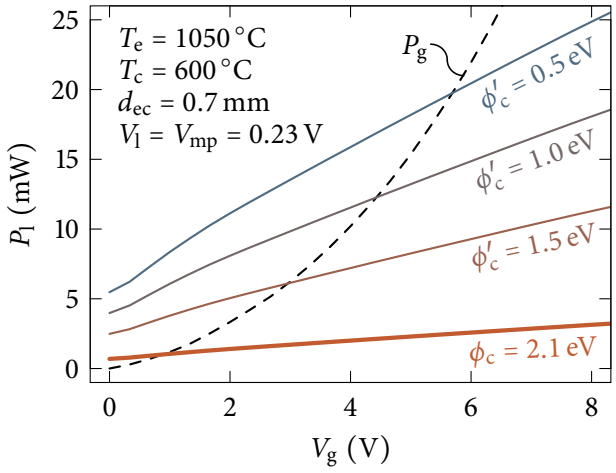

(c)

Figure 6.1: The influence of the collector work function on the power generation capability of the proof-of-concept TEC. **(a)** Replacing the collector used in the measurements ($\phi_c \approx 2.1$ eV, thick line) by a low-work-function collector (ϕ'_c, thin lines) shifts the $I_l(V_l)$ curve towards higher load voltages. Consequently, the generated power increases approximately linearly with the work-function difference $\phi_c - \phi'_c$. This effect is shown as a function of the load voltage and the gate voltage in (**b**) and (**c**), respectively. A BaO-type collector was used for the measurement at $\phi_c = 2.1$ eV. Gate: see p. 61.

6.2 Investigation of the scaling behavior of thermoelectronic energy converters

The one-dimensional models discussed in Ch. 3.3 indicate that far higher current densities should be attainable upon scaling the system to smaller emitter-collector spacings. This insight triggered the experimental investigation of the d_{ec}-dependence of the generator performance. As it is ideal to position the gate in the center between emitter and collector (see Ch. 3.3 and [19]), only setups fulfilling this boundary condition were studied. All measurements shown in this chapter were performed with gates having a bar width of 80 µm and a thickness of 0.2 mm.

To stabilize the emitter-gate and gate-collector spacings, the gate is sandwiched in between stacks of Al_2O_3 foils, which were structured by laser cutting (see Ch. 4). Different spacings can be obtained by varying the number and thickness of the foils of each stack. However, due to the mechanical mounting of the system and the requirement to avoid short circuits, it was not possible to use foils thinner than 0.13 mm. With the gate thickness of 0.2 mm this adds up to a minimum gap width of 0.47 mm.

I_{mp}, which is determined as shown in Fig. 5.5, is the most important property that was investigated for various d_{ec}. Figure 6.2 shows a typical set of $I_{mp}(V_g)$ characteristics for several emitter-collector-spacings and for two gate geometries. It clearly shows an increase of the slope of the $I_{mp}(V_g)$ characteristics with decreasing gap width d_{ec}, which – at least qualitatively – corresponds to the predictions of the models described in Ch. 3.3.

Furthermore, significantly higher currents are measured for $w = 0.6$ mm (Fig. 6.2b) than for $w = 1.6$ mm (Fig. 6.2a), even though the transparency for $w = 0.6$ mm ($t = 0.72$) is smaller than it is for $w = 1.6$ mm ($t = 0.89$). Presumably, differences in the magnitudes and geometries of the electric fields generated by both gate types account for this increase of the load current with decreasing mesh width. For decreasing $d_{ec} \lesssim w$, the electric field becomes unfavorably inhomogeneous, which causes it to saturate. For $d_{ec} \ll w$, the electric field even decreases in those regions of the emitter that are aligned with the gate meshes. Consequently, for the suppression of the space charge it is not helpful to decrease the gap width below a certain critical value. By calculating the electric field, it can be shown that these inhomogeneities start to develop at smaller gap widths if the mesh width is smaller. To demonstrate this effect, Fig. 6.3 shows a comparison of the electric fields generated by both gates. As can be seen, for an otherwise identical configuration the finer mesh creates a significantly larger and more homogeneous electric field. Consequently, smaller mesh diameters allow to suppress the space charge to a higher degree, which leads to the high load currents shown in Fig. 6.2b as compared to Fig. 6.2a.

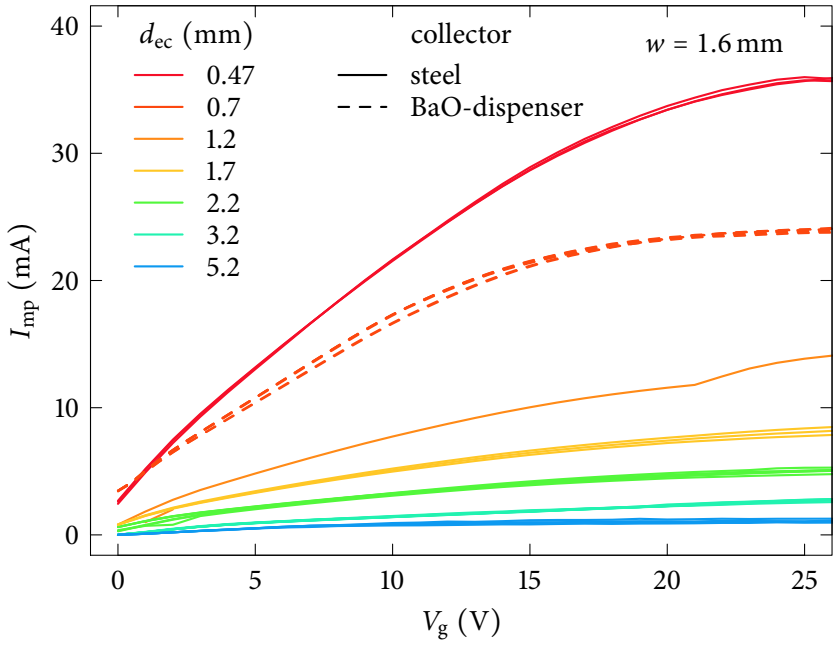

(a)

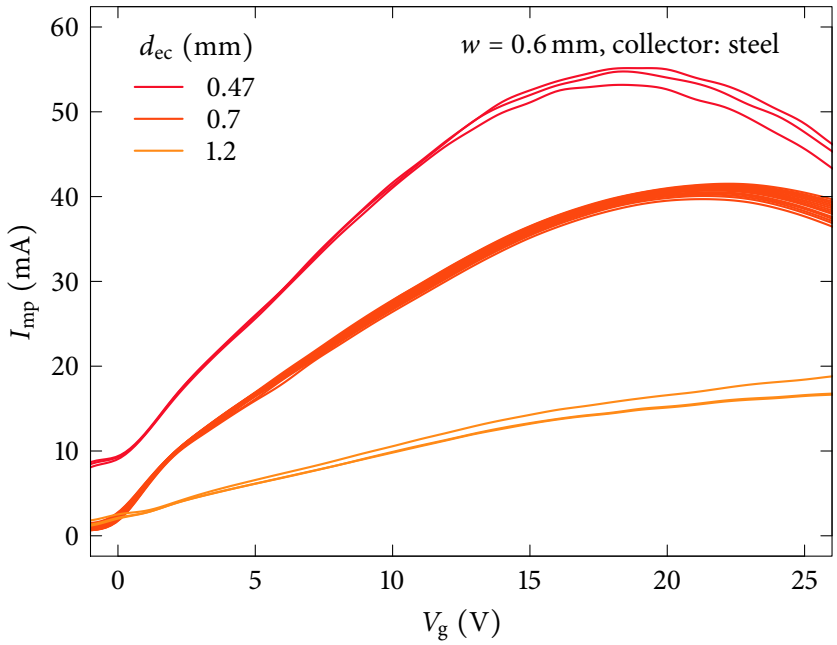

(b)

Figure 6.2: Collector current I_{mp} as a function of gate voltage V_g for a series of gap withs d_{ec}, T_e = 1000 °C, and $T_c \approx$ 500 °C. All data are for $V_l = V_{mp}$, which was determined separately for each curve as in Fig. 5.5. **(a)** and **(b)** show data for two different gates with the same thickness (0.2 mm) and bar width (b = 80 µm), but different mesh widths of w = 1.6 mm (top) and w = 0.6 mm (bottom), respectively. The slope of the $I_{mp}(V_g)$ curves clearly increases with decreasing gap and mesh width.

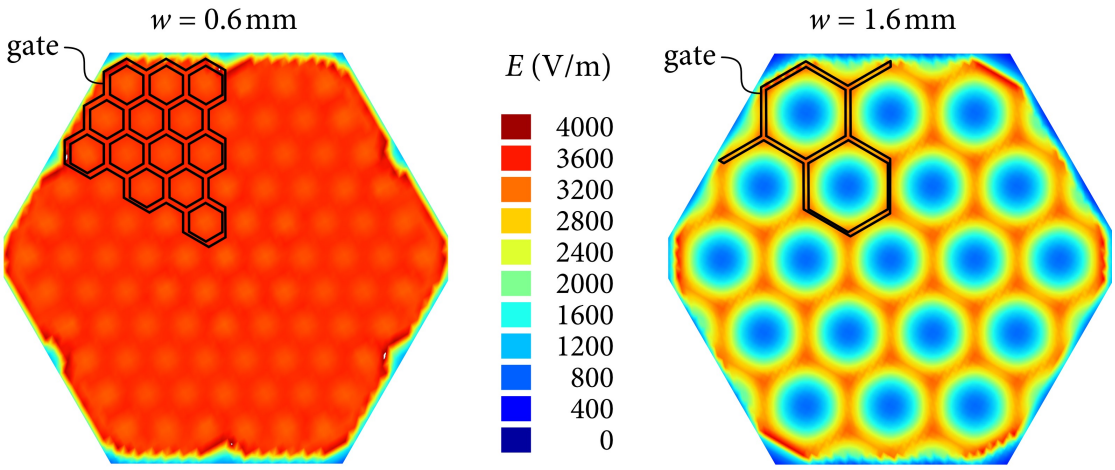

Figure 6.3: Calculated electric field generated by the two gates (left: $w = 0.6\,\mathrm{mm}$, right: $w = 1.6\,\mathrm{mm}$) that were used for the studies of the d_{ec}-dependence of the system performance. Here: $d_{ec} = 0.7\,\mathrm{mm}$, $V_g = 1\,\mathrm{V}$. The electric field scales linearly with V_g. This calculation was performed with IES COULOMB [92].

As can be seen, down to the smallest spacings and the highest gate voltages realized within this thesis still no collector current exceeding 60 mA, which corresponds to approximately 20 mA per cm^2 active emitter area, could be obtained. To assess attainable output currents and power densities it is therefore necessary to extrapolate the measurements shown in Fig. 6.2 to even smaller emitter-collector spacings. Below, this extrapolation will be carried out using the models introduced in Ch. 3.3.

Prior to that it is necessary to explore the validity of these models, which I will do in the following section.

Comparison of the 1D models and the measurements

The current tube model, which was introduced in Ch. 3.3 as a quasi-3-dimensional extension to C. Stephanos' 1D models [19], permits an estimation of the collector current density as a function of the gate voltage V_g. As Fig. 6.4 shows, it correctly predicts the order of magnitude of the collector current density, whereas it underestimates the current density at low V_g and overestimates it at high V_g.

The underestimation at low V_g is probably due to two simplifications. First, the non-zero velocity of the electrons upon emission is neglected. As discussed in Ch. 3.3, in the experiment some electrons have enough kinetic energy to overcome the space charge even if there is no gate voltage applied. Second, the 1D models are pure mean-field mod-

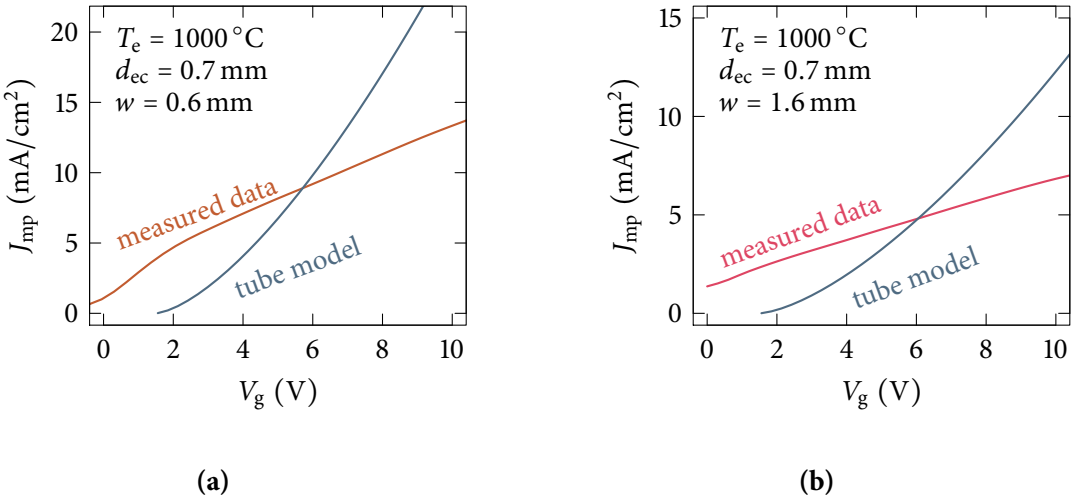

Figure 6.4: Load current density J_{mp} at $V_l = V_{mp}$ as a function of gate voltage V_g for the two gate types studied in this thesis. To compare both gates with each other, the load current is divided by the mesh area to obtain the current density. The current tube model correctly estimates the order of magnitude of J_{mp}; deviations at low and high V_g are discussed in the text. For the tube models the interelectrode space was divided in 300 tubes per gate mesh (see also Ch. 3.3). Collector: BaO (T_c = 600 °C) (**a**), steel ($T_c \approx$ 500 °C) (**b**).

els, *i.e.* direct electron-electron interactions are neglected. However, by exchange of momentum within the space-charge cloud such interactions can increase the number of electrons that reach the collector [19, 114, 115].

At high V_g the current density probably becomes highly inhomogeneous because, as the 1D model predicts, within each tube the current density increases more than linearly with the electric field. Consequently, interactions between electrons traveling through neighboring tubes can no longer be neglected and the current tube model fails.

However, at intermediate gate voltages around $V_g \approx 6$ V either all of the above-discussed effects are small or they compensate each other. The resulting agreement of current tube model and measurements at intermediate gate voltages of about 6 V was observed for all investigated gate geometries and gap widths.

This can be seen in Fig. 6.5, where the current density J_{mp} within the gate meshes is shown as a function of the gap width d_{ec}. As can be seen, for a given mesh diameter w and for decreasing d_{ec}, J_{mp} flattens out as compared to the behavior expected for in ideal gate. This flattening out occurs at smaller d_{ec} and higher J_{mp}, if the mesh diameter is smaller. Thereby the measured data very well correspond to the prediction of the current tube model.

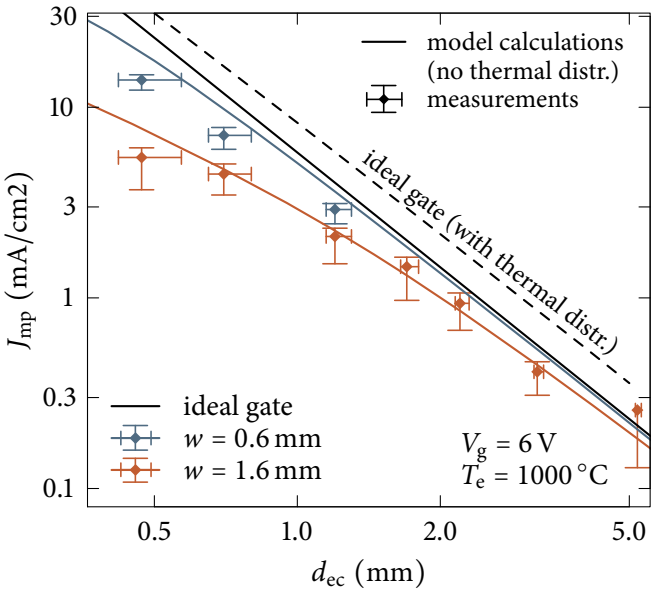

Figure 6.5: Load current density J_{mp} at $V_l = V_{mp}$ as a function of gap width d_{ec} for two different mesh widths. To compare both gates with each other, the load current is divided by the mesh area to obtain the current density. The colored lines are obtained using the current tube model described in Ch. 3.3. The solid black line was calculated from Eq. 3.19. The dashed black line was calculated numerically by C. Stephanos [19]. Vertical error bars take account for the uncertainty in the determination of V_{mp} and J_{mp} (see Ch. 6). Data also shown in [116].

However, the 1D model including the thermal distribution (dashed line in Fig. 6.5) yields slightly larger J_{mp}. This fact suggests that some imperfections in the experimental setup cause slightly lower than possible current densities. Those imperfections may be the only approximately homogeneous magnetic field (see Ch. 4), an imperfect alignment of the magnetic field with the emitter-collector axis, or an inhomogeneous work function of the emitter. The latter might lead to some areas of the emitter not contributing to the emission and, consequently, a smaller than expected current.

Extrapolation to smaller scales

Remarkably, in the regime $d_{\mathrm{ec}} > w$ the measured data for both gate types shown in Fig. 6.5 very well reproduce the $1/d_{\mathrm{ec}}^2$-scaling behavior predicted by the 1D ideal gate model. This gives strong evidence that for every gate J_{mp} scales like $1/d_{\mathrm{ec}}^2$, which yields a route to practically large current densities: both w and d_{ec} need to be reduced.

Figure 6.6 shows an extrapolation of the data shown in Fig. 6.5 into this regime. For comparison, data for the case without gate and for a hypothetical gate with a mesh diameter of $w = 0.2\,\mathrm{mm}$ are also shown. As can be seen, for an ideal gate a current density J_{mp} clearly exceeding $1\,\mathrm{A/cm^2}$ is predicted at emitter-collector spacings of $d_{\mathrm{ec}} \lesssim 100\,\mu\mathrm{m}$. As is shown on the right-hand side of Fig. 6.6, this corresponds to power densities of several $\mathrm{W/cm^2}$, the exact numbers depending on the collector work function.

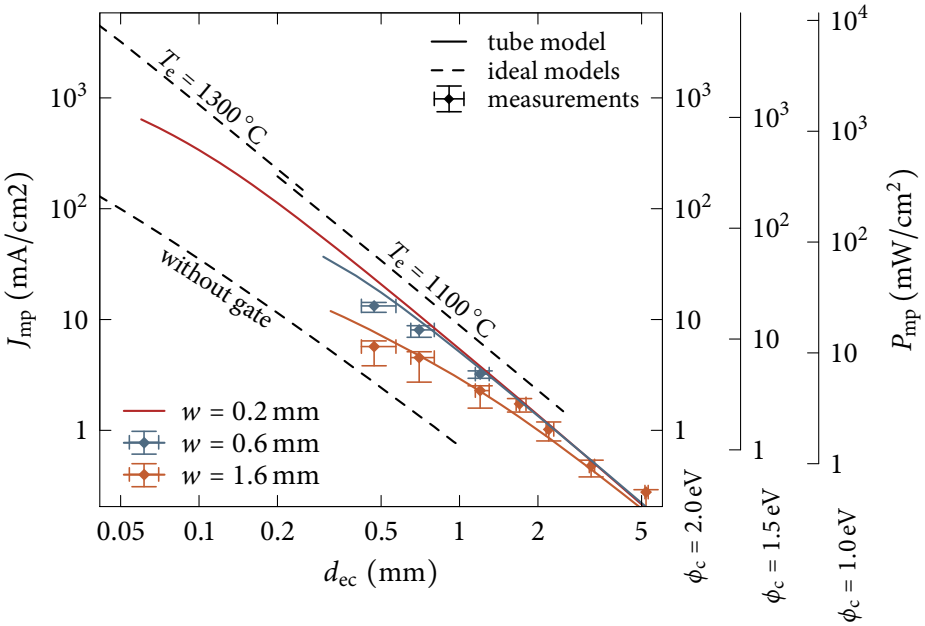

Figure 6.6: Collector current density J_{mp} at $V_l = V_{mp}$ as a function of the emitter-collector spacing d_{ec} for the two gate types studied in this thesis and a hypothetical one with a mesh diameter of $w = 0.2\,\text{mm}$. An extrapolation based on the ideal gate model including the thermal distribution yields that J_{mp} clearly exceeds $1\,\text{A/cm}^2$ at $d_{ec} \leq 100\,\mu\text{m}$. For comparison, the predictions of an ideal model without gate are given. On the right hand side a projection of the output power density for three different, hypothetical collector work functions is given. To obtain these numbers, the current density is multiplied with $V_{mp} = (\phi_e - \phi_c)/e$, with a hypothetical emitter work function of $\phi_e = 3.0\,\text{eV}$. The dashed lines were calculated by C. Stephanos [19]. Data also shown in [116].

6.3 Attainable efficiencies

After it has been shown that our experiments and models give evidence for the possibility to produce practically high output power densities, I will now discuss the possible efficiencies of such systems. This discussion deviates from the one given for ideal TICs in Ch. 3.2 in three aspects, which will be discussed below and can also be seen from Fig. 6.7.

First, as has been shown in the preceding sections, the gate can suppress the space charge only up to a certain current density, which is determined by the gate geometry, the applied voltage, and the gap width. As I want to discuss the fundamental physics involved, an ideal gate generating a homogeneous electric field is assumed. Thus, the space-charge-limited current density J_{mp}, which is emitted from the emitter, can be determined from C. Stephanos' ideal gate model [19] (see *e.g.* the dashed line in Fig. 6.6).

For simplicity, the back-emitted current I_{be} is treated by the Richardson-Dushman equation (Eq. 3.3), which is modified to account for the reflection of back-emitted electrons by the residual space-charge barrier:

$$I_{be} = AA_R T_c^2 \exp \frac{-(\phi_c + \varphi_{max})}{k_B T_c},$$

were φ_{max} is the maximum of the total electric potential $\varphi(z)$, measured from the common local vacuum potentials of emitter and collector (compare to Figs. 3.12 and 3.14). It is obtained as a result of the 1D ideal gate model [19]. This approach is reasonable because for all practical configurations, I_{be} is significantly smaller than I_e. Consequently, I_{be} can be neglected when calculating J_{mp} and φ_{max} in the framework of the ideal gate model.

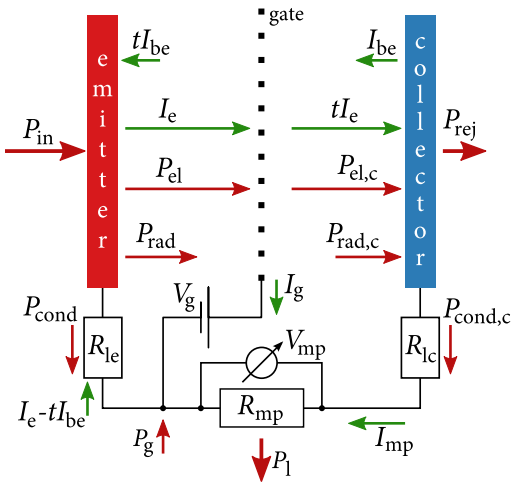

Figure 6.7: Sketch of energy flow (red arrows) and current (green arrows) channels relevant for TECs. Owing to the finite gate transparency t, only the part tI_e of the current I_e emitted from the emitter reaches the collector. Similarly, only the part tI_{be} of the back-emission reaches the emitter. The rest of both emitted currents is lost to the gate current $I_g = (1 - t)(I_e + I_{be})$. The current through the load is given by $I_{mp} = tI_e - I_{be}$. Heat is removed from the emitter by electron cooling (P_{el}), thermal radiation (P_{rad}) and heat conduction (P_{cond}).

Second, some power $P_g = I_g V_g$ is consumed to sustain the electric field. As P_g is of electrical nature, it must be directly subtracted from the produced output power. Hence, the efficiency is given by

$$\eta_{tec} = \frac{P_{out}}{P_{in}} = \frac{P_l - P_g}{P_{in}}, \tag{6.1}$$

where – as before – the load power is

$$P_l = (V_{mp} - V_{lead}) I_{mp}.$$

The heat input is the sum of an electronic, a radiation and a conduction term:

$$P_{in} = P_{el} + P_{rad} + P_{cond}. \tag{6.2}$$

As in the case without gate, V_{lead} is the voltage drop across the leads connecting emitter and collector with the external load cycle.

Third, owing to its finite transparency $0 < t < 1$, the gate reduces the transfer of current and thermal radiation across the vacuum gap. Thus, the net current I_{mp} transported to the collector and through the load becomes

$$I_{mp} = tI_e - I_{be}.$$

Similarly, the power loss on the gate becomes

$$P_g = V_g I_g = V_g (1 - t)(I_e + I_{be}). \tag{6.3}$$

It can be seen that I_{mp} and I_g add up to the net current emitted from the emitter: $I_g + I_{mp} = (1 - t)(I_e + I_{be}) + tI_e - I_{be} = I_e - tI_{be}$.

Again, it is necessary to distinguish whether the power transported to the collector is regarded as loss (stand-alone TEC) or recycled in a secondary heat engine (combined cycle).

Stand-alone thermoelectronic energy converters

In analogy to Ch. 3.2, the voltage drop V_{lead} in the leads is only due to the emitter lead R_{le} as the collector lead can be neglected for stand-alone TECs. The current through this lead equals the net emitter current $I_e - tI_{be}$, yielding $V_{lead} = R_{le}(I_e - tI_{be})$.

Consequently, the load power P_l becomes:

$$P_\mathrm{l} = \left[(\phi_\mathrm{e} - \phi_\mathrm{c})/e - R_\mathrm{le}(I_\mathrm{e} - tI_\mathrm{be})\right] I_\mathrm{mp}. \tag{6.4}$$

In the same way as it modifies the current, the gate modifies the heat loss from the emitter due to thermal radiation:

$$P_\mathrm{rad} = \sigma\varepsilon A(T_\mathrm{e}^4 - tT_\mathrm{c}^4), \tag{6.5}$$

thermal and electric conduction through the emitter lead:

$$P_\mathrm{cond} = \frac{L}{2R_\mathrm{le}}(T_\mathrm{e} - T_0)^2 - (I_\mathrm{e} - tI_\mathrm{be})^2 R_\mathrm{le}/2, \tag{6.6}$$

and evaporation and condensation of electrons:

$$P_\mathrm{el} = I_\mathrm{e}/e \cdot (\phi_\mathrm{e} + \varphi_\mathrm{max} + 2k_\mathrm{B}T_\mathrm{e}) - tI_\mathrm{be}/e \cdot (\phi_\mathrm{e} + \varphi_\mathrm{max} + 2k_\mathrm{B}T_\mathrm{c}). \tag{6.7}$$

From Eq. 6.1, the general expression for the heat-to-electricity efficiency of stand-alone TECs becomes:

$$\eta_\mathrm{tec} = \frac{\left[(\phi_\mathrm{e} - \phi_\mathrm{c})/e - R_\mathrm{le}(I_\mathrm{e} - tI_\mathrm{be})\right] I_\mathrm{mp} - V_\mathrm{g}(1-t)(I_\mathrm{e} + I_\mathrm{be})}{P_\mathrm{rad} + P_\mathrm{cond} + P_\mathrm{el}} \tag{6.8}$$

with P_rad, P_cond, and P_el as in Eqs. 6.5 to 6.7.

In this thesis, a gate transparency of $t \gtrsim 0.8$ has been demonstrated experimentally (see Ch. 5), but the system has not been optimized for high transparencies. Hence, there is no indication that far higher transparencies are unrealistic. In particular if the emission capability of the emitter is shaped in an inhomogeneous way such that no emission occurs near the gate wires, $t \to 1$ appears possible. The high importance of the transparency can be seen from Fig. 6.8, where the efficiency as a function of the gate voltage is shown for a series of transparencies.

In calculating the data shown in Fig. 6.8, an experimentally demonstrated collector work function of 0.9 eV [85] was assumed.

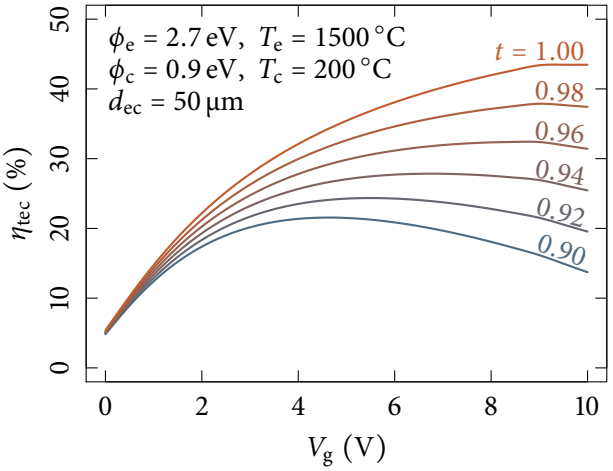

Figure 6.8: Calculated heat-to-electricity conversion efficiency η_{tec} of a TEC as a function of the gate voltage V_g for a series of gate transparencies t. The current I_e as a function of V_g was determined by C. Stephanos via the ideal gate model including the thermal distribution. The efficiency is then obtained via Eq. 6.8.

Combined cycles

The consequences of the TEC feeding its rejected heat P_{rej} into a secondary heat engine are discussed for the case of a state-of-the-art steam turbine (T_{in} = 600 °C, η_s = 45 %) [17, 117], as it is typically used in coal-fired power plants.

Taking into account the power loss due to the gate current, the efficiency of the combined cycle becomes (compare Eq. 3.11):

$$\eta_{cc} = \frac{P_l - P_g + \eta_s(P_{el,c} + P_{rad,c} - P_{cond,c})}{P_{el} + P_{rad} + P_{cond}}, \tag{6.9}$$

where – as compared to the stand-alone system – the load power P_l is additionally reduced by the ohmic loss in the collector lead R_{lc}:

$$P_l = \left[(\phi_e - \phi_c)/e - R_{le}(I_e - tI_{be}) - R_{lc}I_{mp}\right] I_{mp}.$$

As compared to the case without gate, some slight modifications to the channels of heat transport to and from the collector are necessary:

$$\begin{aligned} P_{el,c} &= tI_e/e \cdot (\phi_c + 2k_B T_e) - I_{be}/e \cdot (\phi_c + 2k_B T_c), \\ P_{rad,c} &= \sigma\varepsilon A(tT_e^4 - T_c^4), \text{ and} \\ P_{cond,c} &= \frac{L}{2R_{lc}}(T_c - T_0)^2 - I_{mp}^2 R_{lc}/2. \end{aligned} \tag{6.10}$$

Thereby, $P_{cond,c}$ did not have to be modified because the effect of the gate is already contained in I_{mp}.

PETE systems

As was pointed out in Ch. 3.1, the efficiency of solar-heated TICs can be enhanced by using the quantum character of the incident light – utilizing the photoelectric effect to achieve photoexcitations across the bandgap E_{gap} of a semiconducting emitter – in addition to purely thermal emission. An extensive discussion of the efficiencies of PETE devices is given in [69]. However, the space charge is neglected there and no gate is taken into account.

To calculate the efficiency of such PETE devices in the presence of the space charge, which is partially or fully suppressed by an ideal gate, a fixed emitted current $I_{\mathrm{e,pete}}$ and emitter temperature T_{e} need to be assumed. $I_{\mathrm{e,pete}}$ then corresponds to the Richardson-Dushman saturation current from the emitter in the preceding discussion. Consequently, the space-charge limited current I_{mp} can be calculated from $I_{\mathrm{e,pete}}$ via C. Stephanos' 1D models.

If T_{e} is chosen high enough, in an ideal PETE device it can be assumed that every incident photon with an energy higher than E_{gap} creates an emitted electron [69]. From [69] it may furthermore be concluded that this typically is the case if the hypothetical Richardson-Dushman current across the electron-affinity barrier E_{a} exceeds $I_{\mathrm{e,pete}}$ by at least a factor of 100. Electrons that were excited into the conduction band can then be assumed to be thermally emitted therefrom faster than they recombine. As T_{e} rather than E_{a} is the input parameter of this calculation, E_{a} needs to be calculated from T_{e} by solving the Richardson-Dushman equation for E_{a}:

$$\begin{aligned} A A_{\mathrm{R}} T_{\mathrm{e}}^2 \exp \frac{-E_{\mathrm{a}}}{k_{\mathrm{B}} T_{\mathrm{e}}} &\gtrsim 100 \cdot I_{\mathrm{e,pete}} \\ \Rightarrow E_{\mathrm{a}} &\lesssim k_{\mathrm{B}} T_{\mathrm{e}} \ln \frac{100 \cdot I_{\mathrm{e,pete}}}{A A_{\mathrm{R}} T_{\mathrm{e}}^2}. \end{aligned}$$

The input power P_{in} required to maintain a stable emitter temperature can be calculated by substituting I_{mp} into Eq. 6.2. As the emitter is heated by sunlight, P_{in} defines the effective concentration c_{eff} of the incident light:

$$c_{\mathrm{eff}} I_{\mathrm{sun}} A = P_{\mathrm{in}},$$

where I_{sun} is the intensity of the incident, not yet concentrated sunlight. The effective concentration c_{eff} refers to the emitter area A. Consequently, it is not to be confused with the concentration c from Ch. 3.2, which refers to the area A_{b} of the light-absorbing spot on the emitter. It is $c_{\mathrm{eff}} A = c A_{\mathrm{b}}$.

To satisfy the self-consistency of the calculation, the bandgap needs to be chosen as a function of c_{eff} such that the number of photoexcitations matches $I_{\mathrm{e,pete}}$. Hence, the material parameter E_{gap} is again obtained as a result of the calculation.

Finally, from E_{a}, E_{gap}, and T_{e} the work function $\phi_{\mathrm{e}} = E_{\mathrm{vac}} - \mu_{\mathrm{e}}$ of the emitter must be determined. As the load voltage – and consequently the output power – increases with increasing ϕ_{e}, it is optimal to use a p-doped semiconductor, in which the electrochemical potential at low temperatures is near the bottom of the bandgap. Consequently, at low temperatures it is $\phi_{\mathrm{e}} \approx E_{\mathrm{gap}} + E_{\mathrm{a}}$. However, with increasing emitter temperature the electrochemical potential rises towards the middle of the bandgap, the exact value depending on the acceptor level, acceptor concentration, bandgap, and T_{e}. For simplicity, it is therefore assumed that the chemical potential lies in the middle between the worst case – the middle of the bandgap – and the best case – the bottom of the bandgap –, yielding:

$$\phi_{\mathrm{e}} = E_{\mathrm{a}} + 3/4 \cdot E_{\mathrm{gap}}.$$

From ϕ_{e} and I_{mp} the heat-to-electricity efficiencies of both stand-alone and combined-cycle PETE devices can be calculated as described above.

The light-to-electricity efficiency is finally obtained by multiplying the heat-to-electricity efficiency with $1 - \sigma T_{\mathrm{e}}^4/(cI_{\mathrm{sun}})$, as was already discussed in Ch. 3.2 (see Eq. 3.13).

Projected efficiencies

Figure 6.9a shows the projected efficiencies of TECs, which were calculated as was described above. Thereby parameters were assumed, which seem well realizable: $d_{\mathrm{ec}} = 30\,\mu\mathrm{m}$, $t = 0.98$, and $\phi_{\mathrm{c}} = 0.9\,\mathrm{eV}$. As can be seen, the calculations predict promising heat-to-electricity efficiencies above 40 %, which compares well to the efficiency of a hypothetical thermoelectric having $ZT = 3$ over a temperature range from $T_{\mathrm{in}} = 1500\,^{\circ}\mathrm{C}$ to $T_{\mathrm{out}} = 200\,^{\circ}\mathrm{C}$.

The light-to-electricity efficiencies obtained for PETE devices are even higher, even though these data were already corrected for the black spot required to couple the incident sunlight into the emitter (see Ch. 3.2). Thereby a light-concentration factor of $c = 10000$ was assumed, which seems realizable [89]. For an optimum collector work function of $\phi_{\mathrm{c}} = 0.55\,\mathrm{eV}$ an efficiency of 53 % is projected, which is well above the present world record for laboratory-scale photovoltaic cells (43.5 %) [5].

As Fig. 6.9b shows, for combined-cycle systems with state-of-the-art steam turbines ($\eta_{\mathrm{s}} = 45\,\%$, $T_{\mathrm{in}} = 600\,^{\circ}\mathrm{C}$) an increase of the total conversion efficiency in the order of 10

percentage points is projected. If such system were used in coal-fired power plants, this would reduce CO_2 emissions and coal consumption per electricity output by 18 %.

Similarly, for PETE-TECs used in combined cycles with state-of-the-art steam turbines a maximum light-to-electricity efficiency of 54 % is projected. Such systems would be the by far most efficient system for the conversion of solar radiation to electricity. Remarkably, this efficiency may be obtained with well realizable parameters. In particular, the optimum collector work function for these systems is as high as 1.5 eV.

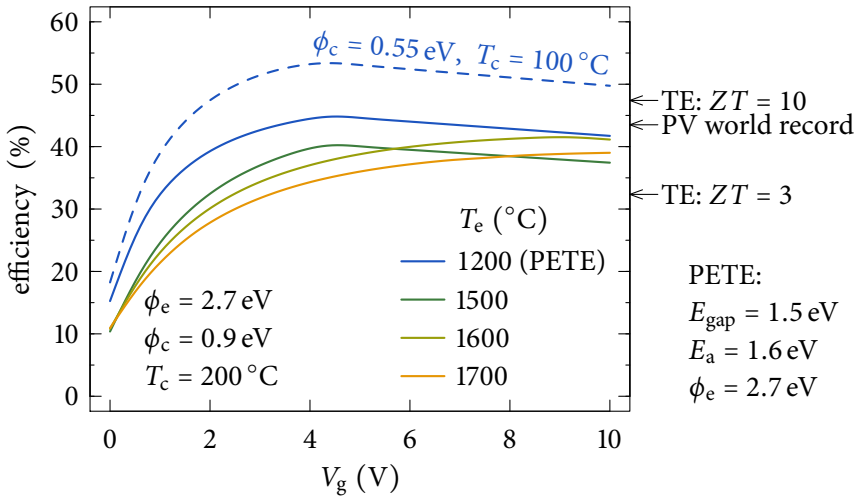

(a) Stand-alone TECs.

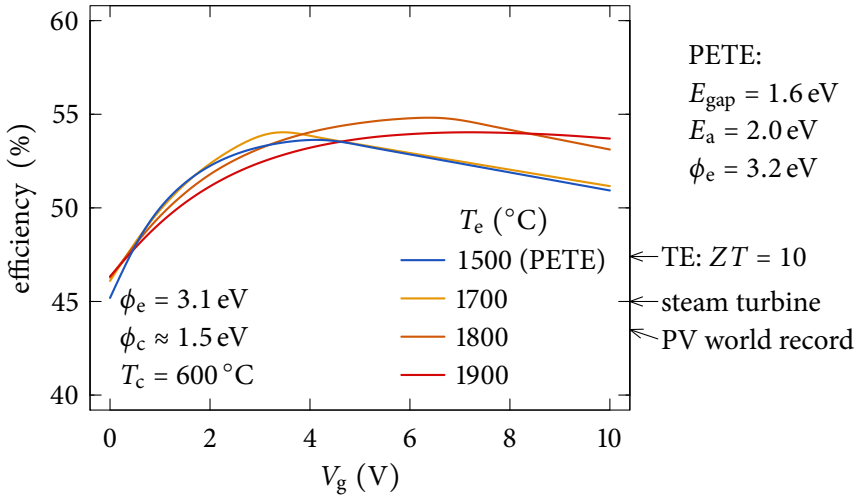

(b) Combined-cycle systems.

Figure 6.9: Calculated efficiencies for stand-alone TECs (**a**) and combined-cycle systems (**b**) for d_{ec} = 30 µm and t = 0.98. In both cases ϕ_e was chosen such that maximum efficiencies are obtained. The data for the PETE systems were corrected to account for the additional loss channel due to the black spot on the emitter (see Ch. 3.2). Consequently, they correspond to light-to-electricity efficiencies. Thereby a concentration of c = 10000 and a solar intensity of I_{sun} = 900 W/m^2, corresponding to the AM1.5 direct+circumsolar reference spectrum [91], were assumed. The rest of the data corresponds to heat-to-electricity efficiencies. For comparison, the world record for laboratory-scale photovoltaic cells (43.5 % [5]) and the efficiencies of hypothetical thermoelectric generators are given [118]. For the latter, upper and lower temperatures of 1500 °C and 200 °C were assumed. To calculate the efficiencies of the combined-cycle systems, the TECs were assumed to feed their waste heat into state-of-the-art steam turbines operating at η_s = 45 % and receiving heat at the collector temperature of T_c = 600 °C. The collector work function was chosen such that the efficiency is maximized. To obtain the data shown here, the space-charge-limited emitter current density J_e as a function of the load voltage was calculated by C. Stephanos [19] via the ideal gate model including the thermally distributed initial velocity. Therefrom, the efficiencies were calculated via Eqs. 6.8 and 6.9. Data also shown in [116].

7 Summary and outlook

By the time of the start of this thesis, the suppression of the space charge by electric and magnetic fields was believed to be impractical [21]. In the community, the cesium and close-space approaches were exclusively investigated.

In this thesis, a proof-of-concept of thermoelectronic energy conversion was given. It was demonstrated experimentally that the space charge can be suppressed by an electric field, thereby significantly enhancing the output current of the device. At the same the time, it was demonstrated that the applied magnetic field prevents electrons from hitting the gate wires. Although neither the collectors nor the gates were optimized to maximize the output power, the proof-of-concept generator produces more electric power than is consumed on the gate. However, owing to limitations of the miniaturization of the gap width, the output power was limited to tens of milliwatts.

In collaboration with C. Stephanos [19], numerical and analytical models were developed to estimate output current densities for the configurations studied experimentally as well as for future systems. The predictions based on these models compare well with experimental data on the dependence of the output current on the gate voltage, the gap width, and the width of the gate meshes.

An extrapolation of the system behavior to small gap widths gives strong evidence that practically high output power densities and conversion efficiencies may be achieved. In particular, efficiencies exceeding the world record for photovoltaic cells and the best thermoelectric materials are projected. Whereas no physical reason prohibiting the realization of such devices could be found, substantial efforts both in engineering and materials science are still required.

In the following section I will briefly address issues to be faced in these two directions in the future.

System fabrication

As Ch. 6 has shown, TECs with emitter-collector spacings below 100 µm are required for practically large output current densities. Such devices may be fabricated in a flip-chip technique, where the gate, necessary spacers, and possibly further components are

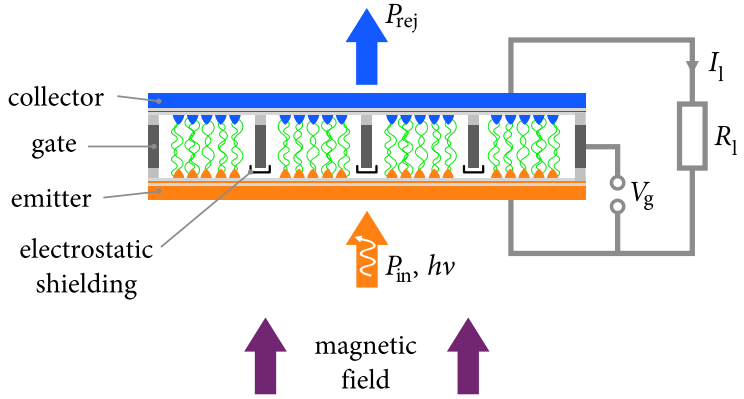

Figure 7.1: Sketch of a possible microfabricated TEC. The emission of electrons is restricted to those areas of the emitter that are aligned with the meshes in the gate. For this purpose, nanotips and the applied electric field decrease the effective work function of the emitter – and possibly the collector as well – in those regions. The gate current may be further reduced by electrostatic shields, which tailor the geometry of the electric field in a favorable way. Figure also shown in [116].

deposited on top of either the emitter or the collector by techniques as they are known in the microelectromechanical systems (MEMS) industry. To give just a few examples, electron beam evaporation, photolithography, and chemical etching might enable the growth of practical gate geometries. After the growth and patterning processes, emitter and collector are joined to form an integrated assembly, as illustrated in Fig. 7.1.

Honeycomb gate structures seem to be an optimum choice due to their optimum surface filling. If such structures are used, the desired electric field can be generated while only a minimum fraction of the emitter surface is covered by the gate wires. Obviously, the surface covering can be further reduced by decreasing the width of the grid bars. However, as the mesh width will have to be reduced below 100 µm, the radii of gyration r_g of the electrons along the magnetic field lines can no longer be neglected. Instead, the effective transparency will be decreased due to the finite r_g [19].

To attain high effective transparencies despite finite radii of gyration, the emission of electrons from the emitter may be tailored such that no emission occurs in those regions of the emitter that are aligned with the gate wires. For this purpose, a work-function-reducing layer may be structured on the emitter. Alternatively, as sketched in Fig. 7.1, nanometer-sized tips on both the emitter and collector in combination with the electric field generated by the gate can reduce the work function in desired regions of both electrodes via the Schottky effect (see Ch. 3.1). The gate current may be further reduced by electrostatic shields, which screen the electric field in those regions of the emitter that are

aligned with the gate wires. Additionally, inhomogeneous magnetic fields might guide the emitted electrons through the gate meshes.

As a general rule of thumb, the mesh diameter w should be equal or smaller than d_{ec} so that the electric field is approximately homogeneous. Otherwise, unfavorably high gate voltages have to be applied to create electric fields large enough to suppress the space charge in the center of the meshes. At the same time, the thickness of the gate should be large. For a fixed gap width, thicker gates increase the electric fields in those regions of the emitter that are aligned with the mesh centers. Obviously, the thickness of the gate can only be increased to a certain fraction of the gap width because stable electrical insulation needs to be provided.

To obtain high conversion efficiencies, the system needs to be highly optimized with respect to the heat flow. Heat has to be efficiently transported to the emitter, and thermal radiation therefrom should be minimized and reflected back. As Ioffe has already pointed out [119], even the collector surface may be used as heat shield for the emitter because the absorption of electrons (governed by the first few atomic layers) can in principle be decoupled from the emission and absorption of infrared radiation (governed by a layer in the order of some hundred nanometers).

Furthermore, as has been mentioned in Ch. 3.2 and Ch. 6.3, the electric wiring needs to be optimized to minimize both ohmic losses and conduction of heat away from the emitter.

Identification and development of suitable materials

The probably most critical component of any thermoelectronic converter is the collector as it needs to offer a very small work function at elevated temperatures and high current densities for a long time. Historically, the adsorption of cesium atoms on the surfaces of metals has been the most successful approach to solve this problem [21]. At cesium background pressures as low as 1×10^{-6} mbar such cesiated collectors might in principle offer work functions as low as 0.7 eV [86, p. 123], which is very close to the optimum work function of collectors being operated at practical temperatures around 100 °C. Hence, adding a very small amount of cesium to the vacuum chamber might already by sufficient to achieve desirably low work functions.

However, the high reactivity of cesium and resulting material constraints on other parts of the TEC, as well as safety considerations might prohibit the widespread use of cesiated collectors. In this case, other material systems might become an important option. Recently, work functions of 0.9 eV and 1.3 eV have been reported for phosphorous and

nitrogen doped diamond after a surface treatment with hydrogen plasma [85, 120]. For the room temperature stable electride $[Ca_{24}Al_{28}O_{64}]^{4+}(4e^-)$ a work function of 0.6 eV was measured [121], although somewhat higher values were reported later [122, 123].

It should be noted that, despite those two material classes might offer an alternative to cesiated surfaces, substantially more research will be required to provide long-time reliable collectors based upon them.

Operating a TEC as a topping cycle to a secondary heat engine both increases the total conversion efficiency and makes possible the use of less critical collector materials. As was pointed out in Ch. 6.3, the optimum work function of such combined cycles lies in the range between 1.3 eV and 2.0 eV. Sufficiently low work functions for these systems might therefore be available from the material class of alkaline-earth oxides on metals [86]. These systems, typically barium oxide on tungsten[1], are commercially available today and have proven long-term stability in the order of ten years [124] at temperatures around 1000 °C. If operated as the collector of a TEC, which will typically be significantly colder than that, these systems might remain stable even longer.

Remarkably, the most critical issue of stand-alone and combined-cycle TEC systems – the need to obtain a low collector work function – appears to be resolvable.

Depending on other system parameters – mainly on the collector work function and the temperatures of the hot and cold reservoirs – a broad variety of material systems may be considered for use as emitter materials. In the regime of low temperatures – and consequently very low collector work functions – the emitter should have a work function around 2.0 eV to provide sufficiently large current densities. As discussed above, these work functions can be provided by alkaline-earth oxides on metals.

With increasing emitter temperature, higher emitter work functions should be used as this increases the output voltage. Thereby, the range from 2.0 eV to 4.0 eV, which will be interesting in the range 1000 °C < T_e < 2500 °C, is covered by various oxides (CaO: ≈ 2.0 eV, La_2O_3: ≈ 3.0 eV, the barium-tungsten oxides: 1.8 eV–3.3 eV, or TiO: 3.9 eV), borides (LaB_6: ≈ 2.5 eV, MoB_2: 3.4 eV), and various semiconductor compounds (La_2S_3: 2.9 eV-4.3 eV, depending on temperature), to give just a few examples [86][2]. Furthermore, refractory metals doped with work-function reducing oxides cover the range from approximately 3.0 eV to approximately 4.5 eV [96, 97].

[1] The emitters used in this thesis are from this material class.

[2] Fomenko and Samsonov's *Handbook of Thermionic Properties* [86] provides an extensive collection of emission parameters of further material systems.

Bibliography

[1] W. Shockley and H. J. Queisser, *Detailed balance limit of efficiency of p-n junction solar cells*, Journal of Applied Physics **32**, 3, pp. 510–519 (1961), doi:10.1063/1.1736034.

[2] M. A. Green, *Third generation photovoltaics: solar cells for 2020 and beyond*, Physica E: Low-dimensional Systems and Nanostructures **14**, 1–2, pp. 65–70 (2002), doi:10.1016/S1386-9477(02)00361-2.

[3] M. Ley *et al.*, *Thermodynamic efficiency of an intermediate band photovoltaic cell with low threshold Auger generation*, Journal of Applied Physics **98**, 4, pp. 044905 1–5 (2005), doi:10.1063/1.2010622.

[4] G. Conibeer *et al.*, *Silicon nanostructures for third generation photovoltaic solar cells*, Thin Solid Films **511–512**, pp. 654–662 (2006), doi:10.1016/j.tsf.2005.12.119.

[5] M. A. Green *et al.*, *Solar cell efficiency tables (version 40)*, Progress in Photovoltaics: Research and Applications **20**, 5, pp. 606–614 (2012), doi:10.1002/pip.2267.

[6] REN21, *Renewables 2012 Global Status Report*, available from www.ren21.net (Paris, 2012).

[7] R. M. Swanson, *Photovoltaics power up*, Science **324**, 5929, pp. 891–892 (2009), doi:10.1126/science.1169616.

[8] C. Richter, ed., *SolarPACES Annual Report 2008*, available from www.solarpaces-csp.org/Library/AnnualReports (International Energy Agency, 2009).

[9] H. Müller-Steinhagen and F. Trieb, *Concentrating solar power*, Ingenia, 18, pp. 43–50 (2004).

[10] D. M. Rowe, *Thermoelectrics Handbook: Macro to Nano* (CRC Press, 2005), ISBN: 9780849322648.

[11] T. M. Tritt and M. A. Subramanian, *Thermoelectric materials, phenomena, and applications: a bird's eye view*, MRS Bulletin **31**, 03, pp. 188–198 (2006), doi:10.1557/mrs2006.44.

[12] D. M. Rowe, ed., *CRC Handbook of Thermoelectrics* (CRC Press, 1995), ISBN: 0849301467.

[13] C. B. Vining, *An inconvenient truth about thermoelectrics*, Nature Materials **8**, 2, pp. 83–85 (2009), doi:10.1038/nmat2361.

[14] T. M. Tritt *et al.*, *Thermoelectrics: direct solar thermal energy conversion*, MRS Bulletin **33**, 04, pp. 366–368 (2008), doi:10.1557/mrs2008.73.

[15] L. E. Bell, *Cooling, heating, generating power, and recovering waste heat with thermoelectric systems*, Science **321**, 5895, pp. 1457–1461 (2008), doi:10.1126/science.1158899.

[16] B. Y. Moyzhes and T. H. Geballe, *The thermionic energy converter as a topping cycle for more efficient heat engines—new triode designs with a longitudinal magnetic field*, Journal of Physics D: Applied Physics **38**, 5, pp. 782–786 (2005), doi:10.1088/0022-3727/38/5/017.

[17] R. Kneer, RWTH Aachen, private communication with Jochen Mannhart, 2012.

[18] *Key World Energy Statistics 2012*, available from http://www.iea.org/publications/freepublications/publication/name,31287,en.html (International Energy Agency, 2012).

[19] C. Stephanos, *Thermoelectronic Power Generation from Solar Radiation and Heat*, PhD thesis (Universität Augsburg, 2012).

[20] D. R. Lide, ed., *CRC Handbook of Chemistry and Physics*, 80th ed. (CRC Press, Boca Raton, 1999), ISBN: 0849304806.

[21] G. N. Hatsopoulos and E. P. Gyftopoulos, *Thermionic Energy Conversion Volume I: Processes and Devices* (MIT Press, Cambridge and London, 1973), ISBN: 0262080591.

[22] G. N. Hatsopoulos and E. P Gyftopoulos, *Thermionic Energy Conversion Volume II: Theory, Technology and Application* (MIT Press, Cambridge and London, 1979), ISBN: 0262080591.

[23] N. S. Rasor, *Thermionic energy-conversion plasmas*, IEEE Transactions on Plasma Science **19**, 6, pp. 1191–1208 (1991).

[24] J. Lee *et al.*, *Optimal emitter-collector gap for thermionic energy converters*, Applied Physics Letters **100**, 17, pp. 173904 1–4 (2012), doi:10.1063/1.4707379.

[25] J. D. Jackson, *Classical Electrodynamics*, 3rd ed. (Wiley, 1998), ISBN: 047130932X.

[26] W. H. Preece, *On a peculiar behaviour of glow-lamps when raised to high incandescence*, Proceedings of the Royal Society of London **38**, 235-238, pp. 219–230 (1884), doi:10.1098/rspl.1884.0093.

[27] W. Schlichter, *Die spontane Elektronenemission glühender Metalle und das glühelektrische Element*, Annalen der Physik **47**, 13, pp. 573–640 (1915), doi:10.1002/andp.19153521302.

[28] G. N. Hatsopoulos, *The Thermo-Electron Engine*, PhD thesis (Massachusetts Institute of Technology, 1956).

[29] K. G. Hernqvist *et al.*, *Thermionic energy converter*, RCA Review **19**, 2, pp. 244–258 (1958).

[30] G. N. Hatsopoulos and J. Kaye, *Measured thermal efficiencies of a diode configuration of a thermo electron engine*, Journal of Applied Physics **29**, 7, pp. 1124–1125 (1958), doi:10.1063/1.1723373.

[31] G. M. Grover *et al.*, *Properties of a thermoelectric cell*, Journal of Applied Physics **29**, 11, pp. 1611–1612 (1958), doi:10.1063/1.1723009.

[32] G. N. Hatsopoulos and J. Kaye, *Analysis and experimental results of a diode configuration of a novel thermoelectron engine*, Proceedings of the IRE **46**, 9, pp. 1574–1579 (1958), doi:10.1109/JRPROC.1958.286932.

[33] V. C. Wilson, *Conversion of heat to electricity by thermionic emission*, Journal of Applied Physics **30**, 4, pp. 475–481 (1959), doi:10.1063/1.1702391.

[34] National Research Council. Committee on Thermionic Research and Technology., *Thermionics Quo Vadis? An Assessment of the DTRA's Advanced Thermionics Research and Development Program* (National Academy Press, Washington D.C., 2001), ISBN: 030908282X.

[35] A. Stanculescu, ed., *The Role of Nuclear Power and Nuclear Propulsion in the Peaceful Exploration of Space.* (International Atomic Energy Agency, Vienna, 2005), ISBN: 9201074042.

[36] A. K. Hyder, *Spacecraft Power Technologies* (Imperial Colleague Press, London, 2003), ISBN: 1860941176.

[37] N. N. Ponomarev-Stepnoi *et al.*, *Russian space nuclear power and nuclear thermal propulsion systems*, Nuclear News **43**, 13, pp. 33–46 (2000).

[38] M. Tarasenko, *Twinkle, twinkle little topaz*, Bulletin of the Atomic Scientists **49**, 6, pp. 11–13 (1993).

[39] M. R. Martinez *et al.*, *Cylindrical inverted multi-cell (CIM) thermionic converter for solar power and propulsion systems*, AIP Conference Proceedings **746**, 1, pp. 926–934 (2005), doi:10.1063/1.1867217.

[40] S. F. Adams, *Solar thermionic space power technology testing: a historical perspective*, AIP Conference Proceedings **813**, 1, pp. 590–597 (2006), doi:doi:10.1063/1.2169239.

[41] P. N. Clark *et al.*, *Solar thermionic test in a thermal receiver*, AIP Conference Proceedings **813**, 1, pp. 598–606 (2006), doi:10.1063/1.2169240.

[42] H. Moss, *Thermionic diodes as energy converters*, Journal of Electronics and Control **2**, 4, pp. 305–322 (1957), doi:10.1080/00207215708937036.

[43] W. B. Nottingham, *Thermionic diode as a heat-to-electrical-power transducer*, Journal of Applied Physics **30**, 3, pp. 413–417 (1959), doi:10.1063/1.1735178.

[44] P. A. Lindsay and F. W. Parker, *Potential distribution between two plane emitting electrodes*, Journal of Electronics and Control **7**, 4, pp. 289–315 (1959), doi:10.1080/00207215908937215.

[45] H. F. Webster, *Calculation of the performance of a high-vacuum thermionic energy converter*, Journal of Applied Physics **30**, 4, pp. 488–492 (1959), doi:10.1063/1.1702393.

[46] P. A. Lindsay and F. W. Parker, *Potential distribution between two plane emitting electrodes II. thermionic engines*, Journal of Electronics and Control **9**, 2, pp. 81–111 (1960), doi:10.1080/00207216008962752.

[47] E. S. Rittner, *On the theory of the close-spaced impregnated cathode thermionic converter*, Journal of Applied Physics **31**, 6, pp. 1065–1071 (1960), doi:10.1063/1.1735747.

[48] G. Hatsopoulos *et al.*, *Prediction of optimum performance of vacuum-diode configuration of thermionic engines*, IRE Transactions on Electron Devices **7**, 3, pp. 117–122 (1960), doi:10.1109/T-ED.1960.14666.

[49] A. F. Dugan, *Contribution of anode emission to space charge in thermionic power converters*, Journal of Applied Physics **31**, 8, pp. 1397–1400 (1960), doi:10.1063/1.1735850.

[50] D. B. King *et al.*, *Results from the microminiature thermionic converter demonstration testing program*, in Energy Conversion Engineering Conference and Exhibit, Vol. 1 (2000), pp. 272 –282, doi:10.1109/IECEC.2000.870697.

[51] D. B. King *et al.*, *Microminiature thermionic converters*, United States patent 6294858, filed Feb. 25, 1999 and issued Sep. 25, 2001.

[52] D. B. King *et al.*, *Microminiature thermionic converters*, United States patent 6509669, filed Jun. 28, 2001 and issued Jan. 21, 2003.

[53] C. Zhang *et al.*, *Micro combustion-thermionic power generation: feasibility, design and initial results*, in 12th International Conference on Transducers, Solid-State Sensors, Actuators and Microsystems, Vol. 1 (2003), pp. 40–44, doi:10.1109/SENSOR.2003.1215248.

[54] D. B. King *et al.*, *Low work function material development for the microminiature thermionic converter.* Tech. rep. (Sandia National Laboratories, Albuquerque and Livermore, 2004).

[55] P. G. Tanner *et al.*, *Developments in thermionic energy converters*, IEE Proceedings - Science, Measurement and Technology **152**, 1, pp. 1–6 (2005), doi:10.1049/ip-smt:20051050.

[56] A. N. Korotkov and K. K. Likharev, *Possible cooling by resonant Fowler-Nordheim emission*, Applied Physics Letters **75**, 16, pp. 2491–2493 (1999), doi:10.1063/1.125058.

[57] Y. Hishinuma *et al.*, *Refrigeration by combined tunneling and thermionic emission in vacuum: Use of nanometer scale design*, Applied Physics Letters **78**, 17, pp. 2572–2574 (2001), doi:10.1063/1.1365944.

[58] Y. Hishinuma *et al.*, *Vacuum thermionic refrigeration with a semiconductor heterojunction structure*, Applied Physics Letters **81**, 22, pp. 4242–4244 (2002), doi:10.1063/1.1523653.

[59] H. T. Chua *et al.*, *Thermionic and tunneling cooling thermodynamics*, Applied Physics Letters **84**, 20, pp. 3999–4001 (2004), doi:10.1063/1.1738939.

[60] T. Zeng, *Thermionic-tunneling multilayer nanostructures for power generation*, Applied Physics Letters **88**, 15, pp. 153104 1–3 (2006), doi:10.1063/1.2192973.

[61] A. N. Tavkhelidze, *Nanostructured electrodes for thermionic and thermotunnel devices*, Journal of Applied Physics **108**, 4, pp. 044313 1–7 (2010), doi:10.1063/1.3464256.

[62] J. H. Lee *et al.*, *Microfabricated silicon carbide thermionic energy converter for solar electricity generation*, in IEEE 25th International Conference on Micro Electro Mechanical Systems (2012), pp. 1261 –1264, doi:10.1109/MEMSYS.2012.6170386.

[63] G. D. Mahan, *Thermionic refrigeration*, Journal of Applied Physics **76**, 7, pp. 4362–4366 (1994), doi:10.1063/1.357324.

[64] X. C. Xuan, *Combined thermionic-thermoelectric refrigerator*, Journal of Applied Physics **92**, 8, pp. 4746–4750 (2002), doi:10.1063/1.1509101.

[65] J. R. Smith *et al.*, *Theory of space charge limited regime of thermionic energy converter with negative electron affinity emitter*, Journal of Vacuum Science & Technology B: Microelectronics and Nanometer Structures **27**, 3, pp. 1132–1141 (2009), doi:10.1116/1.3125282.

[66] L. Chen *et al.*, *Performance analysis of a vacuum thermionic refrigerator with external heat transfer*, Journal of Applied Physics **107**, 10, pp. 104507 1–7 (2010), doi:10.1063/1.3428419.

[67] N. D. Lang and W. Kohn, *Theory of metal surfaces - work function*, Physical Review B **3**, 4, pp. 1215–1223 (1971).

[68] G. P. Smestad, *Conversion of heat and light simultaneously using a vacuum photodiode and the thermionic and photoelectric effects*, Solar Energy Materials and Solar Cells **82**, 1-2, pp. 227–240 (2004), doi:10.1016/j.solmat.2004.01.020.

[69] J. W. Schwede *et al.*, *Photon-enhanced thermionic emission for solar concentrator systems*, Nature Materials **9**, 9, pp. 762–767 (2010), doi:10.1038/nmat2814.

[70] A. Einstein, *Über einen die Erzeugung und Verwandlung des Lichtes betreffenden heuristischen Gesichtspunkt*, Annalen der Physik **322**, 6, pp. 132–148 (1905), doi:10.1002/andp.19053220607.

[71] O. W. Richardson, *On the negative radiation from hot platinum*, Proceedings of the Cambridge Philosophical Society, pp. 286–295 (1901).

[72] O. W. Richardson, *The Emission of Electricity from Hot Bodies* (Longmans, Green and Co., London, 1916).

[73] S. Dushman, *Electron emission from metals as a function of temperature*, Physical Review **21**, 6, pp. 623–636 (1923), doi:10.1103/PhysRev.21.623.

[74] R. H Fowler and L. Nordheim, *Electron emission in intense electric fields*, Proceedings of the Royal Society of London A **119**, pp. 173–181 (1928).

[75] W. Schottky, *Über kalte und warme Elektronenentladungen*, Zeitschrift für Physik A **14**, 1, pp. 63–106 (1923), doi:10.1007/BF01340034.

[76] C. D. Child, *Discharge from hot CaO*, Physical Review **32**, 5, pp. 492–511 (1911), doi:10.1103/PhysRevSeriesI.32.492.

[77] I. Langmuir, *The effect of space charge and residual gases on thermionic currents in high vacuum*, Physical Review **2**, 6, pp. 450–486 (1913), doi:10.1103/PhysRev.2.450.

[78] I. Langmuir, *The effect of space charge and initial velocities on the potential distribution and thermionic current between parallel plane electrodes*, Physical Review **21**, 4, pp. 419–435 (1923), doi:10.1103/PhysRev.21.419.

[79] Lord Kelvin, *Contact Electricity of Metals*, Philosophical Magazine Series 5 **46**, 278, pp. 82–120 (1898), doi:10.1080/14786449808621172.

[80] W. A. Zisman, *A new method of measuring contact potential differences in metals*, Review of Scientific Instruments **3**, 7, pp. 367–370 (1932), doi:10.1063/1.1748947.

[81] M. Nonnenmacher *et al.*, *Kelvin probe force microscopy*, Applied Physics Letters **58**, 25, pp. 2921–2923 (1991), doi:10.1063/1.105227.

[82] J. M. Houston, *Theoretical efficiency of the thermionic energy converter*, Journal of Applied Physics **30**, 4, pp. 481–487 (1959), doi:10.1063/1.1702392.

[83] J. H. Ingold, *Calculation of the maximum efficiency of the thermionic converter*, Journal of Applied Physics **32**, 5, pp. 769–772 (1961), doi:10.1063/1.1736103.

[84] G. Kaye and T. Laby, *Tables of Physical and Chemical Constants*, 16th ed. (Longman, Essex and New York, 1995), ISBN: 0582226295.

[85] F. A. M. Koeck *et al.*, *Thermionic electron emission from low work-function phosphorus doped diamond films*, Diamond and Related Materials **18**, 5-8, pp. 789–791 (2009), doi:10.1016/j.diamond.2009.01.024.

[86] V. S. Fomenko, *Handbook of Thermionic Properties*, edited by G. V. Samsonov (Plenum Press, New York, 1966), ISBN: 0306651173.

[87] A. Y. Ender *et al.*, *Terrestrial solar power system based on Cs-Ba thermionic converter*, AIP Conference Proceedings **458**, pp. 1408–1412 (1999), doi:10.1063/1.57536.

[88] W. B. Stine and R. B. Diver, *A Compendium of Solar Dish/Stirling Technology*, tech. rep. (Sandia National Laboratories, Albuquerque and Livermore, 1994).

[89] R. Pitz-Paal, *Introduction to Solarthermal Power Plants - Lecture Script*, DLR Institut für Solarforschung, Köln, 2010.

[90] P. Gleckman *et al.*, *Concentration of sunlight to solar-surface levels using non-imaging optics*, Nature **339**, 6221, pp. 198–200 (1989), doi:10.1038/339198a0.

[91] American Society For Testing, *ASTM G173-03 Terrestrial (AM1.5) Reference Spectra*, available from `http://rredc.nrel.gov/solar/spectra/am1.5/`, 2003.

[92] Integrated Engineering Software, *IES.* COULOMB, AMPERES, and LORENTZ, version 9.0, `www.integratedsoft.com`, 2011.

[93] A. Roth, *Vacuum Technology*, 3rd ed. (Elsevier Science Publishers, Amsterdam, 1990), ISBN: 0444860274.

[94] magnetshop.com, *Materials*, `www.magnetshop.com/materials.html`, visited Mai 15, 2012, 2008.

[95] magnetladen.de, *Neodymmagnete*, `www.magnetladen.de/service/neodym-magnete/`, visited Mai 15, 2012, 2012.

[96] A. Hoffmann, Plansee Metall GmbH, 6600 Reutte, Austria, private communication on Jan. 29, 2010.

[97] Plansee Metall GmbH, *Tungsten*, `www.plansee.com/en/Materials-Tungsten-403.htm`, visited Jul. 13, 2012, 2012.

[98] HeatWave Labs Inc., 195 Aviation Way, Suite 100, Watsonville, CA 95076-2069, USA.

[99] J. L. Cronin, *Modern dispenser cathodes*, IEE Proceedings I, Solid-State and Electron Devices **128**, 1, pp. 19 –32 (1981), `doi:10.1049/ip-i-1.1981.0012`.

[100] R. Cortenraad *et al.*, *Surface analysis of thermionic dispenser cathodes*, Applied Surface Science **191**, 1–4, pp. 153–165 (2002), `doi:10.1016/S0169-4332(02)00175-7`.

[101] V. Vlahos *et al.*, *Ab initio investigation of barium-scandium-oxygen coatings on tungsten for electron emitting cathodes*, Physical Review B **81**, 5, pp. 054207 1–15 (2010), `doi:10.1103/PhysRevB.81.054207`.

[102] H. Ahmed and A. H. W. Beck, *Thermionic Emission from Dispenser Cathodes*, Journal of Applied Physics **34**, 4, pp. 997–998 (1963), `doi:10.1063/1.1729584`.

[103] R. W. Springer and T. W. Haas, *Auger electron spectroscopy study of cathode surfaces during activation and poisoning. I. The barium-on-oxygen-on-tungsten dispenser cathode*, Journal of Applied Physics **45**, 12, pp. 5260–5263 (1974), `doi:10.1063/1.1663226`.

[104] J. Cronin, *Practical aspects of modern dispenser cathodes*, Microwave Journal **22**, 9, pp. 57 (1979).

[105] J. Vaughn *et al.*, *The deactivation of impregnated type cathodes due to metal vapors*, Vacuum **11**, 2, pp. 77–79 (1961), doi:10.1016/0042-207X(61)90011-2.

[106] D. R. Lide, ed., *CRC Handbook of Chemistry and Physics*, 77th ed. (CRC Press, Boca Raton, 1996), ISBN: 0849304776.

[107] Lasercut24, Thomas Frey, Weimarische Str. 55, 99510 Apolda, Germany.

[108] R. Romminger, Edelstahltechnik und Laserbearbeitung, Gottlob-Bauknecht-Straße 26, 75365 Calw, Germany.

[109] T. C. Hales, *The honeycomb conjecture*, Discrete and Computational Geometry **25**, pp. 1–22 (2001), doi:10.1007/s004540010071.

[110] MatWeb LLC, *MatWeb Material Property Data*, Alumina 98 %, www.matweb.com, visited on Nov. 5, 2012.

[111] R. G. Wilson, *Vacuum thermionic work functions of polycrystalline Be, Ti, Cr, Fe, Ni, Cu, Pt, and type 304 stainless steel*, Journal of Applied Physics **37**, 6, pp. 2261–2267 (1966), doi:10.1063/1.1708797.

[112] R. J. D'arcy and N. A. Surplice, *Electric charges on stainless steel surfaces: The effects of hydrogen, charged particles, illumination, and electric fields on the work function*, Surface Science **34**, 2, pp. 193–211 (1973), doi:10.1016/0039-6028(73)90115-5.

[113] R. H. Bullis *et al.*, *The Plasma Physics of Thermionic Converters*, Journal of Applied Physics **38**, 9, pp. 3425–3438 (1967), doi:10.1063/1.1710144.

[114] P. V. Akimov *et al.*, *The true nature of space-charge-limited currents in electron vacuum diodes: A Lagrangian revision with corrections*, Physics of Plasmas **8**, 8, pp. 3788–3798 (2001), doi:10.1063/1.1383287.

[115] P. V. Akimov and H. Schamel, *Space-charge-limited current in electron diodes under the influence of collisions*, Journal of Applied Physics **92**, 3, pp. 1690–1698 (2002), doi:10.1063/1.1490616.

[116] S. Meir, C. Stephanos, T. H. Geballe, and J. Mannhart, *Highly-Efficient Thermoelectronic Conversion of Solar Energy and Heat into Electric Power*, submitted to the Journal of Renewable and Sustainable Energy (2013).

[117] F. Cziesla *et al.*, *Lünen – state-of-the-art ultra supercritical steam power plant under construction*, in POWER-GEN Europe, Cologne (2009).

[118] G. J. Snyder and E. S. Toberer, *Complex thermoelectric materials*, Nature Materials **7**, 2, pp. 105–114 (2008), doi:10.1038/nmat2090.

[119] A. F. Ioffe, *Semiconductor Thermoelements and Thermoelectric Cooling* (Infosearch Ltd. London, London, 1957).

[120] F. A. M. Koeck and R. J. Nemanich, *Low temperature onset for thermionic emitters based on nitrogen incorporated UNCD films*, Diamond and Related Materials **18**, 2-3, WOS:000264429300031, pp. 232–234 (2009), doi:10.1016/j.diamond.2008.11.023.

[121] Y. Toda *et al.*, *Field emission of electron anions clathrated in subnanometer-sized cages in* $[Ca_{24}Al_{28}O_{64}]^{4+}(4e^-)$, Advanced Materials **16**, 8, pp. 685–689 (2004), doi:10.1002/adma.200306484.

[122] Y. Toda *et al.*, *Intense thermal field electron emission from room-temperature stable electride*, Applied Physics Letters **87**, 25, pp. 254103 1–3 (2005), doi:10.1063/1.2149989.

[123] Y. Toda *et al.*, *Work function of a room-temperature, stable electride* $[Ca_{24}Al_{28}O_{64}]^{4+}(e^-)_4$, Advanced Materials **19**, 21, pp. 3564–3569 (2007), doi:10.1002/adma.200700663.

[124] R. T. Longo, *Physics of thermionic dispenser cathode aging*, Journal of Applied Physics **94**, 10, pp. 6966–6975 (2003), doi:10.1063/1.1621728.

A Acknowledgments

Diese Arbeit wäre in dieser Form ohne die tatkräftige Unterstützung zahlreicher Personen und Institutionen nicht möglich gewesen. Ich bin zu tiefstem Dank verpflichtet:

Meinem Doktorvater Herrn Prof. Dr. Jochen Mannhart für die Risikobereitschaft, ein solches Pionierprojekt zu starten und für das mir entgegen gebrachte Vertrauen. Für ein stets offenes Ohr und für zahlreiche spannende Diskussionen. Für seine pragmatische und visionäre Art und für die Freude an der Physik, die er bei jedem Gespräch zu vermitteln vermag.

Cyril Stephanos für den gemeinsamen Ausflug in dieses für uns alle so vollkommen neue Terrain und die äußerst fruchtbare und freundschaftliche Zusammenarbeit mit ihm. Für endlose Diskussionen zu allen Aspekten der Thermionik und weit darüber hinaus sowie dafür, dass er sich nie mit einer schlechten Begründung zufrieden gab.

Herrn Prof. Dr. Armin Reller für die Übernahme der Zweitkorrektur sowie für zahlreiche Ideen während der Projektphase.

Prof. emer. Theodore H. Geballe from Stanford who has pointed us on this fascinating topic and who has provided invaluable input during the work of this thesis.

Dr. habil. Andreas Schmehl für entscheidende Ideen in der Frühphase des Projektes und für zahlreiche hilfreiche Diskussionen.

Klaus Wiedenmann und Alexander Herrnberger für ihre Unterstützung beim Aufbau der Vakuumanlage und meiner Experimente sowie für einige der in dieser Arbeit gezeigten Fotografien.

Allen Mitarbeitern des Lehrstuhls für Experimentalphysik 6 für unzählige helfende Hände und offene Ohren, stete Diskussionsbereitschaft bei wissenschaftlichen und nichtwis-

senschaftlichen Fragen sowie ein entspanntes und doch so produktives Arbeitsklima. Insbesondere Prof. Dr. Thilo Kopp, Dr. German Hammerl, Dr. Florian Loder, Eleonore Saladie, Birgitta Eisenschmid und meinen zwischenzeitlichen Büromitbewohnern Dr. Martin Breitschaft, Dr. Veronika Tinkl, René Berktold und Rainer Jany.

Der Universität Augsburg und dem Freistaat Bayern für die herausragenden Arbeitsbedingungen, die ich am Zentrum für elektronische Korrelationen und Magnetismus genießen durfte und darf.

Der feinmechanischen Werkstatt für die sorgfältige Anfertigung der zahlreichen Bauteile meiner Experimente.

Georg Hilscher, Dr. German Hammerl und Dr. Veronika Tinkl für ihre Unterstützung bei der Suche nach orthografischen, typografischen und syntaktischen Ungereimtheiten.

Joël Amblard, Pascal Brachet, John Chambers, Matthias Ettrich, Robert Gentleman, Ross Ihaka, Donald Knuth, Leslie Lamport, Jendrik Seipp, Marc Shuttleworth, Richard Stallman, Linus Torvalds, the Center for History and New Media at the George Mason University, the Inkscape team, the Mozilla Foundation, the Scribus team, and the Wikimedia Foundation for initiating, developing, and maintaining open source software that has made my work live so much more enjoyable.

B Curriculum vitae

Name	Stefan Meir
Geburtstag	15. April 1984
Geburtsort	Augsburg

Schulbildung

1990-1994	Grundschule Emersacker
1994-2003	Gymnasium Wertingen
2003	Abitur

Zivildienst

Jul. 2003 - Jul. 2004	Sozialstation Dinkelscherben-Zusmarshausen-Welden

Studium

Okt. 2004 - Okt. 2009	Studium der Physik an der Universität Augsburg
Aug. 2008 - Aug. 2009	Diplomarbeit betreut von Prof. Dr. J. Mannhart "Untersuchungen elektronischer Zustände an Grenzflächen zwischen Metallen und organischen Materialien zur nichtflüchtigen Datenspeicherung"
Okt. 2009	Abschluss: Diplom-Physiker (Univ.)

Promotion

seit Nov. 2009	Wissenschaftlicher Angestellter an der Universität Augsburg